POLITECNICO DI TORINO

SCUOLA DI DOTTORATO

Dottorato in Dispositivi Elettronici – XXVI ciclo

Tesi di Dottorato

Nd^{3+} doped phosphate glass optical fibre lasers

Nadia Giovanna Boetti

Tutore Prof. Daniel Milanese

Coordinatore del corso di dottorato Prof. Giovanni Ghione

Febbraio 2014

To Alice and Nicolò

Acknowledgements

I would like to acknowledge a number of people for the assistance they have given me through my PhD.

First of all, I would like to express my deepest gratitude to my supervisor Prof. Daniel Milanese, for his support and responsiveness during those past years. He introduced me in the world of academic research and provided me an excellent working atmosphere during those years.

Part of this work involved productive collaborations with other members of our group. In particular, I give special thanks to Dr. Joris Lousteau for fibre drawing activity. Furthermore I would like to acknowledge him for all the ideas, suggestions and help he provided me during this research period. My thanks also go to Emanuele Mura and Davide Negro for glass fabrication activity and to Gerardo Scarpignato for laser simulation.

I would like to thank Istituto Superiore Mario Boella in the person of Ing. Silvio Abrate for having hosted me during these three years and all the PhotonLab researchers with whom I shared the office and the laboratory.

I would like also to thank Prof. Guido Perrone and Dr. Massimo Olivero for all the fruitful collaboration occasions we had and for their willingness in sharing equipment in the laboratory.

Contents

LIST OF ACRONYMS

AC alternated current

BO bridging oxygen

CW continuous wave

DC direct current

DC double cladding

DSC differential scanning calorimetry

DTA differential thermal analysis

EM electromagnetic

ESA excited state absorption

FWHM full width half maximum

GUI graphical user interface

IR infrared

LASER light amplification by stimulated emission process of radiation

LDVT linear variable displacement transducer

LED light emitting diode

LIDAR light detection and ranging

MCVD modified chemical vapour deposition

MM multimode

NA numerical aperture

NIR near infrared

NBO non-bridging oxygen

OC output coupler

OSA optical spectrum analyser

OVD Outside vapour deposition

PI power –current

PCF photonic crystal fibre

PCVD Plasma chemical vapour deposition

PECVD plasma-enhanced chemical vapour deposition

RE rare-earth

RF radio frequency

SBS stimulated Brillouin scattering

SESAM saturable absorber mirrors

SM single mode

SPL solar pumped laser

XRD X-ray diffraction

TIR total internal reflection

UV ultraviolet

VAD Vapour phase axial deposition

VIS visible

Introduction

In the last decade, a new laser technology appeared and revolutionized the world of laser applications: the fibre laser. This is a laser in which the active medium is realized using a specialty fibre doped with rare earth (RE) ions such as Nd^{3+}, Yb^{3+}, Er^{3+}, Tm^{3+}… The cavity for this kind of laser could be formed using all-fibre components, such as fibre Bragg gratings (FBG), instead of discrete dichroic mirrors, with an evident simplification of the mechanical set-up and an improved overall stability and reliability.

Nowadays fibre lasers are not only one of the fastest growing photonic technologies, but are also a sound industrial reality since they are rapidly eroding the market shares of the other laser technologies, thanks to their outstanding properties, such as high brightness, excellent mode quality, high efficiency and enhanced heat dissipation [1,2].

Moreover, fibre laser technology is extremely versatile and could be customized to suit the different applications in terms of output power, operating wavelength, mode of operation (continuous wave CW or pulsed regime), beam quality and dimension, spectral properties and output stability. Therefore fibre lasers find applications in a variety of fields such as industrial material processing, marking, semiconductor device manufacturing, surgery, military technology, remote sensing and scientific instrumentation.

In order to give a clearer picture on the dimension of fibre lasers market and how it is expected to continue to grow, we can consider three main laser market categories: laser marking, micro materials processing and macro material processing.

Laser marking (including engraving) is a market category that it is expected to continue to grow in near future, thanks to the increasing regulatory requirements on traceability set forth by governments and companies. This market sector is dominated by fibre lasers (see Fig. I.1), which grew 13% last year and are expected to continue to grow in 2014, while CO_2 lasers and solid state lasers continue to experience market share erosion.

REVENUE (US$M)	2012	2013	2014 (F)
CO_2	$47.5	$46.1	$44.7
y-to-y		-3%	-3%
SOLID STATE	$72.3	$69.0	$66.3
y-to-y		-5%	-4%
FIBER	$201.0	$227.1	$256.7
y-to-y		13%	13%
TOTAL	$320.8	$342.2	$367.6
y-to-y		6.7%	7.4%

Figure I.1. Lasers used for marking/engraving applications [3].

Micro materials processing include semiconductors and printed circuit board processing, fine metal processing (such as stent cutting and fuel injector nozzle drilling), additive manufacturing and processing of glass and ceramics and other non-metal materials. This sector (see Fig. I.2) is still dominated by solid-state lasers, but their decline is evident, while fibre lasers are challenging for leadership.

REVENUE (US$M)	2012	2013	2014 (F)
SOLID STATE	$184.6	$183.9	$185.8
y-to-y		0%	1%
FIBER	$111.7	$127.2	$154.3
y-to-y		14%	21%
CO_2	$126.7	$119.4	$117.3
y-to-y		-6%	-2%
OTHER	$141.6	$146.3	$137.1
y-to-y		3%	-6%
	$564.6	$576.8	$594.5
y-to-y		2.2%	3.0%

Figure I.2. All lasers < 1kW used for Micro Materials Processing [3].

By far, the largest revenue producing category is Macro Material Processing (see Fig. I.3), where high power lasers are used to process metals in thickness range greater

REVENUE (US$M)	2012	2013	2014 (F)
CO_2	$750.9	$696.1	$647.3
y-to-y		-7%	-7%
FIBER	$348.7	$432.4	$536.2
y-to-y		24%	24%
SOLID STATE	$210.0	$199.5	$190.5
y-to-y		-5%	-5%
DIRECT DIODE/OTHER	$116.2	$146.5	$167.0
y-to-y		26%	14%
TOTAL	$1,425.8	$1,474.4	$1,541.0
y-to-y		3.4%	4.5%

Figure I.3. All lasers ≥1kW used for Macro Materials Processing [3].

than 10 mm. In this market sector, although CO_2 lasers are still the first revenues source, fibre lasers showed an impressive growth of 24% that is expected to repeat in 2014.

The previous analysis outlines how fibre lasers are nowadays an excellent market opportunity but, at the same time, an extraordinary field of technological research, starting from materials science for the active material design, through the engineering of optical fibre, to the realization of the laser architecture.

That sets the background to this PhD research activity whose objective was the development of neodymium (Nd) doped phosphate glass optical fibre lasers.

Among the possible RE doping, the Nd^{3+} ion was chosen because is one of the most important activators for crystalline and bulk glass lasers, thanks to the power and efficiency available from the transition around 1.06 μm ($^4F_{3/2} \rightarrow {}^4I_{9/2}$). A Nd^{3+}-doped laser operated at this wavelength and pumped at wavelength of about 800 nm, behaves like a four-level laser system, so a positive internal gain is possible even for very small pump power and, therefore, a very low threshold can be achieved. Neodymium has been extensively used for the developing of glass-based lasers since the very beginning: the first glass laser [4], the first single-mode fibre laser [5], and the first cladding-pumped fibre laser [6] were all Nd^{3+}-doped.

Nd-doped lasers based on crystals (YAG, YVO4 or YLF) or on glass find applications in a variety of fields: starting from the low power of laser marking to high power of material processing [7]. Moreover these lasers are widely employed in medical [8,9] and aesthetic fields [10], normally in pulsed regime. Some applications, for example in dermatology, require visible laser light obtained by frequency doubling of the Nd main emission [11].

Beyond the well-known Nd^{3+} ion transition around 1.06 μm, this ion possesses two other interesting emissions: one around 0.9 μm ($^4F_{3/2} \rightarrow {}^4I_{9/2}$) and the other around 1.3 μm ($^4F_{3/2} \rightarrow {}^4I_{13/2}$).

Recently there has been a strong interest on the Nd ion emission around 0.9 μm. The main applications are the pumping of Yb and Er doped fibre amplifiers and the generation of blue light obtainable by frequency doubling [12]. This wavelength range has numerous potential applications such as biological and medical diagnostic, trace gas detection and Raman spectroscopy. UV light generation, which can be obtained by

frequency quadrupling, is also of great interest for many applications such as ozone remote sensing or writing of FBG [13]. Unfortunately obtaining high power laser emission from the transition ${}^4F_{3/2} \rightarrow {}^4I_{9/2}$ is quite challenging due to the three-level nature of this laser transition and the strong competition with main Nd emission. Nd^{3+}-doped lasers based on this transition have been demonstrated in crystals like Nd:YAG [13] and Nd:YVO_4 [14] and recently in double cladding (DC) fibre [12,15] with record emission of 20 W at 910 nm.

Concerning the Nd^{3+} ion emission around 1.3 μm, it is potentially very important for optical communication system in the second window, and was largely investigated in 80's and 90's [16,17]. The work was essentially discontinued after the demonstration of a more efficient source at 1.3 um obtained by Pr-doped fluoride fibres [18,19]. Current interest on this emission is mainly driven from application for optical coherence tomography [20], medical [21] and aesthetic application for skin rejuvenation [22].

Optical fibres for laser applications are made of glasses and different glasses suitable for photonic applications are known in the literature, with a variety of chemical, physical and optical properties. Nonetheless, most of the research activity on fibre lasers carried out so far have been performed on doped silica glasses, thanks to its outstanding properties, in particular the extremely low propagation losses, the possibility to withstand high temperature and the impressive mechanical strength against pulling and even bending. However silica glass presents also some drawbacks: for example RE ions have a very low solubility in this glass system and are prone to clustering.

Phosphate glasses have demonstrated in last years to be an alternative host material to silica glass, especially for high power applications. In fact, they enable extremely high doping level of RE ions (up to 10^{21} ions/cm^3) and thus more compact active devices [23]. In fact the length of the phosphate fibre laser can be substantially decreased even below ten centimetres in order to have an output power in the order of watt level, in a single frequency operation. Moreover, phosphate glasses offer a higher photo-darkening threshold than silica and low nonlinear refractive index, that make them suitable for the realization of high power, high brilliance single-frequency laser sources [24,25]. Another important feature of phosphate glasses is their thermal and

mechanical strength, that allows the realization of optical fibres that can be cleaved and fusion spliced with commercial optical fibre components based on silicate glasses [26], thus allowing an easier integration of these fibres in commercial system.

The research activity carried out during this PhD aimed at designing, engineering and manufacturing in-house a novel Nd^{3+}-doped phosphate glass material suitable for the development of optical fibre lasers to be customized for different applications.

The first step of the work was to obtain a passive phosphate glass stable, robust, able to incorporate high amount of RE ions and suitable for fibre drawing. Afterwards several Nd-doped phosphate glass samples were fabricated by doping the developed host glass with different Nd^{3+} ion concentrations. The samples were then thoroughly characterized in order to measure their physical, thermal and spectroscopic properties.

After this work on active material, a Nd^{3+}-doped double cladding optical fibre was designed, engineered and drawn using a drawing tower facility hosted in the research group laboratory located at Istituto Superiore Mario Boella. The manufactured fibre was then used to demonstrate laser action around 1.06 μm in the developed Nd^{3+}-doped phosphate glass.

Part of the PhD research activity was also dedicated to solar pumped laser (SPL), a very interesting device able to convert the broad-band and incoherent solar radiation into coherent and narrow-band laser radiation. The Nd^{3+}-doped phosphate glass developed in this PhD research activity has the potential to be used as active material for the development of a SPL, in particular in fibre form, with several key advantages over conventional bulk rods or disk. A preliminary study of the possibility to realize a solar pumped laser based on the developed Nd^{3+}-doped phosphate glass was carried out, with evaluation of a co-doping with another RE, europium (Eu) with the aim of increasing the overall pump power conversion efficiency.

This dissertation is organized as follows. Chapter 1 briefly reviews glass definition and main structural and thermodynamics properties. Phosphate glass is introduced along with its peculiar features that made it the material of choice for the development of the Nd^{3+}-doped double cladding optical fibre realized for this PhD research activity.

Chapter 2 is dedicated to optical fibres: description of their basic structure, transmission of light along the fibre and main mechanisms behind the attenuation of light travelling in the fibre. Main fibre fabrication methods are introduced, with a

particular attention to the preform drawing method used to fabricate the Nd^{3+}-doped double cladding optical fibre manufactured for this PhD activity. A description of the optical tower facility hosted in our research laboratory is also added.

In chapter 3 basic principles of laser action are reviewed, along with unique properties of laser light. The fundamental of rare earth solid state lasers are presented, with a focus on Nd^{3+}-doped phosphate glass lasers. The second part of the chapter is focused on fibre lasers: their key advantages over the other solid state lasers, common laser resonators setup and the possibility of power scaling through double cladding optical fibre design. At last, state of the art in the research on Nd^{3+}-doped phosphate fibre lasers is briefly reviewed.

Chapter 4 presents the novel Nd^{3+}-doped phosphate glass host material developed in-house for this research and describes the method of glass fabrication. Main glass characterization techniques are briefly reviewed and measurements results obtained from the fabricated glasses are presented and discussed. Particular attention is devoted to the fluorescence spectroscopy measurement, for which a dedicated setup on optical bench was realized as part of the work of this thesis.

In chapter 5 the realization of a Nd^{3+}-doped double cladding optical fibre is described step by step, from the manufacture of the three required phosphate glasses, to preform fabrication and fibre drawing. Demonstration of a continuous wave cladding pumped fibre laser based on 9 cm of the manufactured optical fibre is reported along with main laser characterization results. Preliminary conclusions of the work are also drawn.

Chapter 6 is dedicated to solar pumped laser: a brief introduction about solar radiation, basic concept of SPL, potential applications on the earth and in space and state of the art in this research field. A new technological approach to SPL based on fibre laser technology is proposed along with its key advantages over conventional solid state lasers. Preliminary experimental results of the assessment of the developed Nd^{3+}-doped phosphate glass as SPL active material are also reported.

REFERENCES

[1] J. Nilsson and D. Payne, "High-power fiber lasers," Science 332, n. 6032, pp. 921-922, 2011.

[2] C. Jauregui, et al., "High-power fibre lasers," Nat Photonics 7, pp. 861–867, 2013.

[3] http://www.industrial-lasers.com/

[4] E. Snitzer, "Optical maser action of Nd in a barium crown glass," Phys. Rev. Lett., vol. 7, no. 12, pp. 444–446, 1961.

[5] R. J. Mears, et al., "Neodymium doped silica single-mode fiber lasers," Electron. Lett., vol. 21, no. 17, pp. 738–740, 1985.

[6] E. Snitzer, et al., "Double-clad, offset-core Nd fiber laser," Proc. Conf. Optical Fiber Sensors, Postdeadline paper PD5, 1988.

[7] W.M Steen et al., "Laser Material Processing," 4th edition, Ed. Springer 2010.

[8] P. F. Bradley, "A review of the use of the neodymium YAG laser in oral and maxillofacial surgery," Brit J Oral Max Surg 35, pp. 26-35, 1997.

[9] T. Qadri et al., "Significance of scaling and root planning with and without adjunctive use of a water-cooled pulsed Nd:YAG laser for the treatment of periodontal inflammation," Lasers Med Sci 1-4, 2013.

[10] M. W. C Lee "Long-Pulse Neodymium-Doped Yttrium Aluminum Garnet Laser for Hypopigmentation and Other Diverse Applications," Dermatol Surg 36, pp. 1681–1682, 2010.

[11] G. L. Becher et al., "Treatment of superficial vascular lesions with the KTP 532-nm laser: experience with 647 patients," Lasers Med Sci 1-5, 2013.

[12] M. Laroche et al., "20 W continuous-wave cladding-pumped Nd-doped fiber laser at 910 nm," Opt Lett 38, pp.3065-3067, 2013.

[13] X. Délen et al., "34 W continuous wave Nd:YAG single crystal fiber laser emitting at 946 nm," Appl Phys B-Lasers O, vol. 104, Issue 1 , p.p 1-4, 2011.

[14] X. Yu et al., "High power diode-pumped 914-nm Nd:YVO4 laser," Chin. Opt. Lett. 8, pp. 499-501, 2010.

[15] J. W. Dawson et al., "Scalable 11W 938nm Nd^{3+} doped fiber laser," presented at the Proc. Advanced Solid-State Photonics, Santa Fe, NM, Feb. 2–5, 2004, Paper MD8.

[16] S. G. Grubb et al. "Diode-pumped 1.36 μm Nd-doped fibre laser," Electron. Lett. 26, pp. 121–122, 1990.

[17] S. Zemon et al., "Comparison of Nd^{3+}-doped glasses for amplification in the 1300-nm region," In: Fiber Laser Sources and Amplifiers IV. Proc. SPIE 1789, pp. 58–65, 1993.

[18] W. J. Miniscalco et al., "1.3 μm fluoride fibre laser," Electron. Lett. 24, pp. 28–29, 1988.

[19] Y. Miyajima et al. "Rare earth-doped fluoride fiber amplifiers and fiber lasers," Opt. Fiber Technol. 1, pp. 35–47, 1994.

[20] K. Bizheva, "Compact, broad-bandwidth fiber laser for sub-2-mm axial resolution optical coherence tomography in the 1300-nm wavelength region," Opt Lett 28, No. 9, pp. 707-709, 2003.

[21] T. M. Proebstle et al., "Endovenous Treatment of the Great Saphenous Vein Using a 1,320 nm Nd:YAG Laser Causes Fewer Side Effects than Using a 940 nm Diode Laser," Dermatol Surg 31, pp. 1678–1684, 2005.

[22] M. A. Trelles et al., "Facial rejuvenation with nonablative 1320 nm Nd:YAG laser, " Dermatol. Surg. 27, pp 111-116, 2011.

[23] Y.W. Lee, et al., "20 W single-mode Yb^{3+}-doped phosphate fiber laser," Opt. Lett., vol. 31, pp. 3255-3257, 2006.

[24] Y. W. Lee, et al., "High-Power Yb^{3+}-Doped Phosphate Fiber Amplifier," J. Sel. Top. Quant. 15, pp. 93-102, 2009.

[25] J. H. Campbell, in Inorganic Optical Materials, P. Klocek, Ed. SPIE CR 64 3-39, 1996.

[26] A. Polynkin, et al. "Watts-level, short all-fiber laser at 1.5 mm with a large core and diffraction-limited output via intracavity spatial-mode filtering," Opt. Lett., 30, pp. 403-405, 2005.

Chapter 1

Phosphate glasses

Among photonic materials, glass plays an important role thanks to its unique structural and thermodynamic features. Besides stability, glass presents an excellent homogeneity, good thermo-mechanical properties and a viscosity–temperature relationship that allows for fibre drawing. Moreover glass has a wide flexibility of the chemical composition and doping, allowing the preparation of multi-components glass with properties that can be customize to meet the needs of different applications.

The first part of the chapter briefly reviews glass definition and main structural and thermodynamics properties. In the second part of the chapter, phosphate glass will be introduced along with its peculiar features that made it the material of choice for the development of the Nd-doped double cladding optical fibre realized for this PhD research activity.

1.1 Introduction to glass material

1.1.1 Structural properties

A glass, whether in bulk, fibre or film form, is a non-crystalline (or amorphous) solid. In principle, any substance can be vitrified by quenching it from the liquid state, while preventing crystallization, into a solid glass [1].

The atomic arrangement of a glass is characterized by the absence of long-range order which defines crystalline materials and it is quite close to the atomic arrangement

in a liquid, with a variety of short to medium range order, which originates from chemical bonding and related interactions (see Fig. 1.1).

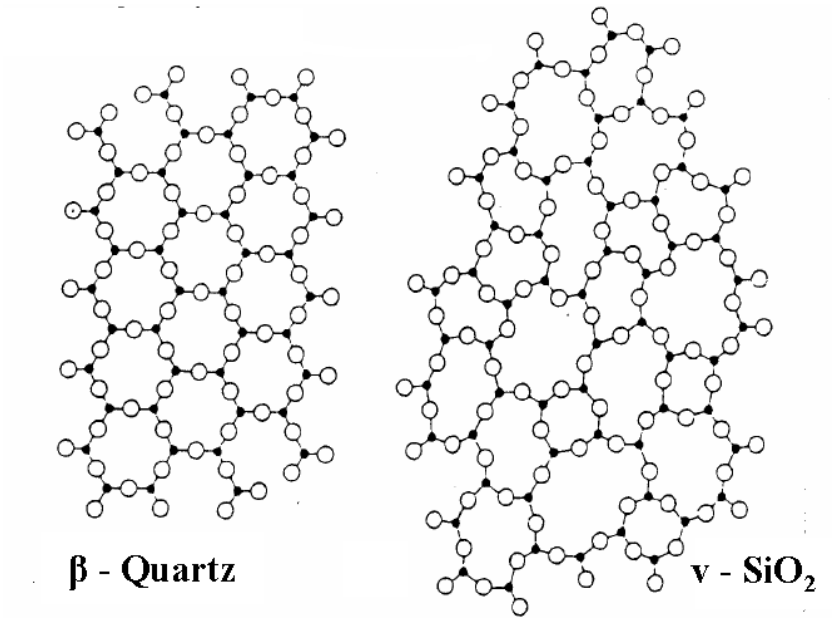

Figure 1.1. Two-dimensional atomic arrangement of SiO_2 in (a) crystalline lattice structure and (b) random network glass [1].

One of the best experimental characterization method to distinguish an amorphous solid, such as glass, from a crystalline material is X-ray diffraction (XRD). In case of glass, instead of diffraction peaks, a halo is seen in the XRD pattern.

Although in principle any material could form glass, in practice glass formation is limited, in the case of inorganic materials, to a relatively small number of substances found in oxide, halide, and chalcogenide systems.

The substances that form the three-dimensional random network of strong bonds in a glass are called the ***network formers***. Examples of these constituents are: silica (SiO_2), phosphorous oxide (P_2O_5), germania (GeO_2), boron oxide (B_2O_3) and tellurium oxide (TeO_2).

Other components, called ***network modifiers***, can also participate in glass formation, causing a breakdown of the glass network and thus modifying glass properties. They are weakly bonded to the network and can easily diffuse inside the material. Their incorporation aims at modifying physical and chemical properties (such as melting and working temperatures, refractive index, fluorescence, viscosity, tendency to

devitrification, chemical resistance) of the glass. Examples of modifiers are alkali oxides (Na_2O, K_2O, Li_2O), earth-alkali oxides (MgO, CaO, BaO) and zinc oxide (ZnO).

Oxygen ions, which act as bridges between the structural units, are called ***bridging oxygens*** (BO). The introduction of modifiers in the glass breaks some of these bonds and creates ***non-bridging oxygens*** (NBO). These oxygen ions carry a partial negative charge and are connected to the glass network at one end only (see Fig. 1.2).

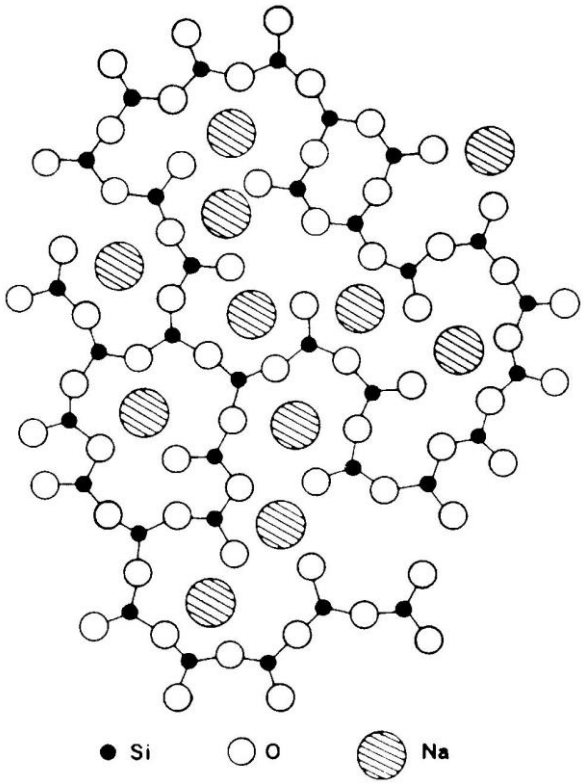

Figure 1.2. Two-dimensional atomic arrangement of a glass (sodium silicate glass) containing a glass modifier element (Na) [2].

Other substances, called ***glass intermediates***, do not form glass alone, but in a limited amount, they can take part to the glass former amorphous network. Examples of these compounds are alumina (Al_2O_3), titanium oxide (TiO_2) and zirconia (ZrO_2). They are strongly bonded to the network.

Thanks to its unique structure, glass has the great advantage of the flexibility of the chemical composition. In fact, unlike crystalline materials, there is no requirement of stoichiometry among constituents, provided that the electrical neutrality over the whole

structure of a glass is maintained. Thus, in principle, it is possible to form a glass by any composition that contains a sufficient amount of a network former, allowing the preparation of a variety of multi-components glass with the desired properties.

Moreover, the flexibility of the chemical composition makes also easier the doping with active materials, such as RE or transition metal ions. Considering the lack of regularity of glass structure, the local environment of RE ions is different from site to site, making the absorption and emission spectra from the ion broader than those from active ions doped in a crystalline material (Fig. 1.3), a feature which is advantageous in the preparation of active glass.

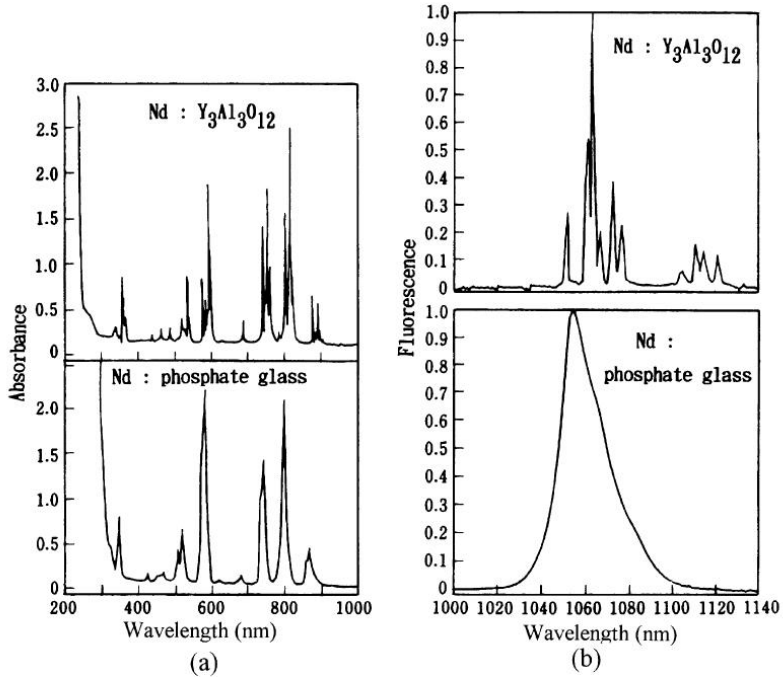

Figure 1.3. Absorption (a) and emission (b) spectra of Nd ions in YAG crystal and phosphate glass [3].

1.1.2 Thermodynamic properties

A glass could be also defined as an amorphous solid that exhibits a glass transition temperature T_g. Below T_g the glass is in a rigid and brittle state, while above T_g it is in a molten or rubber-like state.

Figure 1.4 illustrates what happens to the specific volume of glass as temperature changes. If the cooling is sufficiently rapid (relative to the characteristic crystallization

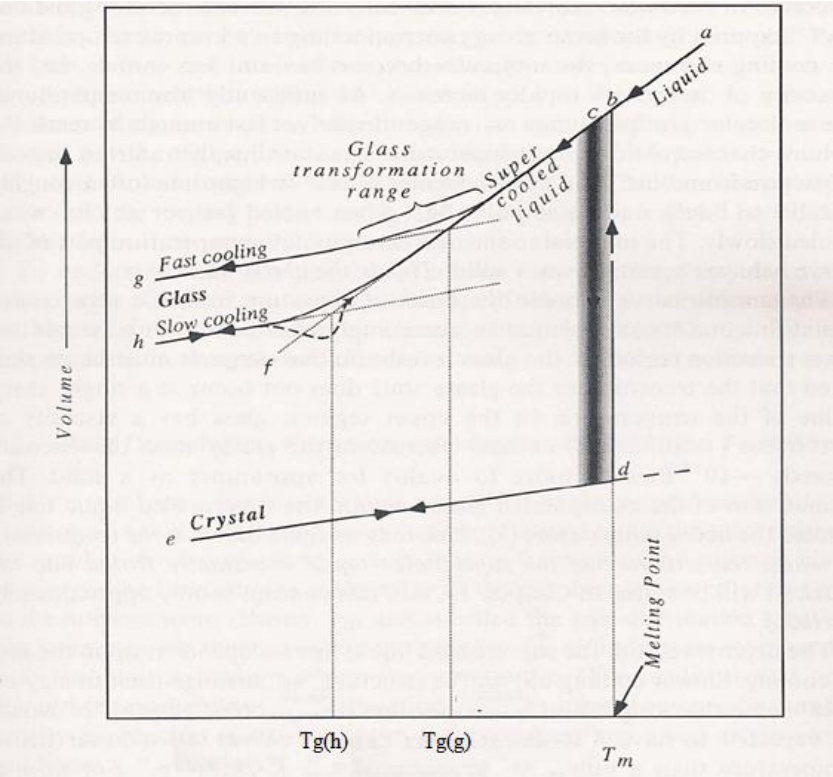

Figure 1.4. Temperature dependence of a glass forming liquid's volume. (adapted from [4]).

time) then crystallization is prevented and instead the disordered atomic configuration of the supercooled liquid is frozen into the solid state at T_g. Generally, the structure of a glass exists in a thermodynamically metastable state with respect to its stable crystalline form, due to hindrance of the atomic rearrangement during the process of glass formation.

Unlike the melting temperature T_m, which represents a first order thermodynamic transition, accompanied by a discontinuity in the specific volume, T_g is not a well-defined temperature, but rather a temperature range. Therefore, T_g is not always the same, even if the chemical composition is the same, but depends on the cooling rate of the supercooled liquid. The faster the quenching of the liquid, the higher the T_g value of the glass obtained. In fact, a slow cooling allows enough time for a viscous liquid to alter its local atomic arrangement to attain the minimum free energy at the corresponding temperature, whereas a rapid cooling causes an increase of viscosity that

is too quick for the local atomic arrangement to follow and results in a transition into a glass at a higher temperature.

The properties of a glass are therefore different from glass to glass, depending on the thermal history, even if the chemical composition is the same.

An important parameter directly involved in glass formation from the melt is the viscosity. Experimentally, it is possible to observe that a liquid with low viscosity at the melting point tends to crystallize, while a viscous liquid may easily form amorphous solids, i.e. a glass.

The viscosity η of a molten glass is a strong function of temperature, rapidly decreasing when the temperature increases (see Fig. 1.5). The variation of molten glass viscosity with temperature often follows the Arrhenius law:

$$\eta = \eta_0 exp^{\frac{E_\eta}{RT}} \tag{1.1}$$

where T is temperature, R is the molar gas constant, E_η is the activation energy for viscous flow (kJ/mol), independent of temperature, and η_0 is approximately a constant.

Arrhenius behaviour occurs especially in case of melts with strong glass-forming ability (SiO_2, P_2O_5,GeO_2, BeF_2, ...), sometimes referred as strong liquids. On the other

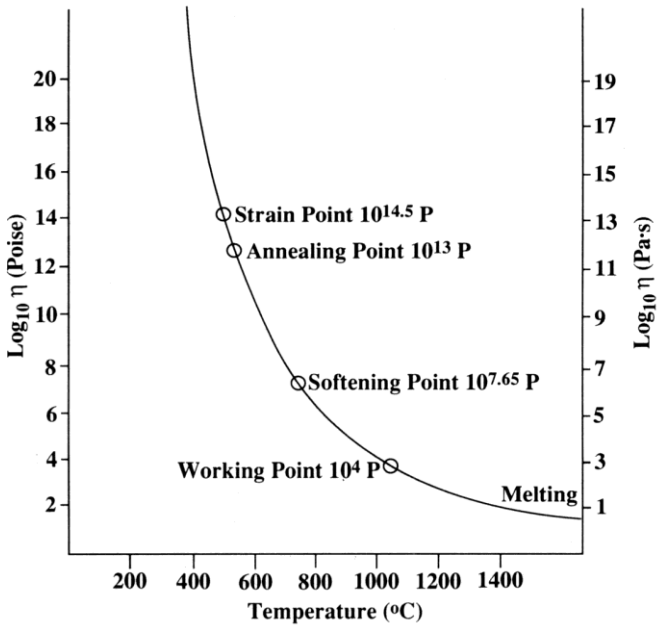

Figure 1.5. Temperature dependency of viscosity of a standard soda lime silica glass [4].

hand, melts with weak glass-forming ability, like most glass-forming halides (ZrF_4–based compositions, $ZnCl_2$, ...), usually exhibit an activation energy for viscous flow which strongly decreases with increasing temperature. Such melts are sometimes referred as fragile liquids.

When a viscous liquid is rapidly cooled, viscosity increases exponentially until a value to near or above 10^{14} Pa s, without being transformed into a crystal. Once the viscosity reaches this value, even the alteration of the local atomic arrangement to equilibrate with temperature is not possible, resulting in the frozen structure. Then the material behaves as a rigid and brittle solid, i.e. a glass.

Given the importance of viscosity in glass technology, five standard viscosity reference points (or temperature ranges) were defined:

- ***melting point*** (η= 10 Pa s): the glass is fluid enough to be considered a liquid;
- ***working point*** (η= 10^4 Pa s): the glass is suitable for working or forming;
- ***softening point*** (η= $10^{7.65}$ Pa s): it is the temperature at which glass deforms under its own weight;
- ***annealing point*** (η= 10^{13} Pa s): it corresponds to the maximum temperature, in the annealing range, at which the internal strain of glass will be substantially eliminated;
- ***strain point*** (η= $10^{14.5}$ Pa s): it corresponds to the lowest temperature in the annealing range at which viscous flow of glass will not occur. Stress release from the glass occurs in a matter of minutes at the annealing temperature and in a matter of hours at the strain point.

Most glass-forming operations are carried out within the working range, thus between the working and softening temperatures. Of course, the temperature at which each of these points occurs depends on glass composition.

The particular viscosity-temperature relationship of a glass is the main reason behind the possibility of glass optical fibre drawing.

1.2 Phosphate glass

The first phosphate glasses, with low dispersion and relatively high refractive indices (compared with silicate-based optical glasses) were developed for achromatic optical elements about 100 year ago by Schott and co-workers. Later on, in 1940s, interest in

alkaline earth phosphate glasses was stimulated by their high transparency for ultraviolet (UV) light, again when compared with silicate glasses. However, their applications were limited by the poor chemical and mechanical resistivity [5,6]. In the 1950s, alkali phosphates glasses were used in several industrial applications like sequestering agents for hard water treatments and dispersants for clay processing and pigment manufacturing [7].

But it was in the 1960s, with the advent of solid state lasers that started a new era of phosphate glass research, thanks to their particular features (such as large RE stimulated emission cross-sections and low thermooptical coefficient) that make them suitable for high power laser applications [8]. In particular the interest was focused on Nd-doped phosphate laser glasses [9].

More recently, phosphate glasses have been developed not only for optical applications but also for a variety of specialty applications such as hermetic seals, nuclear waste hosts and medical applications [10]. In particular, phosphate glasses are a material of interest for use as biomaterials because of their ability to dissolve completely in aqueous solutions into safe dissolutions products, commonly found in human body.

Table 1.1 reports a list of areas of interest and potential applications of phosphate glasses.

1.2.1 Phosphate glass structure

The properties that make phosphate glasses good candidates for so many different applications are related to their molecular-level structures of the glass network and the role of network modifiers and intermediates.

The glass forming component of phosphate glass is P_2O_5. The basic building blocks of the glass are P-tetrahedra that result from the formation of sp^3 hybrid orbitals by the P outer electrons ($3s^2 3p^3$). The fifth electron is promoted to a 3*d* orbital where strong p-bonding molecular orbitals are formed with oxygen 2*p* electrons [6]. The tetrahedra are bonded through covalent bridging oxygens to form different phosphate anions. The tetrahedra could be classified using the Q^i terminology [11], where *i* represents the number of bridging oxygens per tetrahedron (see Fig. 1.6).

Table 1.1. Properties and areas of application of phosphate glasses [10].

Properties	Outstanding features	Potential applications
Composition	Offer extremely wide range of compositions, possible to tailor the chain-like polymeric structure	Oriented metaphosphate glass fibers [2]
		Injection moldable glass-polymer melt blends [3,4]
Preparation temperature	Low[a] Sn–Pb–F–P–O glass: $T_g \approx 100$ °C [25] g-Pb–In–P–O glass: $T_m = 900$ °C, $T_p = 800$–900 °C, $T_g = 436$ °C, $T_s = 459$ °C [6]	Castable lenses and optical elements [5]
Chemical durability	Poor for ultraphosphate glasses, but can be strengthened drastically by incorporation of modifier oxides	Nuclear waste storage media [7,8]
Thermal expansion	High. alkali-alkaline earth P-glasses: $10–20 \times 10^{-6}$/°C [9]	Glass-to-metal seals
Electrical conductivity	Fast ionic conduction AgI–Ag_2O–P_2O_5 glasses: 10^{-3}–$10^{-2}\ \Omega^{-1}\ cm^{-1}$ [1,11] Proton conduction H^+-implanted $Mg(PO_3)_2$ glass: DC conductivity 5×10^{-4} s cm^{-1} [12]	Solid electrolytes Fuel cell materials
Optical clarity	High index of refraction, 1.75–1.91 for Pb–In–P–O, Pb–Sc–P–O [6], and Pb–In–Al–P–O glasses [13] Moderately low dispersion	Optical applications
UV transparency	High-energy excitations of the bridging and nonbridging oxygen orbitals leads to superior UV-transparency [14,16]	Wide-band optical fibers for communication
Stimulated emission	Narrow line widths, high transition strengths, high refractive index and spectral homogeneity [17,18] Photochromism and thermochromism [15,19]	High average-power lasers [26] Solar energy collectors Light- and heat-sensitive colored glasses
Surface chemistry	Hydrolyzed, nonmisting surface [20]	Lenses and windows for marine applications
Nucleation and crystallization	Controlled formation of microstructure in glass ceramics	Hydrogen-filled BPO_4 gas ceramic [21]
Biocompatibility and bioactivity	Capable of bonding to living bone by glass formation of a Ca–P-rich surface film [22–24]	Bioglass Bioceramics

[a]Glass transition temperature (T_g), melting temperature (T_m), pouring temperature (T_p), softening temperature (T_s).

The networks of phosphate glasses can be classified by the ratio between oxygen and phosphorus in:

- ***ultraphosphate*** for 2,5 < [O]/[P] < 3,0
- ***metaphosphate*** for [O]/[P] = 3,0
- ***polyphosphate*** for [O]/[P] > 3,0

A detailed description of the atomic structure of the different glasses is out of scope of this thesis and could be find in [6].

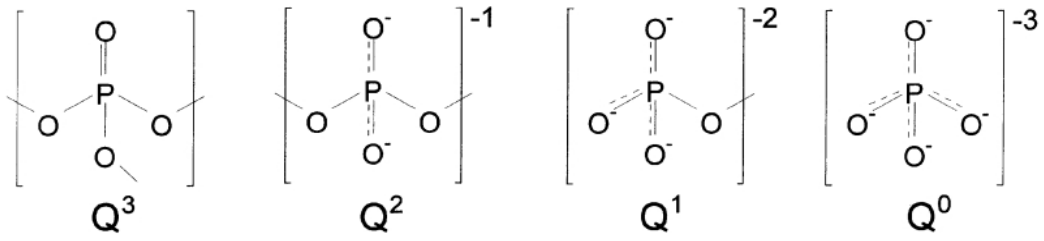

Figure 1.6. Different phosphate tetrahedral sites existing in phosphate glasses [6].

P_2O_5 is a network former and could be used to form a glass alone under certain conditions. But this glass is extremely reactive and hygroscopic and is not used in practical applications. However, the durability and stability can be increased by adding network modifiers, such as H, alkali, alkali-earth or transition metals that break the P-O-P links and create additional NBO. The resulting glass structure is disrupted, containing not only covalent P-O-P bond, but also ionic links between NBO. This process is called depolymerisation of the network. [12]

The presence of water in phosphate glasses act as network modifiers, by disrupting P-O-P linkage and creating P-OH group instead. This reaction occurs readily for ultraphosphate glasses and limits the technological usefulness of these glasses even though they possess UV edges at wavelengths shorter than found for silicate glasses [13].

Water content of the glass is critical especially in case of doping with RE ions. When OH^- groups are present in a glass, the nonradiative rates are increased because of coupling between the RE states and the high energy (3200 cm^{-1}) vibrations of OH^-. Since this effect reduces the lifetimes of the RE states, the water content of the glass must be controlled to be as low as possible (see chapter 3).

1.2.2 Fabrication method

Phosphate glasses are commonly manufactured by mixing glass precursor and melting at high temperatures in a platinum or alumina crucible. The melting temperatures tend to be lower than those of silicate glasses, and are usually between 800 and 1400 °C, depending on the glass composition.

The reactivity of phosphate glasses to water influence also their preparation method: instead of conventional open crucible techniques [14,15] they are often manufactured using anhydrous raw materials melted in sealed ampoules [16]. The preparation method has influence on the resulting density and refractive index of the glass.

After melting, the glass is cast into a graphite or metal mould preheated at a temperature close to the glass transition temperature T_g. Then the glass is annealed, that is, allowed to cool down to room temperature slowly in order to relieve glass internal stress.

An alternative route for making glasses is sol-gel method. Although this process for phosphate is quite new and the obtained glasses seem to be more fragile than the ones made by traditional method.

1.2.3 Phosphate glass for photonic applications

Silica based glasses are the most widespread material used for photonic systems, especially for data transmission. However, other applications depend on optical amplification (through dopants or nonlinear optical processes), infrared (IR) light transmission or high optical nonlinearities that require alternative glass systems with suitable properties. Although these glass systems are not applied to mass production due to the higher cost of raw material (compared to silicate), lower chemical durability and mechanical strength, they possess unique properties that cannot be obtained for silicate glasses.

One of these alternative glass systems is phosphate glass that possesses several interesting features as materials for optical applications and in particular for compact high-power laser system, also in fibre form:

- Large glass formation region.
- Possibility of glass manufacturing free of platinum inclusions thereby greatly increasing the optical damage threshold. Residual micron-size platinum inclusions in the glass could be eliminated by chemical treatment of the glass. It has not yet been possible to achieve comparable results for silicates or fluorides [17].
- Good thermal and mechanical strength (compared to fluoride or tellurite). For high power application high fracture toughness, high thermal conductivity and low

thermal expansion of the glass are critical. Moreover, for glass in fibre form, it is important the possibility to cleave and fusion spliced the phosphate fibre with commercial fibre and optical fibre components based on silicate glasses [18].

- Low thermo-optical coefficient. In comparison with crystals, the major disadvantage of glass is its low thermal conductivity. A laser glass is thermally loaded by pump radiation and by the laser beam itself. Since glass has a low thermal conductivity compared to crystal, optical distortion occurs due to a change of refractive index with temperature, and this effect limits its applicability in high average-power systems. For this application glass, like phosphates, with low thermo-optical coefficient are preferred.
- Low nonlinear refractive index. Especially in case of high intensity light, this property limits the detrimental effect of non-linear processes.
- High solubility of RE ions and resistance to quenching concentration effect. Phosphate glasses enable extremely high doping level of RE ions (up to 10^{21} ions/cm^3) and thus the realization of more compact optical gain devices [19].
- High absorption cross-section for RE elements.
- Higher photo-darkening threshold than silica. It has been demonstrated the possibility to dope a phosphate fibre with at least six times higher Yb^{3+} concentration than highly Al-doped silica fibres without the onset of photodarkening [20].
- Ion exchangeability and thus the possibility to fabricate waveguide structure in glass.

In Table 1.2 typical values of selected properties of phosphate glass are reported in comparison with main glass systems. These values can vary with changing the glass compositions.

Table 2.2. A comparison of selected properties of main glass systems typical values of the properties are reported for each glass family: these may vary with changing the glass compositions [21].

Glass property	**Silica**	**Phosphate**	**Tellurite**	**Fluoride ZBLAN**	**Chalcogenide**
Transmission range [µm]	0.2 ÷ 2.5	0.2 ÷ 4	0.4 ÷ 5.0	0.2 ÷ 6	0.8÷ 20
Maximum phonon energy [cm^{-1}]	1100	1200	800	600	350
Glass transition temperature [ºC]	1000	461	300	260	300
Thermal conductivity [W/(mK)]	1.38	0.57	1.25	0.628	0.2
Expansion coefficient [10^{-6}/K]	0.55	13.4	12 ÷ 17	17.2	14
Density [g/cm^3]	2.2	2.59	5.5	4.33	4.51
Young's modulus [GPa]	70	47	33.6	58.3	21.5
Refractive index	1.458 @ 0.589 µm	1.507 @ 0.587 µm	2 @ 1.55 µm	1.499 @ 0.589 µm	2.9 @ 10.6 µm
Abbe number	68	68	10 ÷ 20	76	NA
Nonlinear index [m^2/W]	10^{-20}	10^{-20}	$2.5 * 10^{-19}$	10^{-21}	10^{-18}
Thermo-optic coefficient [10^{-6}/ K]	12 @ 1.06 µm	-4.7	-16.4	-14.75 @ 1.06 µm	10 @ 10.6 µm
Fiber loss [dB/Km]	0.2 @ 1.5 µm	$1.5*10^3$ @ 1.05 µm	50 @ 1.2 µm	0.65 @ 2.59 µm	12 @ 3 µm
RE solubility	10^{19} ions/cm^3	10^{21} ions/cm^3	10^{21} ions/cm^3	10^{21} ions/cm^3	0.1 mol%

REFERENCES

[1] http://www.lehigh.edu/imi/OPGCourse.htm

[2] M. Yamane and Y. Asahara, "Glasses for Photonics," Cambridge University Press, 2004.

[3] M. J. Weber, "Handbook of the Physics and Chemistry of Rare Earth," Vol. 4, ed. K. A. Gschneider, Jr. and L. Eyring, North-Holland Publishing Company, Amsterdam, 1979.

[4] A. K. Varshneya, " Fundamentals of inorganic glasses," Academic Press, 1994.

[5] N. J. Kreidl, W. A. Weyl, "Phosphates In Ceramic Ware: Iv, Phosphate Glasses," J. Am. Ceram. Soc. 24 11, pp. 372-378, 1941.

[6] R. K. Brow, "Review: the Structure of Simple Phosphate Glasses," J. Non-Cryst. Solids 263-264, pp. 1-28, 2000.

[7] J. R. Van Wazer, "Phosphorus and its Compounds," vol. 1, Interscience, New York, 1958.

[8] M. J. Weber, "Science and technology of laser glasses," J. Non-Cryst. Solids 123, pp. 208-222, 1990.

[9] J. H. Campbell, T. I. Suratwala, "Nd-doped phosphate glasses for high-energy/high-peak-power lasers," J. Non-Cryst. Solids 263&264, pp. 318-341, 2000.

[10] C. K. Loong et al., "Structure and Dynamics of Phosphate Glasses: from Ultra- to Ortho-Phosphate Composition, "Physica B 241-243, pp. 890, 1998.

[11] F. Liebau, in: M. O'Keefe, A. Novrotsky (Eds.), "Structure and Bonding in Crystals II," Academic Press, New York, 1981.

[12] J. Jones, A. Clare, "Bio-Glasses: An introduction," John Wiley & Sons Ltd, 2012.

[13] W. Vogel, in: D.R. Uhlmann, N.J. Kreidl (Eds.), "Optical Properties of Glass," American Ceramic Society, 1991.

[14] E. Kordes and H. Becker, “Physical-chemical studies on the fine structure of glasses. V. glasses of the binary systems of P_2O_5 with CdO, Na_2O and Li_2O,” Z. Anorg. Allgem. Chemie 260, pp. 185-207, 1949.

[15] P. E. Gray and L. C. Klein, "Chemical durability of sodium ultraphosphate glasses,” Glass Technol. 24, pp. 202-206, 1983.

[16] J. J. Hudgens, PhD thesis, Iowa State University, 1994.

[17] S. A. Payne, et al., “Laser properties of a new average-power Nd-doped phosphate glass,” Appl. Phys. B 61, Issue 3, pp. 257-266, 1995.

[18] A. Polynkin, et al., "Watts-level, short all-fibre laser at 1.5 mm with a large core and diffraction-limited output via intracavity spatial-mode filtering," Opt. Lett. 30, pp. 403-405, 2005.

[19] Y. W. Lee, et al., “20 W single-mode Yb^{3+}-doped phosphate fiber laser,” Opt. Lett., vol. 31, pp. 3255-3257, 2006.

[20] Y. W. Lee, et al., “Measurement of high photodarkening resistance in heavily Yb^{3+}-doped phosphate fibres,” Electron. Lett. 44, No. 1, pp. 14-16, 2008.

[21] J. Lousteau et al., “Photonic glasses for IR and mid-IR spectral range,” International Conference on Space Optics, Ajaccio (France), October 9th-12th 2012.

Chapter 2

Optical fibre

After a recall of basic optical concepts such as the refractive index of a medium and the refraction of light at a boundary between different media, in this chapter the basic structure of an optical fibre is introduced. Then the transmission of light along the fibre is described using two theories: the ray theory, or geometrical optics, and mode theory, or wave representation. Main mechanisms behind the attenuation of light travelling in a fibre are also discussed.

The second part of the chapter is dedicated to the main fibre fabrication methods with a particular attention to the preform drawing method used to fabricate the Nd^{3+}-doped double cladding (DC) optical fibre realized in this PhD research activity. A description of the optical tower facility hosted in our research laboratory is also added.

2.1 Refractive index

An electromagnetic wave travelling in a dielectric medium polarizes, through the oscillating electric field, the molecules of the medium at the frequency of the wave. As a consequence, the speed of light in a medium is lower than in vacuum, where there are no dipoles with which the field can interact. The ratio between the speed of light in free space *c* and its speed in a medium *v* is called the ***refractive index n*** of the medium:

$$n = \frac{c}{v} \tag{2.1}$$

The velocity of an electromagnetic wave traveling in a dielectric medium can be expressed as:

$$v = \frac{1}{\sqrt{\varepsilon_r \varepsilon_0 \mu_0}} \tag{2.2}$$

where ε_r is the *electrical relative permittivity*, ε_0 the and μ_0 are the *electrical* and *magnetic permittivity* of the vacuum.

If the wave travels in vacuum, $\varepsilon_r = 1$, and thus:

$$v = \frac{1}{\sqrt{\varepsilon_0 \mu_0}} = c = 3 \cdot 10^8 \, ms^{-1} \tag{2.3}$$

Hence the refractive index can also be expressed as:

$$n = \sqrt{\varepsilon_r} \tag{2.4}$$

Since the relative permittivity of the material depends on the frequency of the wave, because of the different polarization mechanism involved at low and high frequencies, the refractive index of the medium is also frequency (wavelength) dependent.

The dependence of the refractive index on the wavelength of a material is called ***dispersion*** and can be expressed by *Abbe number* defined as:

$$\upsilon_d = \frac{n_d - 1}{n_F - n_C} \tag{2.5}$$

where n_d, n_F, n_C are the refractive indices for the d-line of He (587.56 nm), the F-line of H (486.13 nm) and the C-line of H (656.27 nm), respectively. A small Abbe number means high dispersion of the material.

The relation 2.5 apply within the range where there is a linear relationship between the polarization *P* and electric field *E*:

$$P = \chi^1 E \tag{2.6}$$

where the proportionality coefficient χ^1 is called *linear electrical susceptibility*. However, in case of high electric field (for example under the irradiation of high

intensity laser beam), the induced polarization increases nonlinearly with applied field and can be expressed as:

$$P = \chi^1 E + \chi^2 E^2 + \chi^3 E^3 \tag{2.7}$$

where, the coefficients χ^2 and χ^3 are called *second and third order nonlinear susceptibilities*, respectively.

In an isotropic material like glass, the second-order nonlinear susceptibility χ^2 is zero and the nonlinearity at orders higher than four is negligible. Thus equation 2.7 becomes:

$$P = \chi^1 E + \chi^3 E^3 \tag{2.8}$$

Therefore, the refractive index of a glass n also varies with the intensity I of light and can be expressed as:

$$n = n_0 + n_2 I \tag{2.9}$$

where n_0 is the *linear refractive index* when the relation in Equation 2.6 holds, and n_2 is the *nonlinear refractive index*, expressed in m^2/W [1].

The field of non-linear optics is based on the application of the above defined non-linear refractive index.

2.2 Refraction of light and total internal reflection

When a light ray encounters the boundary between two different transparent media, with different refractive index n_1 and n_2, part of the ray is reflected back into the first medium while part of the ray is refracted (see Fig. 1.1).

The reflected ray follows the law of reflection which states that the angle of incidence θ_1 is equal to the angle of reflection.

The relationship between the incident and the refracted rays at the boundary is described by *Snell's law*:

$$n_1 \sin\theta_1 = n_2 \sin\theta_2 \tag{2.10}$$

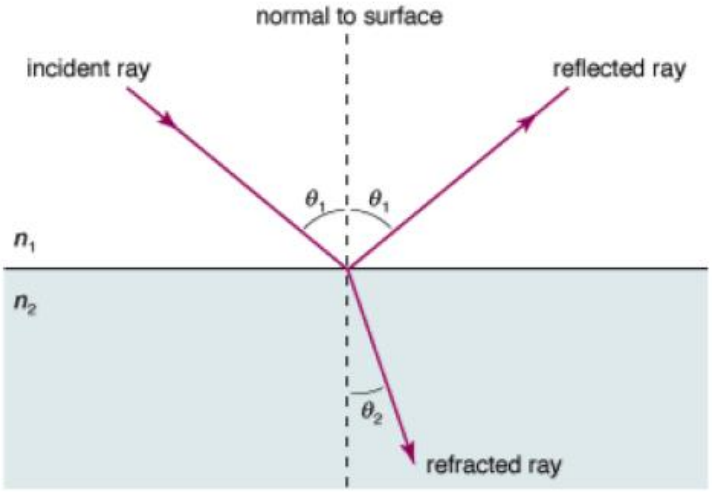

Figure 1.1. Light reflection and refraction at a boundary between media of different refractive index.

where θ_1 is the angle of incidence and θ_2 is the angle of refraction. If the wave passes from a less dense to a denser medium, it is bent toward the normal, and the angle of refraction is less than the angle of incidence. On the contrary, if the wave passes from a denser to a less dense medium, it is bent away from the normal, and the angle of refraction is greater than the angle of incidence.

As the angle of incidence θ_1 becomes larger, the angle of refraction θ_2 approaches 90 ° until a point where no refraction is possible. The light ray is then totally reflected back into the glass medium and no light escapes into the air. This condition is called ***total internal reflection (TIR)*** and the angle θ_c at which TIR occurs is called the *critical angle*.

The critical angle is determined by using Snell's Law and it is given by:

$$\sin\theta_c = \frac{n_2}{n_1} \tag{2.11}$$

The condition of total internal reflection is an ideal situation. However, in reality, there is always some light energy that penetrates the boundary. This situation is explained by the mode theory of light [2].

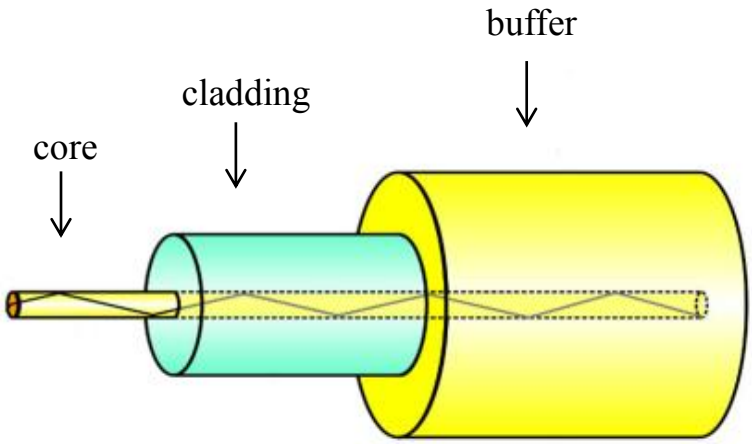

Figure 2.2. General structure of an optical fibre.

2.3 Basic structure of an optical fibre

An optical fibre is a thin cylindrical structure made of dielectric material transparent in the visible and near infrared (NIR) region of the electromagnetic spectrum, which acts as a dielectric waveguide by guiding light from one end to the other.

The basic structure of an optical fibre (see Fig. 2.2) consists of three parts: the ***core***, the ***cladding***, and the ***coating*** or buffer. The core is a cylindrical rod of dielectric material where light propagates and it is generally made of glass. The core is surrounded by a layer of material called cladding, which has a smaller refractive index with respect to the core, condition required for light confinement in the core region. The cladding is generally made of glass or plastic. The cladding performs also the following functions:

- reduces loss of light from the core into the surrounding air;
- reduces scattering loss at the surface of the core;
- protects the fibre from absorbing surface contaminants;
- adds mechanical strength.

Outside the cladding, there is typically a protective polymer coating, called buffer, which gives the fibre improved mechanical strength and protection against moisture and physical damage. The buffer also prevents the optical fibre from scattering losses caused by micro bends.

2.4 Light propagation along an optical fibre

The transmission of light along an optical fibre can be described by two theories. The first is ray theory, or geometrical optics, that describes light as a simple ray. This approach gives a clear picture of the propagation of light along the fibre and it is used to approximate the light acceptance and guiding properties of optical fibres. The second is mode theory, or wave representation, approach where light is described as an electromagnetic wave. This theory describes the behaviour of light within an optical fibre and it is useful to explain optical fibre properties like absorption, attenuation, and dispersion.

2.4.1 Ray theory

Two types of rays can propagate along an optical fibre. The first type is made of rays that pass through the axis of symmetry of the fibre and are called *meridional* rays. They are used to illustrate the basic transmission properties of optical fibres. The second type consists of rays that travel in a helical path through the fibre and never cross its axis; they are called *skew rays*.

Meridional rays can be classified as *bound* or *unbound* rays: bound rays remain in the core and propagate along the axis of the fibre by total internal reflection while unbound rays are refracted out of the fibre core. This in an ideal case where the core-cladding interface is perfect. However, imperfections at the core-cladding interface will cause part of the bound rays to be refracted out of the core into the cladding and escaping from the fibre. In general, meridional rays follow the laws of reflection and refraction.

In order to be guided along the optical fibre, a light ray incident on the fibre must be within a certain cone, known as the *acceptance cone*. The half-angle of this cone is called the *acceptance angle*, α_{max}. Its value depends on fibre properties and transmission conditions.

Suppose that the incidence angle at the end of the fibre core is α, and inside the fibre the ray makes an angle θ with the normal of the fibre axis. If the angle θ is smaller than the critical angle θ_c, the ray will escape into the cladding; on the contrary, if θ is greater than the critical angle θ_c the ray will be guided along the fibre by TIR (see Fig. 2.3).

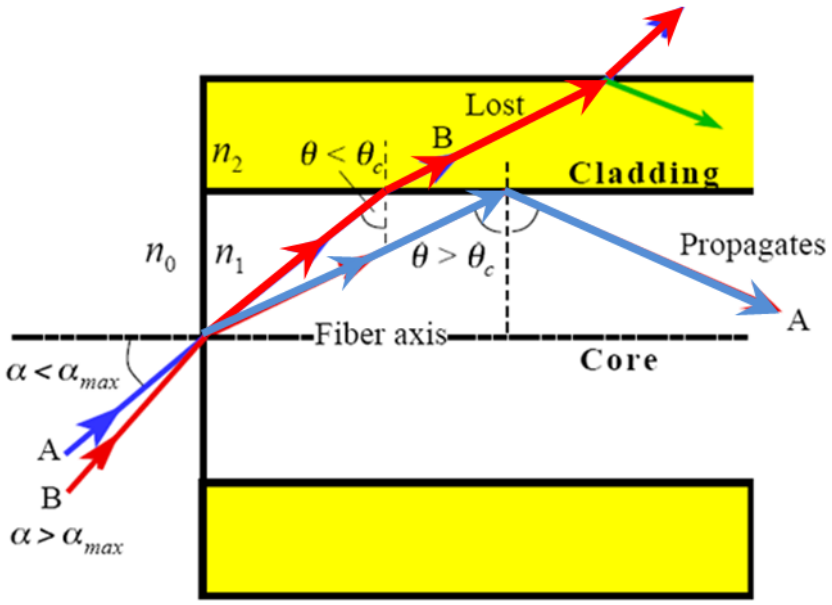

Figure 2.3. Acceptance angle of an optical fibre and total internal reflection. Adapted from [2].

The maximum value admitted for α, is the one for which $\theta = \theta_c$. At the interface n_0/n_1, from Snell law it can be written:

$$n_0 \cdot sin\, \alpha_{max} = n_1 \cdot sin\left(\frac{\pi}{2} - \theta_c\right) \tag{2.12}$$

being at the same time for TIR:

$$n_1 \cdot sin\, \theta_c = n_2 \cdot sin\left(\frac{\pi}{2}\right) \tag{2.13}$$

thus by substituting for θ_c:

$$sin\, \alpha_{max} = \frac{\left(n_1{}^2 - n_2{}^2\right)^{1/2}}{n_0} \tag{2.14}$$

The ***numerical aperture NA*** of the fibre is a characteristic parameter defined by:

$$NA = \left(n_1{}^2 - n_2{}^2\right)^{1/2} \tag{2.15}$$

So in terms of NA, the acceptance angle can be defined as

$$sin\ \alpha_{max} = \frac{NA}{n_0} \tag{2.16}$$

The angle $2\alpha_{max}$ is called the total acceptance angle and depends on the NA of the fibre and the refractive index of the launching medium. This equation is strictly applicable only for meridional rays.

The NA is a convenient way to measure the light-gathering ability of an optical fibre. It can be used to measure the efficiency of light coupling between a source and a fibre. Typical values of NA range from 0.1 to 0.3 for glass fibres. Plastic fibres generally have a higher NA, also up to 0.50.

Skew Rays propagate without passing through the fibre axis. The acceptance angle for skew rays is larger than the one of meridional rays, thus they increase the amount of light capacity of a fibre. They propagate in a helical motion, consequently they take longer paths which increase their attenuation considerably. Skew rays tend to propagate in the annular region near the edge of the fibre core and so a large portion of them are considered to be leaky rays. Skew rays exist only for short lengths of fibres < 100 m.

2.4.2 Mode theory

Mode theory uses electromagnetic wave behaviour to describe the propagation of light along a fibre. It is useful for describing properties of light that ray theory is unable to explain.

Light wave can be represented as a plane wave, which is described by its direction, amplitude, and wavelength of propagation. A plane wave is a wave whose wavefront (surfaces of constant phase) is made of infinite parallel planes of constant amplitude normal to the direction of propagation.

The wavelength λ of the plane wave is given by:

$$\lambda = \frac{c}{fn} \tag{2.17}$$

where c is the speed of light in a vacuum, f is the frequency of the light, and n is the index of refraction of the plane-wave medium.

Figure 2.4 shows the direction and wavefronts of plane-wave propagation along the fibre. Not all wavefronts incident on the fibre at angles less than or equal to light acceptance angle propagate along the fibre. Wavefronts have to remain in phase for light to be transmitted along the fibre. If propagating wavefronts are not in phase, they

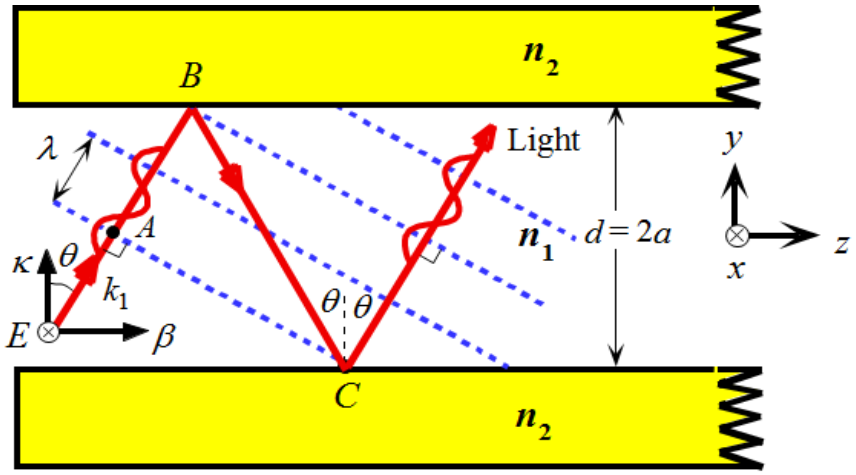

Figure 2.4. Wavefront propagation along an optical fibre. The light ray must interfere constructively with itself to propagate successfully [2].

eventually disappear because of destructive interference. This interference is the reason why only a finite number of modes can propagate along the fibre.

The modes of the fibre are then a set of guided electromagnetic waves in the optical fibre. Each mode of propagation is identified with a mode number m = 0, 1, 2, ... Figure 2.5 shows the electric field pattern of the first three modes (m = 0,1,2) traveling wave along the fibre. It can be observed that the mode number indicates the number of field maxima within the core of the fibre. Generally, modes with more than a few (5-10) field

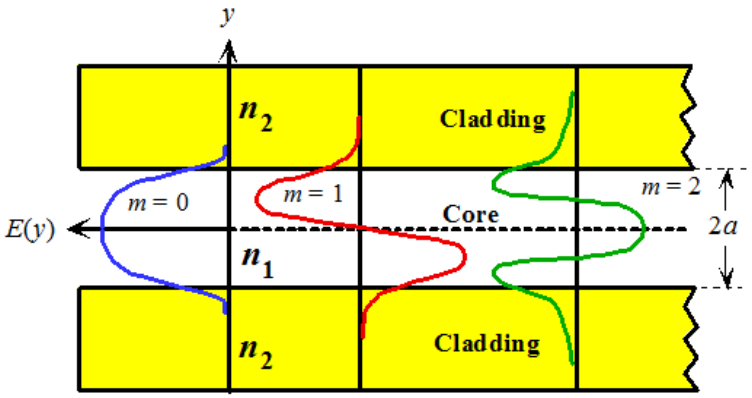

Figure 2.5. Electric field pattern of the first three modes (m=0,1,2) traveling wave along the fibre [2].

maxima are called *high order modes*. It can also be observed that the modes are not confined in the core of the fibre, but penetrate partially into the cladding material. While the low order mode are concentrated near the centre of the fibre, higher order modes are distributed more towards the external surface of the fibre. Thus a portion of light could be refracted out of the core and be trapped into the cladding. These modes are called *cladding modes*.

The order of the mode is also determined by the angle the wavefront makes with the axis of the fibre: high order modes cross the axis of the fibre at steeper angles compared to low order modes, while the lowest mode (m= 0) travels nearly parallel to the fibre axis. A light pulse (Fig. 2.6) that enters a waveguide structure will thus be broken into various modes that propagate at different group velocity inside the guide. Therefore the signal emerging at the end of the guide will become broader than the input pulse.

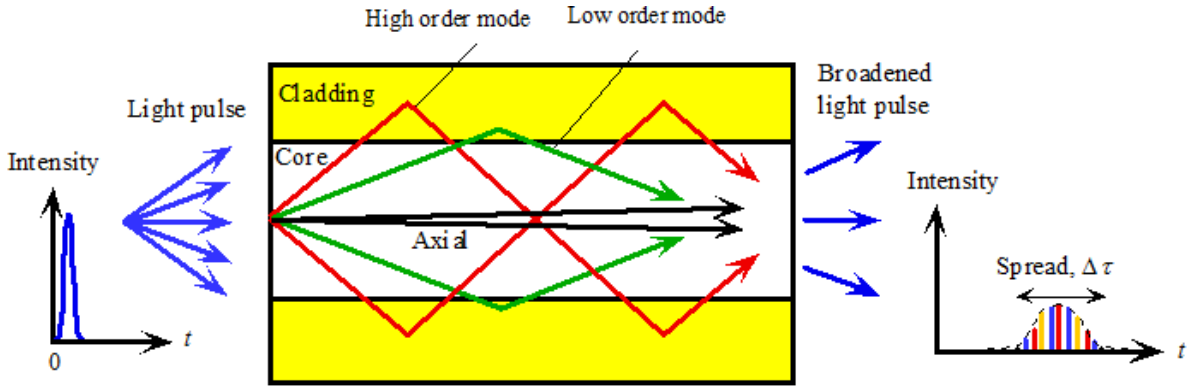

Figure 2.6. Schematic illustration of a light pulse travelling in a waveguide structure. The signal is broken into various modes that propagate at different group velocity inside the guide. Therefore the signal emerging at the end of the guide will be broader than the input pulse [2].

A last type of modes are the *leaky modes* that lose power as they propagate along the fibre. Generally, modes leaked into the cladding are lost in a few centimetres. However, leaky modes can carry a large amount of power in short fibres.

There is an important parameter that describes how many modes a fibre can support: the ***normalized frequency V***. It is a dimensionless quantity defined as:

$$V = \frac{2\pi a}{\lambda}\left(n_1{}^2 - n_2{}^2\right)^{1/2} = \frac{2\pi a}{\lambda}\, NA \qquad (2.18)$$

where n_1 is the core index of refraction, n_2 is the cladding index of refraction, a is the core radius, and λ is the wavelength of light in air.

For a given wavelength λ, the V number depends on the waveguide geometry (a) and properties (n_1 and n_2), so it is a characteristic parameter of the optical fibre.

It can be demonstrated that for $V \leq 2.405$ only the fundamental mode propagates along the fibre, while high order modes are lost in the cladding. This kind of fibre is called ***single mode (SM)***. For low V values (≤ 1.0), most of the power is propagated in the cladding material and it is easily lost at fibre bends. Hence, the value of V should remain near the 2.405 level.

When $V > 2.405$, the number of modes propagating along the fibre increases sharply, even above 100. This kind of fibre is called ***multimode (MM)***. For large values, the number of supported modes of a fibre can be calculated approximately as:

$$M = \frac{4}{\pi^2} V^2 \tag{2.19}$$

2.5 Optical Fibre types

Optical fibres are characterized by their structure and by their properties of transmission. They can be classified by the number of modes that propagate along the fibre into two types: single mode and multimode fibres. The basic structural difference between these two types is the core size, since core size is strictly related to the number of mode propagating in a fibre (see paragraph 2.4.2).

Optical fibres can be also classified by the refractive index profile of the core/clad structure which determines the mode of propagation of the optical signal. The most common types are the step-index and graded-index fibres.

2.5.1 Single Mode and multimode fibres

The core size of single mode fibres is small, typically around 8 to 10 μm. A fibre core of this size allows only the fundamental or lowest order mode to propagate around a 1300 nm wavelength. As already discussed, for single mode fibres V is less than or equal to 2.405.

The core size of typical multimode fibres is from 50 to 100 μm, with NA between 0.20 to 0.29, respectively. The number of modes propagating in a multimode fibre depends on the core size and NA. As the core size and NA increase, the number of modes increases above 100 modes.

Single mode fibres have many advantages as compared with the multimode:

- small attenuation (0.15 dB/km)
- high transmission bandwidth
- low fibre dispersion.

However due to smaller core size light coupling from an external source is more critical than in a multimode fibre. As a consequence, single mode fibres typically require laser diodes while multimode can be coupled to light emitting diodes (LEDs) that are less complex and cheaper than lasers.

Nonetheless the use of multimode fibres has the disadvantage of modal dispersion that increases with the number of supported modes. This effect causes the light pulse to be spread during propagation in the fibre and thus decreases system bandwidth.

2.5.2 Step-index and graded-index fibres

Step-index optical fibres have a refractive index profile of the core/clad structure characterized by a uniform refractive index within the core and a sharp decrease in refractive index at the core-cladding interface so that the cladding has a lower refractive index (see (a) and (b) in Fig. 2.7). The step-index profile corresponds to a power law index profile with the profile parameter approaching infinity. The step-index profile is used in most single mode fibres and some multimode fibres.

A *graded-index fibre* means that the fibre core has a refractive index that decreases with increasing radial distance from the optical axis of the fibre, as represented in Fig. 2.7 (c).

Because the part of the core closer to the fibre axis have a higher refractive index than the parts near the cladding, light rays follow sinusoidal paths down the fibre. The most common refractive index profile for a graded-index fibre is very nearly parabolic. These types of fibres are designed to compensate for the difference in the propagation path length among various modes so that the distortion of the signal is minimized.

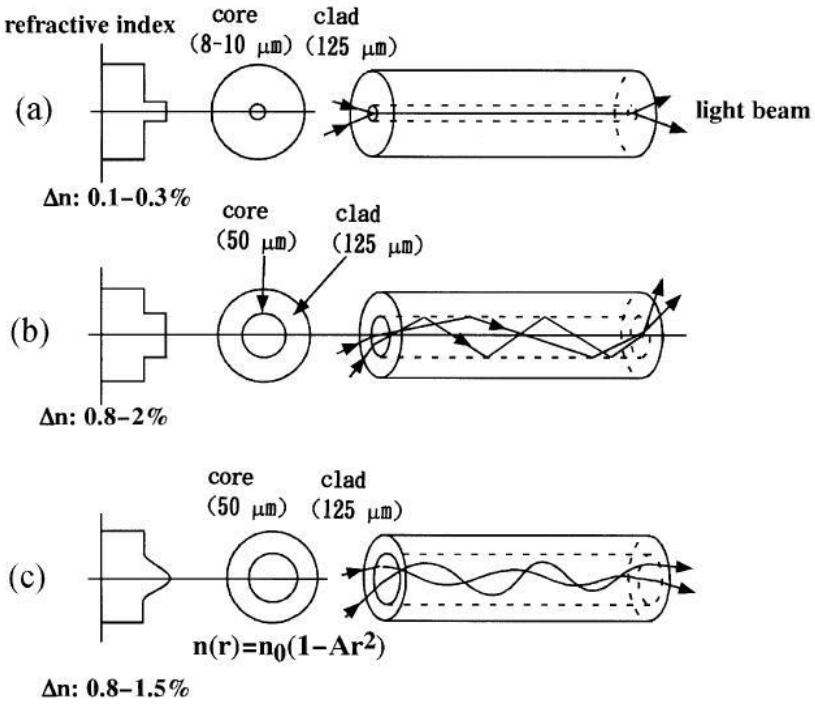

Figure 2.7. Typical structure of optical fibre for telecommunications: (a) single-mode fibre; (b) multimode fibre of step-index type; (c) multi-mode fibre of graded-index type [1].

Multimode optical fibre can be manufactured with either graded-index or step-index. The advantage of the graded-index compared to step-index is the considerable decrease in modal dispersion.

More unusual refractive index profile of the core/clad structure can be realized. There are for example *"W profiles" fibres*, where the core is surrounded by a region with a refractive index lower than that of the cladding (depressed cladding). Triangular, trapezoidal and Gaussian index profiles are used for dispersion-shifted fibres. Moreover index profiles do not need to be cylindrical. For example, an elliptical core shape can provide increased birefringence (for polarization-maintaining fibres) or even single-polarization guidance [3].

In addition, there are photonic crystal fibres, where the refractive index profile is strongly structured.

2.6 Attenuation of an optical fibre

Attenuation is the loss of optical power of a light beam travelling along a fibre. It is mainly a result of light absorption, scattering and bending losses.

In an optical fibre having a length L, an input power P_{in} and an output power P_{out}, attenuation is defined as a unit of length by the following equation:

$$\alpha_{dB} = \frac{1}{L} \cdot 10 \cdot Log\left(\frac{P_{in}}{P_{out}}\right) \tag{2.20}$$

Attenuation is a log relationship. If length is expressed in kilometres, therefore, the unit of attenuation is decibels/kilometre (dB/km).

2.6.1 Absorption

Absorption is a major cause of signal loss in an optical fibre. It is defined as the reduction of optical power due to conversion in internal energy of the absorber, such as thermal energy. Absorption in optical fibres is due to three factors:

- imperfections in the atomic structure of the fibre material;
- intrinsic factors due to fibre/material properties;
- extrinsic factors due to presence of impurities in the fibre/material.

Imperfections in the atomic structure induce absorption by the presence of missing molecules or oxygen defects.

Intrinsic absorption is caused by basic fibre material properties. Intrinsic absorption sets the minimal level of absorption in a fibre, in fact it would be present also in a fibre absolutely pure, with no imperfections or impurities. The most widespread optical fibres are the silica ones, because of their low intrinsic material absorption at the wavelengths of operation.

A first intrinsic material mechanism is due to the interaction of light with atomic electrons that are excited to a higher energy level. The absorption peak is in the UV region, but its tail extends to the NIR region, where usually optical fibres are intended to be operated (see Fig. 2.8).

Another intrinsic material mechanism is due to the interaction of light with molecular vibrations, the peak of absorption is in the IR (~ 10 μm for silica) with tail extending in the NIR region. In silica glass, absorption is caused by the vibration of silicon-oxygen (Si-O) bonds (see Fig. 2.8).

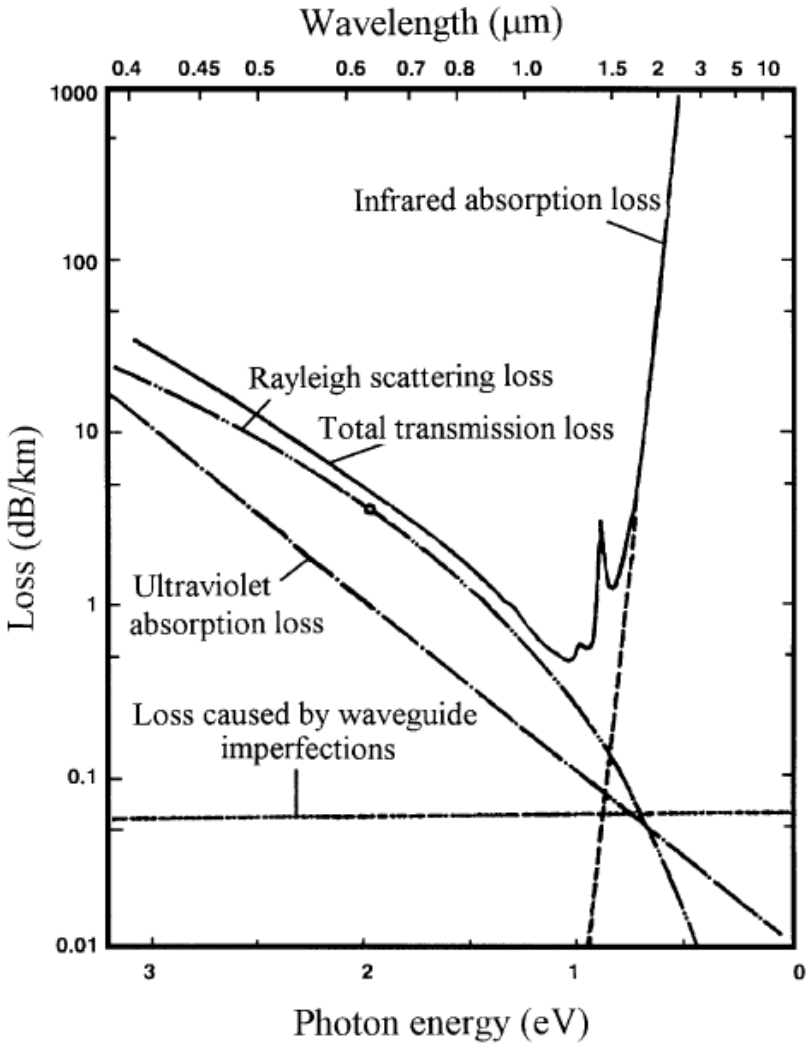

Figure 2.8. Fundamental loss mechanisms in silica fibres [1].

The wavelength giving the minimum intrinsic loss varies from glass to glass depending on the type and amount of the constituents. Silica based glass used for optical fibres shows a theoretical minimum loss of 0.125 $dB \cdot km^{-1}$ at 1.55 μm.

Extrinsic absorption is caused by impurities in the glass matrix. Particularly harmful are transition metal ions, such as iron, nickel, and chromium whose concentration must

be maintained lower than one part per billions. Extrinsic absorption is caused by the electronic transition of these metal ions from one energy level to another. In modern commercial fibres, due to the high quality standard of fibre fabrication, the contribution of these contaminants to total loss is negligible [4].

Extrinsic absorption also occurs when hydroxyl ions (OH^-) are introduced into the fibre. For example in silica glass, water forms a silicon-hydroxyl (Si-OH) bond that has a fundamental absorption at 2700 nm. However, the harmonics or overtones of the fundamental absorption occur in the region of operations: 1383 nm, 1250 nm, and 950 nm. These absorption peaks has defined historically three main windows of operation for optical telecommunication systems. A first window centred at 850 nm, a second window at 1300 nm and a third window at 1550 nm. Fibre optic systems operate at wavelengths defined by one of these windows.

The amount of water (OH^-) impurities present in a fibre should be less than a few parts per billion.

2.6.2 Scattering

Scattering losses are caused by interaction of light with compositional fluctuations of thermodynamic origin in glass material. Light traveling through the fibre interacts with these areas as they were small dielectric particles, and it is partially scattered in all directions.

If the size of these compositional fluctuations is less than one-tenth of the operating wavelength of light (λ), Rayleigh scattering occurs. Loss caused by Rayleigh scattering is inversely proportional to the fourth power of the wavelength ($1/\lambda^4$). Rayleigh scattering is the main loss mechanism between the UV and IR regions (see Fig. 2.8). Nothing can be done to eliminate this scattering in glasses because it is part of their intrinsic structure. [2]

If the size of these compositional fluctuations areas is comparable with λ, Mie scattering occurs. This scattering is less wavelength dependent than Rayleigh one. However, in commercial fibres, due to the high quality standard of fibre fabrication, the effect of Mie scattering is negligible.

2.6.3 Bending

Bending losses are classified according to the bend radius of curvature: microbend losses or macrobend losses.

Microbends are small microscopic bends of the fibre axis that largely arise when a fibre is coated or cabled improperly, causing small discontinuities or imperfections in the fibre. External forces are also a source of microbends. Microbend losses increase attenuation because low order modes become coupled with high order modes, and thus can leak out of the fibre.

Macrobend losses are observed when a fibre bend's radius of curvature is large compared to the fibre diameter. These bends become a great source of loss when the radius of curvature is less than several centimetres. The bends affect mode field diameter that is the field penetration into the cladding. Some of these increased cladding fields will be lost in the outer medium.

2.7 Fibre manufacturing

To obtain a good optical fibre, high quality precursors are necessary, since occurrence of impurities in the materials degrades the optical properties of the fabricated fibre.

There are two main methods to produce an optical fibre:

- drawing from double crucible;
- preform drawing.

The double crucible method (Fig. 2.9) produces a fibre by directly pulling the glass from concentric reservoir containing the molten core glass and molten cladding glass. This method may be used for special glass compositions, when high purity and thus low optical loss are not a crucial issue, or with compositions that cannot be deposited from the vapour phase. Double crucible method is usually employed for soft glass fibres and is limited to step index fibres.

Most glass fibres are fabricated using the second method: preform drawing. ***Preform*** is a term conventionally used among optical fibre manufacturer to indicate the glass rod from which the optical fibre is drawn from. It can be regarded as a larger scale optical fibre with the same refractive index and waveguide structure as the drawn optical fibre.

Preform drawing involves two important steps:

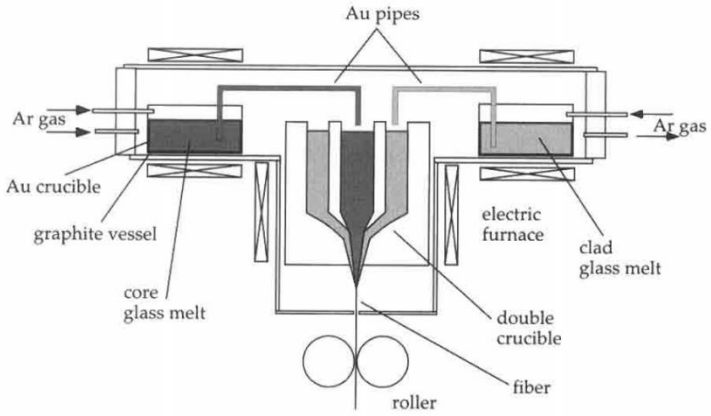

Figure 2.9. The double crucible method of fluoride fibre fabrication [5].

- preform fabrication;
- fibre drawing.

These steps will be described in more details in the following paragraphs.

2.7.1 Preform fabrication

Many fibre preforms, especially those based on silica glasses, are fabricated with a process called ***modified chemical vapour deposition (MCVD)***. This method was developed for silica telecom fibres in the 1970s.

A mixture of oxygen, silicon tetrachloride ($SiCl_4$), germanium chloride ($GeCl_4$) and/or other chemicals is conducted inside a rotating silica glass tube, which is heated from outside to ~ 1600 °C with a torch. Chemical reactions in the gas form a fine soot of silica (and possibly other substances) which coats the inner surface of the glass tube near the flame and is sintered into a clear glass layer. The torch is continuously moved up and down along the tube. Towards the end of the process, the gas mixture is modified to form a layer with higher refractive index, the precursor of the fibre core. Finally, the tube is collapsed by heating it to ~ 2000 °C.

Various alternative vapour deposition methods have been developed; in the following the main methods will be briefly described (see for reference Fig. 2.10).

1. *Outside vapour deposition* (OVD) is a process where the silica soot is deposited on the outer surface of a small diameter rod made of refractory material (usually Al_2O_3

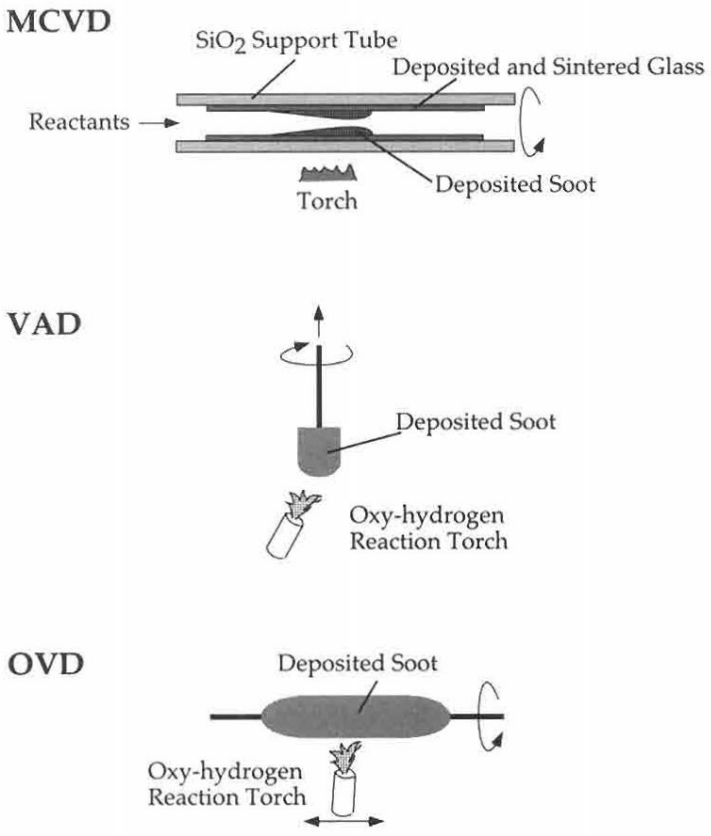

Figure 2.10. Vapour deposition methods for fibres preform fabrication [5].

or graphite) which constitutes the support of the preform and is extracted at the end of the deposition process. The rod is rotated during the process and exposed to the flame of a deposition burner. Together with the material precursors such as $SiCl_4$, a fuel gas such as hydrogen or methane is supplied to the burner which is moved along the rotating rod. After the deposition, the target rod is removed, and the preform is consolidated in a furnace in chlorine and helium flow at high temperature (over 500 °C) to facilitate removal of the hydroxyl content.

2. *Vapour phase axial deposition* (VAD) is similar to OVD, but while in this latter the preform growth is radial, in VAD is axial and the preform must be gradually extracted from the deposition chamber. This method allows manufacturing of very long preforms. Consolidation of the material can be done in a separate zone with respect to the melting process. An important difference to OVD and MCVD is that

the doping profile is determined only by the burner geometry, rather than by a variation of the gas mixture over time. The major disadvantage is the complexity of the burners, which must be constructed ad hoc for each type of refractive index profile.

3. *Plasma chemical vapour deposition* (PCVD) uses deposition inside a tube, similar to MCVD. However, the burner is replaced by a microwave cavity resonator for heating the deposition region. The deposition is slow, but very precise. There is also *plasma-enhanced chemical vapour deposition* (PECVD), operating at atmospheric pressure with fairly high deposition rate.

Using vapour deposition methods extremely low propagation losses (< 0.2 dB/km) can be achieved, because very high purity materials can be used and contamination is avoided. Moreover, when no hydrogen is present (e.g. as fuel gas), the water content of such preforms is very low, avoiding a strong loss peak at 1.4 μm, which would affect the telecom band.

A big challenge in CVD methods is to introduce RE ions in the preform, because they suffer from low volatility in the vapour phase. Solution doping/MCVD allows incorporation of RE chloride precursors.

In case of preform based on heavy metal oxide glasses and non-silicate glasses, whose precursors cannot be obtained in the vapour phase, the fabrication method usually employed is the ***rod-in-tube*** technique. A rod of a glass with higher refractive index is inserted into a glass tube with lower refractive index, but with similar chemical and physical properties (see Fig. 2.11). Both can be reasonably well connected during the following drawing process, but great care is required to avoid bubbles and contaminating particles at the core-cladding interface, causing light scattering and absorption. To avoid this, the glass surfaces must be thoroughly cleaned before the drawing process, preferably in a controlled dust-free atmosphere.

The Nd^{3+}-doped DC optical fibre realized in this PhD research activity was fabricated by preform drawing, while the preform was realized by rod-in-tube technique. All the details on the fabrication process will be given in Chapter 5.

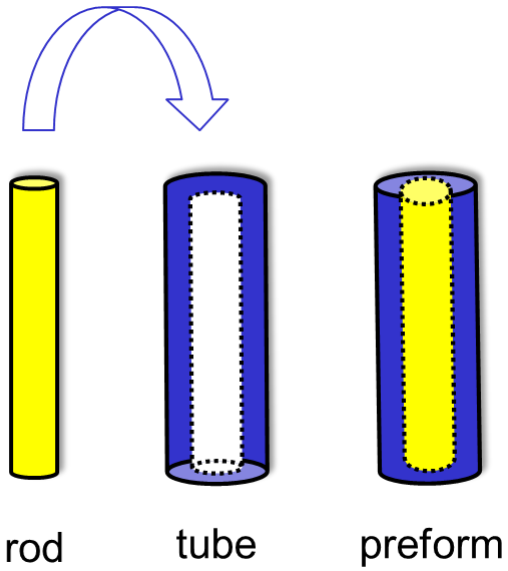

Figure 2.11. Scheme of the rod-in-tube method.

2.7.2 Preform drawing

Optical fibres are produced from preforms using a process called ***drawing***. This process involves a gradual reduction of the diameter of the preform down to that of the fibre without changing the optical properties and the refractive index profile built into the preform. Diameter reduction occurs at a temperature above the material's softening point, in vertical conditions. The choice of drawing temperature depends first of all on the glass type and the possible dopant (i.e. the curve of viscosity versus temperature) and then on the preform diameter, drawing rate and furnace dimensions. The zone at which diameter reduction occurs, called *neck-down*, coincides approximately with the zone at which the material reaches its maximum temperature.

A typical drawing tower (see Fig. 2.12) is composed by:

- a vertical rigid support structure to which all elements are secured;
- a feed mechanism that gradually inserts the preform into the furnace below;
- a high temperature furnace;
- a fibre diameter measurement system;
- an optional coating system;
- a drum for drawing and collecting the fibre.

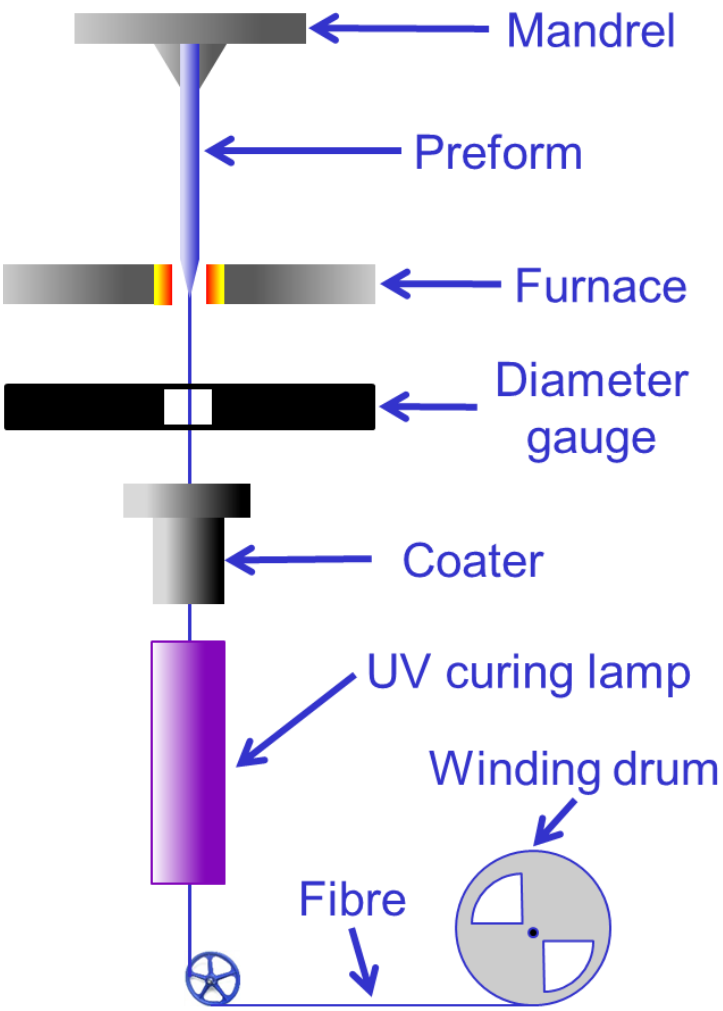

Figure 2.12. Schematic of a drawing tower for optical fibre.

The height of a drawing tower may vary from a few meters to 15 meters or more depending on the fibre materials (i.e. the working temperature), preform dimensions, as well as the number of elements secured to the support.

The drawing tower facility of our research group is the only example in Italy of a glass fibre R&D draw tower.

The preform is fed into the furnace by a motorized linear stage (PI-MICOS VT-75) with 6 µm repeatability and up to 600 mm travel range.

The furnace consists in a graphite ring heated by a RF inductor operating at 248 kHz (SAET, Torino). The furnace provides the thermal energy necessary for drawing and a

laser micrometre (Zimmer 460 A2) is used for monitoring fibre diameter during the drawing process.

The fibre tension is measured online by a tension meter (AE1CM, ASA automazione). The winding drum is operated by a brushless electronically commutated motors (EC) motor (Maxon EC 60). Preforms are drawn into fibres under an inert atmosphere.

The UV coater is not installed at the moment in the drawing tower.

The drawing process (except the inductor settings) is controlled by a Labview programme that was ad hoc developed as part of the work of this thesis (see Fig. 2.13).

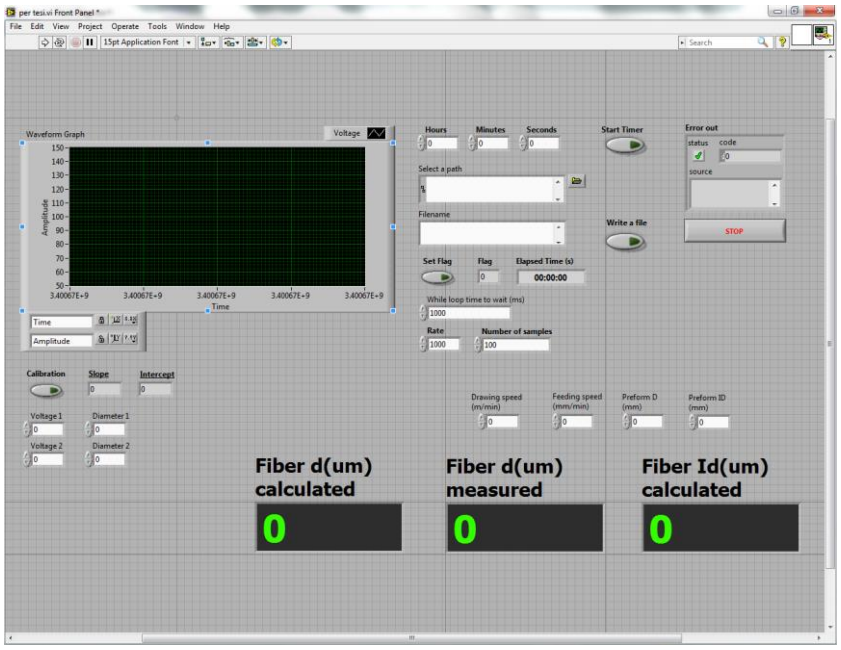

Figure 2.13. User interface of the Labview programme used to control the drawing process.

By setting the preform feed rate into the furnace V (µm/s) and the drawing speed v (m/min), knowing the preform diameter D, the programme calculates the estimated fibre diameter d. In fact, neglecting the material losses which occur through preform vaporization inside the furnace, it should be:

$$D^2 \cdot V = d^2 \cdot v \tag{2.20}$$

Then, during all the drawing process, the programme monitors the measured fibre diameters through a National Instrument acquisition board (NI USB-6008) and plots it in a graph on the screen.

The programme was also developed in view of drawing of hollow fibre, thus calculates a fibre inner diameter I_d, although at the moment no measurement system was implemented for the online measurement of this diameter.

All the data concerning the drawing are then saved in a text file for following analysis.

REFERENCES

[1] M. Yamane and Y. Asahara, “Glasses for Photonics,” Cambridge University Press, 2004.

[2] S. O. Kasap, “ Optoelectronics and Photonics: Principles and Practices,” Upper Saddle River: Prentice-Hall, 2001.

[3] http://www.rp-photonics.com

[4] http://www.cedengineering.com.

[5] P. C. Becker, N. A. Olsson, and J. R. Simpson, “Erbium-doped Fiber Amplifiers-Fundamentals and Technology,” Academic Press Inc, San Diego, Calif, USA, 1997.

Chapter 3

Fibre laser

Fibre lasers are today not only one of the fastest growing photonic technologies, but are also a sound industrial reality since they are rapidly eroding the markets shares of the other laser technologies, thanks to their outstanding properties, such as high brightness, excellent mode quality, high efficiency and enhanced heat dissipation. They find applications in a variety of fields, including semiconductor device manufacturing, surgery, military technology, industrial material processing, remote sensing and scientific instrumentation.

In the first part of the chapter basic principle of laser action are reviewed, along with unique properties of laser light. The second part of the chapter presents the fundamental of RE solid state lasers, with a focus on Nd^{3+}-doped phosphate glass lasers.

In the last part of the chapter fibre lasers are introduced, along with their key advantages over the other solid state lasers, especially in terms of beam management and quality. At last, state of the art in the research on Nd^{3+}-doped phosphate fibre lasers is briefly reviewed.

3.1 Principle of laser action

3.1.1 Interaction of radiation with matter

The interaction between electromagnetic (EM) radiation and matter cause changes in the energy states of the electrons in matter.

To simplify the discussion, let us consider an idealized material with just two nondegenerate energy levels E_1 and E_2 having a populations of N_1 and N_2, respectively. The total number of electrons in these two levels is assumed to be constant:

$$N_1 + N_2 = N \tag{3.1}$$

We can identify three types of interaction between EM radiation and a simple two-level atomic system (see Fig. 3.1).

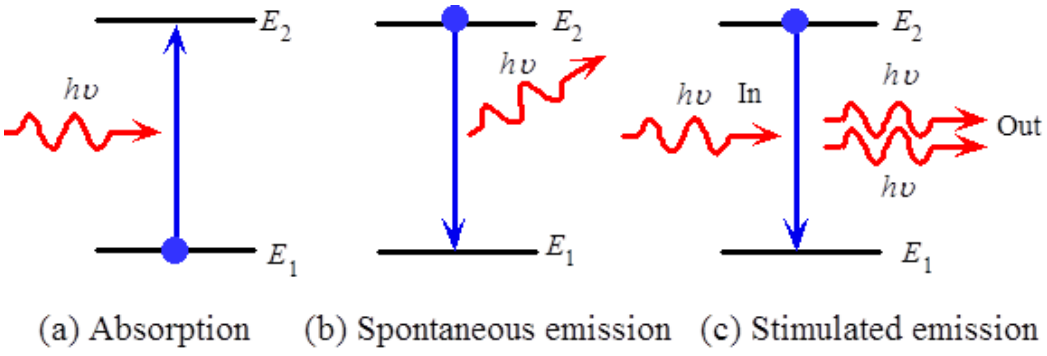

Figure 3.1. Interaction of radiation with matter [1].

Absorption: when a monochromatic EM wave of frequency ν enters a material, electrons can be raised from lower energy level E_1 to higher energy level E_2, if the photons energy equals the energy difference between the two levels:

$$h\nu = E_2 - E_1 \tag{3.2}$$

where h is the Planck constant (6.6×10^{-34} Ws^2).

The population of lower level will be depleted at a rate equal to:

$$\frac{dN_1}{dt} = -B_{12}\rho N_1 \tag{3.3}$$

where B_{12} is the Einstein's coefficient for stimulated absorption and has the units as m^3/s^{2}J, N_1 is the population in lower state and ρ is the energy density per unit of frequency of the incoming photons.

Spontaneous emission: after an electron has been raised to the upper energy level by absorption, there is a probability that it will return to the lower energy state emitting, in a random direction, a photon of energy equal to the energy difference between the two levels. The population of the upper level will be depleted at a rate equal to:

$$\frac{dN_2}{dt} = -A_{21}N_2 \tag{3.4}$$

where A_{21} is the Einstein's coefficient for spontaneous emission and has the units as s^{-1}.

It can be observed that this spontaneous decay of the upper level takes place in absence of an EM field. It is purely a statistical phenomenon related with time and space and is dependent on the lifetime of the excited state. If the transition lifetime is very large, it is considered as a forbidden transition.

If we consider a large number of spontaneously emitted photons there is no phase relationship between them, thus they are incoherent.

Equation (3.4) has a solution equal to:

$$N_2(t) = N_2(0)\exp\left(\frac{-t}{\tau_{21}}\right) \tag{3.5}$$

where τ_{21} is the lifetime for spontaneous radiation of level 2. This radiation lifetime is equal to the reciprocal of the Einstein coefficient:

$$\tau_{21} = {A_{21}}^{-1} \tag{3.6}$$

In general, the reciprocal of the transition probability of a process is called its ***lifetime*** and has the dimension of time (s). Typically, the spontaneous lifetime is of the order of 10^{-8} - 10^{-9} s. The shorter the spontaneous lifetime, the greater is the probability that spontaneous emission will occur. In certain materials, there are energy levels which have the spontaneous lifetime of the order of microseconds to a few milliseconds. These levels are known as ***metastable levels***. The probability of transitions involving metastable levels is relatively low.

Stimulated emission: emission takes place not only spontaneously but also under stimulation by EM radiation of the appropriate frequency ν, that satisfies equation 3.2.

In this case the emitted photon is in phase with the incoming photon, it is in the same direction, it has the same polarization and the same energy.

The population of the upper level will be depleted at a rate equal to:

$$\frac{dN_2}{dt} = -B_{21}\rho N_2 \tag{3.7}$$

where B_{21} is the Einstein's coefficient for stimulated emission and has the units of m^3/s^2J and ρ is the energy density per unit of frequency of the incoming photons.

In presence of external radiation, an atomic system emits a spontaneous radiation with a phase independent of that of the external one and a stimulated radiation in phase with the external one. The useful parameter for laser action is the B_{21} coefficient; the A_{21} coefficient represents a loss term and introduces a noise source in a laser.

Considering an ideal material in thermal equilibrium, where absorption, spontaneous emission and stimulated emission take place, it can be written:

$$B_{21}\rho N_2 + A_{21}N_2 = -B_{12}\rho N_1 \tag{3.8}$$

Using Boltzmann statistic and black body radiation law [1], it is possible to demonstrate that:

$$\frac{A_{21}}{B_{21}} = \frac{8\pi v^2 h v}{c^3} \tag{3.9}$$

$$B_{21} = B_{12} \tag{3.10}$$

These equations are known as Einstein's relations.

From 3.9 it is possible to observe that the ratio of the probability of spontaneous to stimulated light emission depends directly on the frequency of emission (or inversely to the wavelength). Hence, stimulated emission is more probable than spontaneous in the microwave region (reason of the early production of the maser [2]), while in the optical region, spontaneous emission is more likely than stimulated emission and this gets worse as we go into the UV region of the spectrum.

Equation 3.10 states that the Einstein coefficients for stimulated emission and absorption are equal. This means that, in steady state, the two processes have the same probability to happen.

The population density N_1 and N_2 in ground level E_1 and excited state E_2 can be estimated using Boltzmann's relationship as follows:

$$\left(\frac{N_2}{N_1}\right) = exp\left(-\frac{(E_2-E_1)}{KT}\right) \tag{3.11}$$

where K is the Boltzmann constant ($1.38 \cdot 10^{-23}$ J / K) and T the temperature (K).

From 3.11 derives that in a two level system the population of the upper level cannot exceed the population of the lower one. It follows that it is not possible to obtain photon amplification via stimulated emission with a two levels system.

It can be observed that the electrons could decay from level E_2 to level E_1 not only via radiative process, but also via nonradiative decay where the excitation energy is converted into vibrational quanta of the surroundings. The observed fluorescence lifetime τ_f of the excited state E_2 is thus given by the combination of the probabilities for radiative (A_{rad}) and nonradiative (W_{nr}) processes:

$$\frac{1}{\tau_f} = A_{rad} + W_{nr} = \left(\frac{1}{\tau_r}\right) + W_{nr} \tag{3.12}$$

where τ_R is the radiative lifetime. The nonradiative probability W_{nr} includes relaxation by multiphonon emission and energy transfer between ions.

The ***radiative quantum efficiency*** η is defined as:

$$\eta = A_{rad}/(A_{rad} + W_{nr}) = \tau_f/\tau_r \tag{3.13}$$

from which it can be concluded that to a higher fluorescence lifetime τ_f, will correspond a higher radiative quantum efficiency η.

In all the section, it has been considered the interaction between a monochromatic EM radiation wave with a two-level system with an infinitely sharp energy gap hv. An actual atomic system, however, has linewidth-broadened energy levels (the reason will be discussed in following sections). Then instead of simple Einstein's coefficients for the transitions between level E_1 and E_2, new parameters have to be introduced: *absorption and emission cross sections,* which are used to characterize laser materials. Transition cross sections can directly be obtained from spectroscopic measurements of material sample.

3.1.2 Three and four-level laser systems

As discussed above, when light is incident on the material, there is competition between absorption, spontaneous emission and stimulated emission processes. Under normal equilibrium conditions, the population of various levels is given by Boltzmann's statistic and thus N_2 will always be less than N_1.

In order to have the laser action is required to bring the atomic system in a non-equilibrium condition where $N_2 > N_1$. This non-equilibrium condition is known as ***population inversion***.

This condition could be obtained in a three-level system like the one represented in figure 3.2. Initially, all the electrons of the laser material are in the lowest energy level E_1. Assume that an external excitation causes the electrons of the system to be raised to the energy level E_3. This excitation process is called ***pumping***. If the pumping is accomplished through the use of light then it is called *optical pumping*.

In general, the pumping band, level E_3, is actually made up of a number of bands, so that the optical pumping can be achieved over a broad spectral range.

Most of the excited ions are transferred by fast radiationless transitions into the intermediate level E_2. In this process the energy lost by the electron is transferred to the lattice. E_2 is a metastable long-lived state that means that electrons cannot decay rapidly from it and thus they accumulate at this energy level causing a population inversion between E_2 and E_1.

When an electron decays spontaneously from E_2, it emits a photon that can cause a stimulated emission of a neighbouring electron. These two photons can again stimulate

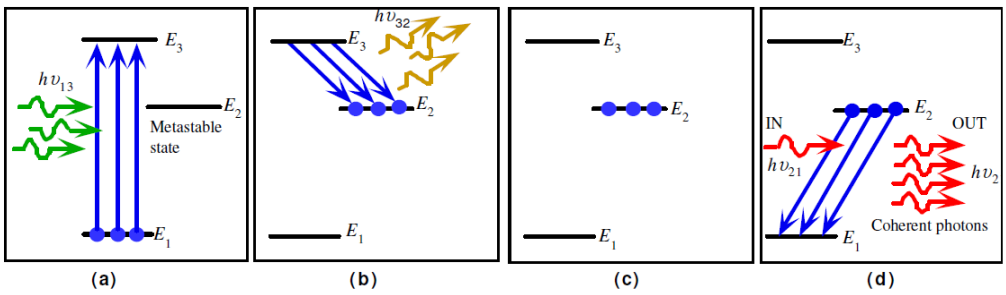

Figure 3.2. The principle of laser operation for a three-level system. (a) Optical pumping of electrons from level E_1 to E_3. (b) Fast electrons decay from E_3 to E_2 by spontaneous emission or radiationless decay. (c) Population accumulation in metastable level E_2. (d) Stimulated emission of photons generated by decay from level E_2 to level E_1.

an emission of photon from another electron on level E_2 and so on. The results are an avalanche effect with all the emitted photons in phases, so that the output light is ***coherent***.

At the end of the avalanche process, all the electrons decayed from E_2 to E_1, can be pumped again to repeat the stimulated emission cycle again. The emission from E_2 to E_1 is called lasing emission. The system described fro photon amplification is a ***LASER***, an acronym for ***Light Amplification by Stimulated Emission Process of Radiation.***

An example of a three-level laser system is ruby laser, the first type of laser to be discovered by Theodore Maiman in 1960 [3], in which the three energy levels are those of Cr^{3+} ion in the Al_2O_3 crystal (sapphire).

Because at least half the population of electrons must be excited from the lowest state E_1 to obtain a population inversion, the laser medium must be very strongly pumped. This makes three-level lasers rather inefficient.

A more efficient laser system is based on four-level energy levels, like the one reported in figure 3.3. In this case the material is pumped from level E_1 to level E_4, which is a fast decaying level, from which the electrons decay rapidly to level E_3, which is a metastable level. The stimulated emission takes place from level E_3 to level E_2. Level E_3 is a metastable state, where electrons accumulate, causing a population inversion between E_3 and E_2. This latter is a fast decaying level, which ensures that it rapidly gets empty and thus always supports the population inversion condition. Ideally, no appreciable population density in the lower laser level can occur even during laser

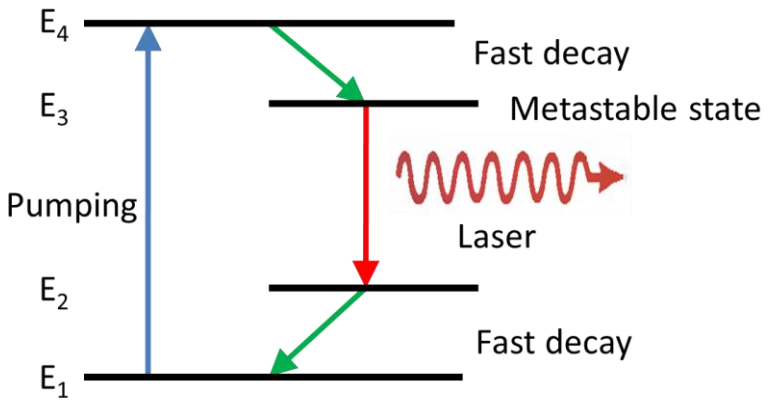

Figure 3.3. Four-levels laser system.

operation, making the four-level lasers quite efficient.

The most popular four-level solid-state gain medium is Nd^{3+}:YAG, in which the four energy levels are those of Nd^{3+} ion in the $Y_3Al_5O_{12}$ crystal (yttrium aluminum garnet).

3.1.3 Typical laser system

A typical laser system is shown in Figure 3.4. It consists of three basic parts:

- an *active medium* with a suitable set of energy levels to support laser action;
- a *source of pumping* energy in order to establish a population inversion;
- an *optical cavity* or *resonator* to introduce optical feedback and thus maintain the gain of the system overcoming all losses.

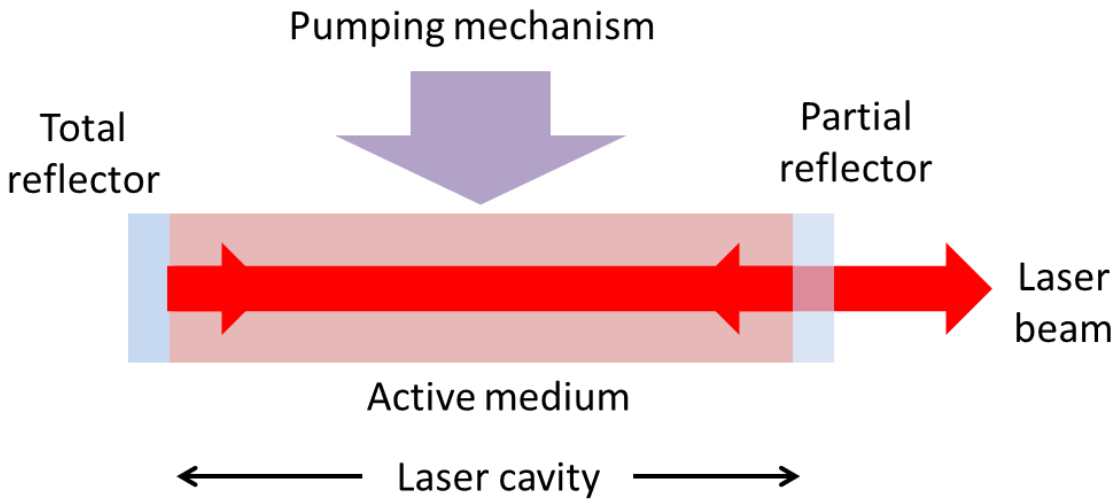

Figure 3.4. Typical laser system.

The active medium is a material (crystal, solid, liquid, semiconductor or gas medium) with properties that allow it to amplify light by stimulated emission. Light of a specific wavelength that passes through the gain medium is amplified (increases in power). The material should be of controlled purity, size and shape and should have the suitable energy levels to support population inversion. Specifically, it must have a metastable state to support stimulated emission. Most lasers are based on 3 or 4 level energy level systems, depending on the lasing medium.

As the gain medium adds energy to the amplified light, it must itself receive some energy through a process called pumping. There are various types of excitation or pumping mechanisms available, the most commonly used are optical, electrical, thermal or chemical techniques, which depends on the type of the laser gain medium employed. For example, solid state lasers usually employ optical pumping from high energy xenon flash lamps (e.g., ruby, Nd:YAG) or from a second pump laser or laser diode array. Gas lasers use an AC or DC electrical discharge through the gas medium, or external RF excitation, electron beam bombardment, or a chemical reaction. Diode laser are usually pumped by DC electrical current.

Optical resonator plays a very important role in the generation of laser light. Population inversion, in fact, is not sufficient for producing a laser action. As there are losses of the emitted photons within the material itself (due to absorption and scattering) in addition to spontaneous emission, an optical cavity or resonator are required to overcome these losses and generate gain in the active medium. Moreover the cavity confines the laser medium and the pumping mechanism in a way that promote stimulated emission rather than spontaneous emission.

The most common type of laser cavity that contains the gain medium consists of a high reflectivity mirror on one end and a partially reflective mirror, *output coupler*, on the other. Light bounces back and forth between the mirrors, passing through the gain medium and being amplified each time. Any photons which are either not of the correct frequency or do not travel along the optical axis are lost.

The output coupler transmits a fraction of the light circulating in the resonator cavity into an output beam. If the output coupler operates in a steady-state mode, i.e. constant energy output, the laser is called ***continuous wave*** (CW). If the output coupler is designed to abruptly change from near 0% transmission to 100%, all or part of the energy circulating in the resonator exits into a single pulse and the laser is called ***pulsed***.

Most practical lasers contain additional elements that affect properties of the emitted light such as the polarization, the wavelength, and the shape of the beam.

3.1.4 Laser oscillation conditions

Two conditions must be satisfied for laser oscillation to occur:

- the amplifier gain must be greater than the loss in the feedback system;
- the total phase shift in a single round trip must be a multiple of 2π.

Considering an optical cavity as the one reported in figure 3.4, laser threshold is reached when the optical gain of the laser medium is exactly balanced by the sum of all the losses experienced by light in one round trip of the laser's optical cavity.

The cavity losses are due to absorption and scattering losses in the active medium, spontaneous emission losses, mirrors and other optical components and laser light losses through the output coupler. This latter is essential for extracting the laser light from the cavity.

Let us consider a laser media of length L, reflectivity of output coupler R_2 and reflectivity of total reflector $R_1 = 1$. Assume an EM wave with an initial power P_i that enters the cavity. As the wave propagates, its power increases with $exp(gL)$ and, at the same time, decreases with $exp(-\gamma L)$, where γ is the loss coefficient of the medium, due to the loss phenomena. The power P_f of the EM radiation after one round trip of path length 2L is given by:

$$P_f = P_i R_1 R_2 \exp[g(2L) - \gamma(2L)] \tag{3.14}$$

For a steady state oscillations it must be:

$$P_f > P_i \tag{3.15}$$

The value of the gain that makes $P_f = P_i$ is called ***threshold gain*** g_{th} and it is expressed by:

$$g_{th} = \gamma + \frac{1}{2L} ln\left(\frac{1}{R_1 R_2}\right) \tag{3.16}$$

This is the threshold gain condition below which no laser oscillations can be sustained.

All the previous consideration on threshold gain considers only the intensity of the radiation inside the cavity, but additional conditions on the radiation phase are necessary in order to have a laser oscillation. To be more specific, the total phase shift in a single round trip must be a multiple of 2π to ensure constructive interference

instead of desctructive one. This means that only the waves with nodes at both ends are allowed, and so the cavity length must be an integral multiple of the half wavelengths.The result is the condition of resonance:

$$2nL = N\lambda \tag{3.17}$$

where *n* is the refractive index of the active medium, *N* is an integer, *nL* represents the theorethical path and λ is the wavelength.

The allowed mode of the cavity are called ***longitudinal mode.***

The cavity length and the refractive index of the laser medium determine the frequencies that are allowed inside the cavity.

3.1.5 Properties of laser light

Laser light presents certain unique properties compared to ordinary sources of light, specifically, monochromaticity, coherency, directionality and brightness. These properties are briefly discussed in the following.

Monochromaticity

The laser light is generated from an atomic transition with a single precise wavelength, thus has a single spectral colour and is almost the purest monochromatic light available.

Actually, laser light is not exactly monochromatic: various broadening factors such as Doppler effect of moving atoms and molecules cause a finite line width. The fact that in the laser cavity laser oscillation is allowed only at the resonant frequencies of the cavity leads to a further narrowing of the laser line width.

The degree of monochromaticity of laser light can be quantitatively described in terms of wavelength bandwidth or frequency bandwidth. Narrower is the line width, higher is the degree of the monochromaticity of the laser. This depends on the type of laser and special techniques can be used to improve monochromaticity. For example single-frequency solid-state bulk and fibre lasers can achieve linewidths of a few KHz, while for monolithic semiconductor lasers linewidth are typically in the MHz range. Much smaller linewidths, sometimes even below 1 Hz, can be reached by stabilization of lasers [4].

The laser linewidth could be also expresses in wavelength units; for example, a laser with emission wavelength of 590 nm and a frequency linewidth ~ 350 MHz has an equivalent wavelength linewidth ~ 0.0004 nm [5].

Lasers with very narrow linewidth and thus a high degree of monochromaticity are required as light sources for various applications, such as fibre-optic sensors, spectroscopy (e.g. LIDAR), in coherent optical fibre communications, and for test and measurement purposes.

Coherence

Coherence is one of the most important concepts in optics and is strongly related to the ability of light to exhibit interference effects. This unique property of laser light arises from the stimulated emission process from which this light is generated. All the emitted photons have a definite phase relation to each other and thus generate coherent output. Ordinary light is not coherent because it comes from independent atoms which emit on time scales of about 10^{-8} seconds without any phase relationship with each other.

There are two types of coherence: spatial and temporal.

Spatial coherence means a strong correlation (fixed phase relationship) between the electric fields at different locations across the beam profile. Let us consider two points P_1 and P_2 on a wave front, at time t= 0, with an electrical field $E_1(t)$ and $E_2(t)$ respectively. There will be a certain phase difference between these two points and if it remains same for every $t > 0$ and for any two points anywhere on the wave front, then we say that the EM wave has perfect spatial coherence.

Temporal coherence means a strong correlation between the electric fields at one location but different times. Let us consider a single point on the wave front of the EM wave at a time $t = 0$ and $t + dt$, there will be a certain phase difference between these two instant. If this phase difference remains the same for any value of dt, then we say that the EM wave has perfect temporal coherence.

It may be underlined that these two types of coherence are independent of each other, thus an EM wave can have perfect spatial coherence although a partial temporal coherence and vice versa.

Some applications need light with very high spatial and temporal coherence, for example for interferometry, holography and some types of optical sensors (e.g. fibre-optic sensors).

Directionality

The light from a typical laser emerges in an extremely thin beam with very little divergence, hence it is *collimated*. The high degree of collimation arises from the mechanism of generation of laser beam in a cavity. Laser light travels back and forth in the cavity for many times in order to gain intensity by the stimulated emission. Only photons traveling along the optic axis can be sustained, while the light slightest bit off axis, it will be lost from the beam.

The directionality of a laser beam is expressed in terms of full angle beam divergence, which is twice the angle that the outer edge of the beam makes with the centre of the beam. Usually it is expressed in radians, where 2π is equal to 360°.

The divergence displays how rapidly the beam spreads when it is emitted from the laser. For example, typical divergence of 1 mrad means that the laser beam increases in size of about 1mm for every meter of beam travel.

The highly collimated nature of the laser beam contributes both to its danger and to its usefulness. The highly parallel beams can focus to a small dot on the retina of the eye, causing almost an instant damage. On the other hand, this capacity for sharp focusing contributes to several application of laser light like cutting tool in industrial field or sharp scalpel in medical sector.

Brightness

The property of brightness is a result of the directionality and the coherence of laser light. In the context of laser technology, it is generally considered as being equivalent to the ***radiance***, which is the total power divided by the product of the mode area in the focus and the solid angle in the far-field; the units are then usually $W\ sr^{-1}\ m^{-2}$.

Brightness is then a property that is not only dealing with the total power delivered by a laser source, but also its diameter, and so concerns how the power is concentrated. For example the radiance of a mW helium neon laser is $1.6 \times 10^9\ Wsr^{-1}m^2$, far greater than the radiance of the sun, that is $10^6\ Wsr^{-1}m^2$ [6].

Brightness is a unique advantage for laser light for many laser applications in various areas, such as material processing, military technologies, medical treatments, etc.

3.2 Rare earth doped solid-state laser

A solid-state laser is a laser with a gain medium that is a solid, such as crystalline or glass material, doped with RE or transition metal ions, that can be made in the form of bulk lasers, fibre lasers, or other types of waveguide lasers. Semiconductor based lasers are also solid-state devices, but are generally considered as a separate class of lasers.

The host material must have good optical, mechanical, and thermal properties to withstand the severe operating conditions of practical lasers. Other important properties include hardness, chemical inertness, absence of internal strain and refractive index variations, resistance to radiation-induced colour centres and ease of fabrication [7].

For crystalline host, several interactions between the host crystal and the dopant ion restrict the number of useful material combinations. In particular the size and valence of the dopant ion should match that of the host ion to replace. The most common crystal hosts are: sapphire, vanadates, fluorides and synthetic garnets like yttrium aluminum garnet (YAG), gadolinium gallium garnet (GGG) and gadolinium scandium aluminum garnet (GSGG).

As already discussed in chapter 1, glass is an important class of host material for solid-state laser, especially doped with RE ions. Glass is easy to manufacture, versatile and less expensive than crystal. It allows a homogenous distribution or RE ions, and these ions in glass shows a large inhomogenous broadening of the absorption and emission cross section, due to the lack of a unique and well-defined crystalline field surrounding the individual active ions. Moreover, glass possesses a particular viscosity-temperature relationship that allows for fibre drawing (see section 1.1.2). However glass has a much lower thermal conductivity than most crystalline hosts and this causes, for laser rods, large thermally induced birefringence and optical distortion when they are operated at high average powers. Besides a low thermal conductivity causes a lower thermal shock resistance than crystals.

In the following the discussion will be limited to RE doped solid state lasers based on glass material, and specifically phosphate glass.

In order to obtain an active material for solid-state laser, host material must be doped with an active ion, which must have sharp fluorescent line, broad absorption bands and high quantum efficiency for the wavelength of interest. These characteristics are generally shown by solids that incorporate a small amount of active ions, in which the optical transitions can occur between states of inner incomplete electron shells. RE ions have been the most extensively used active ions, because exhibit a wealth of sharp fluorescent transitions representing almost every region of the visible and near-infrared portions of the EM spectrum. Their peculiar optical properties result from their particular atomic configuration, which will be briefly reviewed in the following paragraph.

3.2.1 Rare earth

The rare earths atoms are divided into two groups: the ***lanthanides*** that begin with cerium (Ce, $Z = 58$) and end with lutetium (Lu, $Z = 71$) and the ***actinides*** from thorium (Th, $Z = 90$) to lawrencium (Lr, $Z = 103$). Despite their name, RE elements (with the exception of the radioactive promethium) are relatively plentiful in the Earth's crust, with Ce being present at a level of 46 ppm [8].

Only the lanthanides are considered here, because they are of greater importance in lasers and amplifiers; many actinides, in fact, have no isotopes stable enough to be used in such devices, only promethium (Pm) has a short half-life (< 20 year) [9].

Let us consider a classic description of atom as an inner nucleus surrounded by shells of electrons, which are gradually filled as one moves along the periodic table. In general, the radius of each shell is larger than the previous one, but at the atomic number $Z = 57$, an abrupt contraction takes place. The 5*s* and 5*p* shells ($5s^2 5p^6$) are full and so electrons are progressively inserted in a 4*f* shell. This latter instead of having a larger radius than the 5*s* and 5*p* shells, actually contracts and becomes shielded from the environment by these shells. This effect is called ***lanthanide contraction*** and is the reason of RE peculiar optical and electronic properties.

The radius of 4*f* shell slowly decreases from the beginning to the end of the lanthanide series with an overall contraction about 10% [10].

The most common and stable form of RE elements in condensed matter is the ionic form, in particular the trivalent (3^+) state. When a trivalent ion is formed, the RE atom

gives up its outermost electrons and the electronic configuration remains that of the xenon structure plus a certain number (1–14) of 4*f* electrons.

The 4*f* energy level of a RE ion is actually composed by a number of states, which arises from various atomic interactions between electrons. When the ion is placed in a host material, further splitting of energy levels occurs due to the influence of the environment. This effect is normally treated as a perturbation on the free-ion levels, since it is small compared to the atomic interactions among the 4*f* electrons. This crystal field splitting is called ***Stark splitting*** and the resulting states are called *Stark components*.

The Hamiltonian operator *H* for the 4*f* electron could be decomposed as:

$$H = H_{H-like} + H_{coul} + H_{SO} + H_{CF} \tag{3.18}$$

the first term is the sums over all *n* electrons of the individual hydrogen-like kinetic and potential energy; H_{coul} represents the mutual Coloumb repulsion between electrons; H_{SO} describes the electron-spin and orbital-angular momentum interactions and the last term, H_{CF}, represents the electron perturbations caused by the surrounding crystal field [11].

There are several schemes for describing the states of a many-electron system. For RE is habitual to use *Russel-Saunders*, or *LS*, coupled state. The levels are labelled as $^{2S+1}\mathbf{L_J}$,where **L** and **S** are the vector sums of the orbital and spin quantum numbers for all the 4*f* electrons of the ion and **J** is the total angular momentum obtained by vectorially adding **L** and **S**. Total orbital angular momentum is specified by the letters S, P, D,F, G, H, I, K, . . . to represent L = 0, 1, 2, 3, 4, 5, 6, 7, . . . , respectively.

Figure 3.5 represents the splitting of the $4f^N$ level under the effect of the atomic and crystal field Hamiltonian. First the atomic forces split the original configuration of one electrons orbital into $^{2S+1}\mathbf{L_J}$ levels, and then the roughly 100 times weak electrostatic crystal field Hamiltonian splits each free-ion atomic level into a collection of Stark levels, generally separated by 10 – 100 cm^{-1}.

The fluorescence spectra of RE ions are a consequence of electronic transitions between levels of the partially filled 4*f* shells that are well bounded by the filled 5*s* and 5*p* outer shells. As a result, emission lines are relatively narrow and the energy level structure varies only slightly from one host to another.

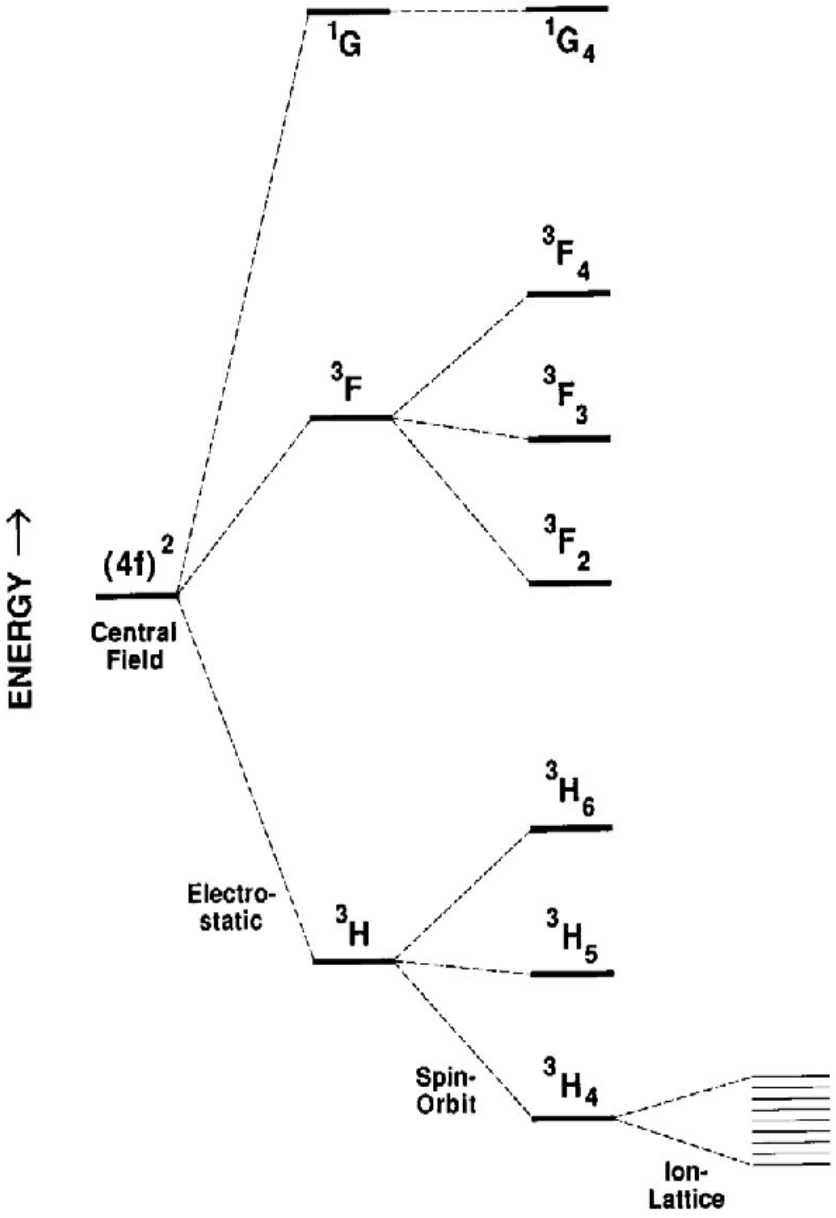

Figure 3.5. Schematic representation of the splitting of $4f^2$ level under the effect of electron–electron and electron–host interactions [9].

However, from the above considerations arises that the transitions between two RE levels are actually transitions between several lines, each of them having different population with different intensities. The result is an emission band, whose shape and dimension are a function of the host glass. Intensity and shape of the band are related to

the transition probabilities among *J*-states: if probabilities were equal, the band would be square shaped.

3.2.2 Radiative transitions

As discussed in the previous paragraph, the $4f^N$ electron state configuration of the RE ions is not sensitive to the environment, on the contrary the transition probability between these electron states is sensitive to the surrounding ions, both radiatively and nonradiatively.

If we assume the host medium as a collection of charged particles (electrons and ion cores), the elastic displacement of the electronic charge distribution to the nucleus causes a collection of induced electric-dipole moments. Classically, a light wave consists of electric and magnetic fields which vary sinusoidally at optical frequency. Since a light wave interaction with a material induces a charge displacement, its effect can be expressed in terms of the field induced electric-dipole moment [12].

The likelihood of transitions between electronic levels in an atom is governed by certain selection rules. For example, dipole transitions can occur only between energy levels with the angular momentum parameter *L* differing by one. Therefore, dipole transitions between energy levels with same parity are forbidden. However, for ions in a glass, internal electric and magnetic fields can break certain symmetries, so that originally dipole-forbidden transitions become possible by mixing of states with different parity. Such processes, however, exhibit a small probability to occur, i.e. small oscillator strength. The resulting transitions are called *weakly allowed transitions*. Whereas typical upper-state lifetimes are of the order of a few nanoseconds for allowed transitions for spontaneous emission, weakly allowed transitions for ions in glasses are typically between microseconds and milliseconds. Such long-lived levels are called ***metastable states***.

Optical transitions in RE ions have been found to be predominantly electric-dipole in nature, and thus, since no change of parity is involved, principally forbidden by Laporte's rule. However, when RE ions are embedded in solids, quantum mixing of higher lying states of opposite parity into the $4f$ configuration, introduces a degree of electric dipole strength into the $f \rightarrow f$ transitions.

Magnetic dipole and electric quadrupole transitions are allowed by the selection rules but their contributions to radiative decay are generally small or negligible [12].

The electric-dipole transition probabilities can be calculated, assuming certain approximations, using the Judd - Ofelt theory [13,14]. In this theory the line strength of an $f \rightarrow f$ transition in a RE ion is expressed in terms of a sum of the products of three intensity parameters Ω_λ and squared matrix elements between the initial *J* state and final *J'* state.

It has been shown that the matrix elements of the majority of RE ions are almost insensitive to the materials and have been tabulated by a number of authors [15,16]. The three intensity parameters Ω_2, Ω_4, Ω_6 on the other hand, contain the host dependence and are empirically determined for a given combination of dopant and host. Judd–Ofelt analysis is accurate to about 10–15% and is particularly valuable for obtaining strengths of transitions for which direct measurements are difficult or impossible.

3.2.3 Nonradiative relaxations

In addition to the interaction with EM radiation through emission and absorption of photons, RE ions in glass can interact with vibration of host material through exchange of *phonons*.

If the energy gap ΔE between the electronic levels is of the order of one or two phonons, for example the Stark components of a multiplet, the transitions will occur rapidly. This leads to thermal occupation of levels above the ground state or metastable excited state if the separations are on the order of the thermal energy (a few *kT* or less).

When the energy gaps ΔE are much larger than *kT*, like between *J* multiplets, the process proceeds predominantly in the downward direction, with the emission of several lattice phonons in order to bridge the energy gap (see Fig. 3.6). For the energy conservation it is required that:

$$p\hbar\omega_{ph} = \Delta E \tag{3.19}$$

where *p* is the number of phonons of energy $\hbar\omega_{ph}$.

The nonradiative decay rate W_{nr} is inversely proportional to the exponential of the energy gap separating the two levels:

$$W_{nr} = W_0 exp[-\alpha \Delta E] \tag{3.20}$$

where W_0 is the transition probability extrapolated to zero energy gap and α is correlated to the phonon vibration ω_{ph} by:

$$\alpha = \left(\frac{1}{\hbar\omega_{ph}}\right)\left\{ln\left[\frac{p}{g(n+1)}\right] - 1\right\} \tag{3.21}$$

where g is the electron phonon coupling constant [17,18] .

From the equations 3.20 and 3.21 it follows that the nonradiative decay rate W_{nr} has not only an exponential dependence on ΔE but also on the phonon vibration ω_{ph}.

In practice W_0, α and p (or $\hbar\omega_{ph}$) are considered as empirical parameters that are host-dependent, but insensitive to the RE ion and energy levels involved. Their values were measured for several glasses and crystalline materials [19].

Table 3.1. lists the maximum phonon energy of various glasses that corresponds to the stretching vibrations of the glass network formers. It can be observed that oxides glasses have larger nonradiative rates because their strong covalent bonds result in higher phonon frequencies, while the weaker ionic bonds of halide glasses lead to a much lower W_{nr}.

Table 3.1. Maximum phonon energy of various glasses [19].

Glass type	Phonon energy $\hbar\omega_{ph}$ (cm^{-1})
Borate	1400
Silicate	1100
Phosphate	1200
Germanate	900
Tellurite	700
Fluorozirconate	500
Chalcogenide	350

Another type of nonradiative decay process involves ion-ion interactions primarily leading to ***concentration quenching***, that is the reduction of fluorescence emission as the concentration of the active ions is increased. This effect has important implications for the performance of luminescent devices because it results in a loss of excitation.

When the concentration of RE ions in solids is increased, the ions become closely spaced and consequently they can interact with each other. Figure 3.6 reports two different relaxation processes: *cross relaxation* and *cooperative up-conversion.*

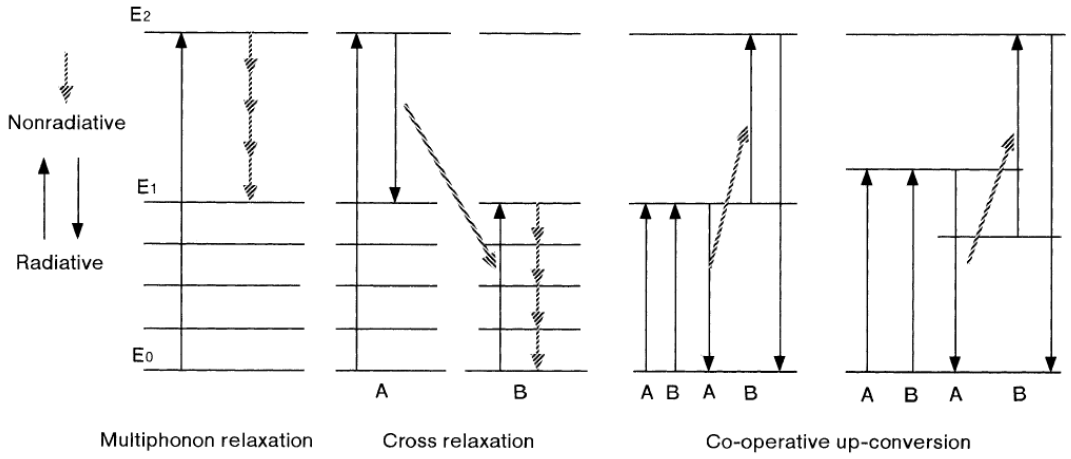

Figure 3.6. Nonradiative relaxation processes of RE ions in solids [12].

Cross relaxation may take place between the same RE ions, which have two pairs of energy levels separated by the same amount. Ion *A* is in the excited state, ion *B* is in its ground-state. Ion *A* gives half its energy to an ion *B*, so that both ions end up in the intermediate energy level, from which they relax rapidly to the ground state via non-radiative relaxation. The major cause of concentration quenching for Nd^{3+}-doped glasses is believed to be due to this process [19].

Co-operative up-conversion is a process in which two neighbouring ions, *A* and *B*, are initially in the excited state. Then ion *A* gives its energy to ion *B*, thus promoting it to a higher energy level while the *A* relaxes to the ground state. From this higher energy level, ion *B* relaxes quickly to the ground state via phonon relaxation. Co-operative up-conversion is believed to be a dominating factor in the concentration quenching of Er^{3+} ion in glass [20].

When energy transfer takes place between two different species of ions, the excited ion, which loses its energy, is called the ***donor*** *(or* ***sensitizer****)*, while the one that receives the excitation is called the ***acceptor*** *(or* ***activator****)*. This transfer mechanism is commonly exploited for sensitizing materials using large donor concentrations (for example Yb^{3+}) to absorb the optical excitation and transfer it to emitting ion (for example Er^{3+}) when the latter has a weak absorption band or not matched with the pumping wavelength.

Concentration quenching usually manifests itself as a shortening of the excited-state lifetime. This effect could be described by the empirical formula [9]:

$$\tau(N) = \frac{\tau_0}{1+\left(\frac{N}{N_0}\right)^2} \tag{3.22}$$

where τ is the measured lifetime at a given RE ion concentration N, τ_0 is the *lifetime in the limit of "zero" concentration*, i.e. the radiative lifetime and N_0 is the *quenching concentration*.

This analysis assumes that the RE ions are uniformly dispersed throughout the glass and do not cluster. If the concentration is kept in the limit of few percent, this is usually true for multicomponent glasses.

Among glasses for which data are available, phosphates are the most resistant to quenching, as already mentioned in chapter 1, and thus they allow the realization of highly doped active material. A phosphate glass doped with 8 wt% of Nd^{3+} ions has been reported [21], which is probably attributed to the large Nd-Nd distance resulting from the chain-form structure, and to the difficulty of Nd-Nd interaction [22].

Another nonradiative transition process, which is deleterious for fluorescence emission, is the energy transfer to the OH^- ions, which are extremely effective at quenching excited RE ions [23].

When OH^- groups are present in a glass, the nonradiative rates are increased because of coupling between the RE states and the high energy (3200 cm^{-1}) vibrations of OH^- [24]. Its contribution to nonradiative decay is considered to be larger than that of the multiphonon process because of the higher vibration energy.

Phosphate glasses can retain significant amounts of OH^- and consequently the lifetimes of the RE states are shortened. To minimize this deleterious effect the water content in these glasses must be kept as low as possible.

3.2.4 Neodymium

Neodymium (Nd) is a RE element with atomic number 60 and electronic configuration [Xe] $4f^4\,6s^2$. When it is incorporated in a glass it loses three electrons and forms the trivalent state Nd^{3+} with the ground electronic configuration $4f^3$. Energy levels for Nd^{3+} (see Fig. 3.7) originate from the splitting of the $4f^3$ configuration under the effect of the coulombic (H_{coul}), spin-orbit coupling (H_{SO}) and crystal field (H_{CF}) interactions (see equation 3.18).

In general, for the magnitude of the various interactions in Nd^{3+} in glass it can be written:

$$H_{H-like} \gg H_{coul} \geq H_{SO} > H_{CF} \tag{3.23}$$

As previously discussed (see section 3.2.1), the effect of crystal field (H_{CF}) is quite small compared to the other interactions, because of the shielding of 4*f* orbitals by the filled 5*s* and 5*p* outer shells. Therefore, the Nd^{3+} ion energy level configuration varies only slightly from one host to another. The magnitude of the crystal field splitting is of order 100 cm^{-1} (Fig. 3.7) and thus approximates kT at ambient temperatures (200 cm^{-1}). Moreover, due to the lack of symmetry in glass material, Nd^{3+} ions reside in sites having a slightly different crystal field interaction [25]. The result is that Stark splitting cannot be individually resolved; in Fig. 3.7 they are represented as broad and shaded bands.

The spin-orbit interaction is quite large for Nd and these causes that $^4I_{11/2}$ state remains virtually unpopulated at ambient temperatures. This effect together with the high energy gap between the $^4F_{3/2}$ state and the terminal ^4I_j states (~5500 cm^{-1}), is the reason why Nd-doped gain media exhibit pure four-level behaviour.

The states above the $^4F_{3/2}$ level are split by energies of order 1000 cm^{-1}, that is, in case of phosphate glass matrix, similar to the phonon energies of the glass (~1200 cm^{-1}). Therefore electrons excited to these levels undergo radiationless decay down to the

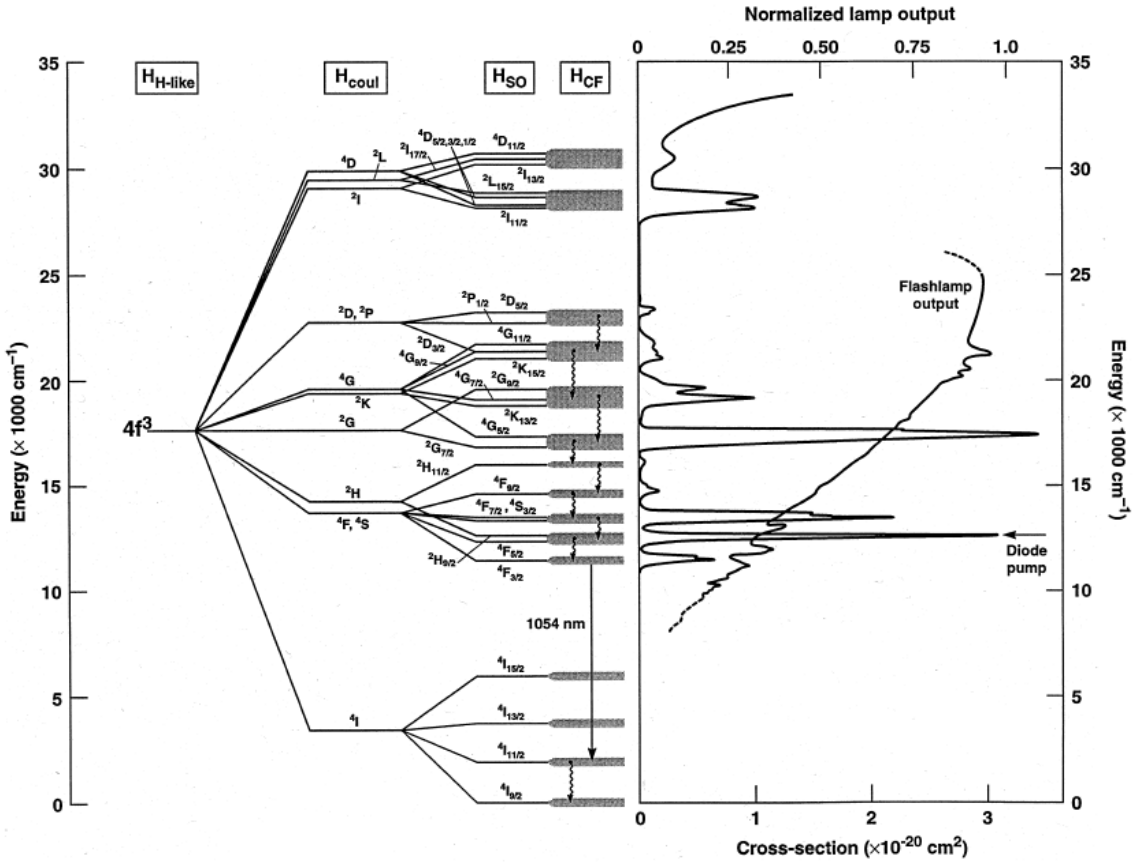

Figure 3.7. On the left: energy levels for Nd^{3+} originating from the splitting of the $4f^3$ configuration under the effect of the coulombic (H_{coul}), spin-orbit coupling (H_{SO}) and crystal field (H_{CF}) interactions. The laser transition of interest (1053 nm) is from the metastable $^4F_{3/2}$ state to the $^4I_{11/2}$ terminal level. The wavy lines denote rapid non-radiative (multi-phonon) transitions. On the right: typical Nd-absorption cross-section in metaphosphate glass host. Relative output intensity for a xenon flashlamp and laser diode pump source are also shown. The energies reported are relative to the $^4I_{9/2}$ ground state [11].

$^4F_{3/2}$ state where they accumulate. In fact the high energy gap between the $^4F_{3/2}$ state and the lower-lying ^4I_j manifold prevents multiphonon decay from this level and, on the contrary, favourites radiative decay [11].

Although the radiative decay can occur to all the lower lying ^4I_J levels, the strongest transition is the one to the $^4I_{11/2}$ level that leads to the emission of light near 1053 nm in most phosphate glasses. From the level $^4I_{11/2}$ electrons quickly decay via multi-phonon relaxation to the ground state thus preventing a build-up of population in the terminal level. The reported lifetimes of this level, for commercial phosphate laser glasses (LG-750, APG-1 and APG-2), are in the range 250 to 450 ps [26-28].

In figure 3.7 the absorption bands of Nd^{3+} ion is also reported. Thanks to its several absorption bands in the visible and near IR, Nd can be pumped by flashlamps, that are the oldest and most common pumping solution for Nd^{3+}-doped glass lasers. In the figure 3.7 the typical spectral overlap of the output spectrum from a xenon flashlamp with the Nd^{3+} absorption bands is shown.

More recently, with the availability of laser diode at the requested wavelength, a more efficient and compact pumping scheme has been achieved through the use of AlGaAs pump diode lasers operating around 808 nm that excite the transition $^4I_{9/2} \rightarrow {}^2H_{9/2} + {}^4F_{5/2}$ (see fig. 3.7). Despite the large number of closely spaced excited states, Nd^{3+} ion does not suffer more from excited state absorption (ESA). Although the $^4F_{3/2} \rightarrow {}^2D_{5/2}$ ESA transition occurs at close to 800 nm, it is extremely weak and does not significantly degrade 800 nm pumping [9].

As mentioned before, the radiative decay from $^4F_{3/2}$ can occur not only to $^4I_{11/2,}$ but also to the other ^4I_J levels as represented in figure 3.8. In order to achieve lasing on those emissions, lasing at the 1053 nm line needs to be suppressed by inserting an appropriate wavelength filter (usually consisting of one or more dichroic mirrors) into the cavity.

In meta-phosphate laser glass compositions, it was calculated by Judd-Ofelt analysis [13,14], that 50% of transitions terminate at the $^4I_{11/2}$ state, 40% at the $^4I_{9/2}$ state and 10% at $^4I_{13/2}$; typically less than 0.5% radiate to the $^4I_{15/2}$ state [11].

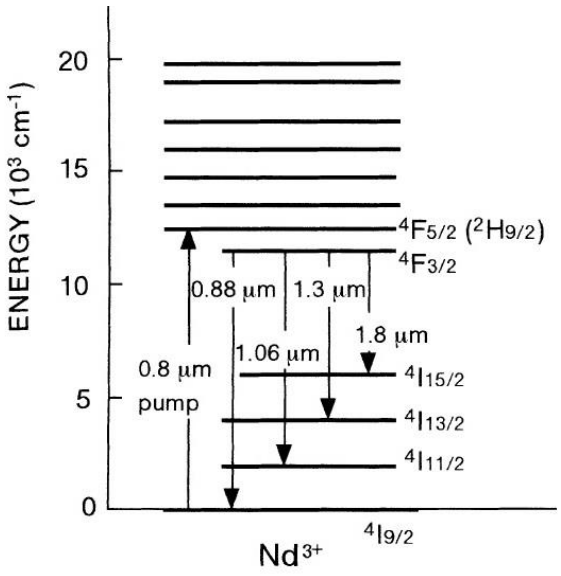

Figure 3.8. Possible lasing transitions from Nd^{3+}:$^4F_{3/2}$ to ^4I_J.

The $^4F_{3/2} \rightarrow {}^4I_{9/2}$ decay leads to an emission at ~900 nm. In this case the laser is a three-level, thus exhibiting a fairly high threshold pump power.

The $^4F_{3/2} \rightarrow {}^4I_{13/2}$ decay generates an emission at ~1300 nm, with real four-level laser behaviour. This emission

suffers ESA from metastable levels.

The ${}^4F_{3/2} \rightarrow {}^4I_{15/2}$ decay generates an emission at ~1800 nm.

Figure 3.9 reports Nd^{3+} ion emission cross section spectra for representative glass compositions, illustrating the variation in magnitude and shape.

The efficiency of the radiative transitions from the ${}^4F_{3/2}$ state can be reduced by non-radiative decay. The observable net effect is a reduction of the fluorescence lifetime of the energy level (see equation 3.12 and 3.13), that can be measured in a Nd-doped glass sample after excitation by a short-pulse pump source. Non-radiative losses can reduce the stored energy in the glass and thus affect the laser gain and overall system performance.

The effect is a sum of contributions from all non-radiative processes that can occur to Nd^{3+} ion ion in a glass (see section 3.2.3). They can be divided into intrinsic losses, that depend on the glass structure and doping level, (such as multi-phonon relaxation, Nd self-quenching, Auger up-conversion) and extrinsic losses due to impurities that enter during glass processing (hydroxyl groups, transition metal ions and RE ions). A summary of the different types of relaxation processes of Nd^{3+} in phosphate laser glasses is illustrated in figure 3.10.

Among intrinsic non-radiative losses, the study of Nd self-quenching in laser glasses has received perhaps the most attention, since for high power application Nd-doped glass has to be doped with a large amount of Nd^{3+} ions in order to maximize the pump light absorption and the stored energy density. The mechanisms involve energy transfer between two Nd^{3+} ions, one in the ${}^4F_{3/2}$ excited state and the other in the ${}^4I_{9/2}$ ground state (see figure 3.10). The exchange converts both to the ${}^4I_{15/2}$ level from which they non-radiatevely decay to the ground state. This loss mechanism usually dominates at high Nd concentration and it is characterized by $N_{0,}$ the quenching concentration (see equation 3.22). N_0 is defined as the concentration (ion/cm^3) that reduces the lifetime by one half. The higher the N_0 value, the less sensitive the laser glass is to Nd self-quenching. This parameter could be determined from emission lifetime measurements on a series of samples with different doping level.

The results of several studies [see references in 11] show that laser glass compositions more resistant to concentration quenching effects are those glasses that use alkali metal or earth alkali metal cations with the smallest electric field strengths.

(a)

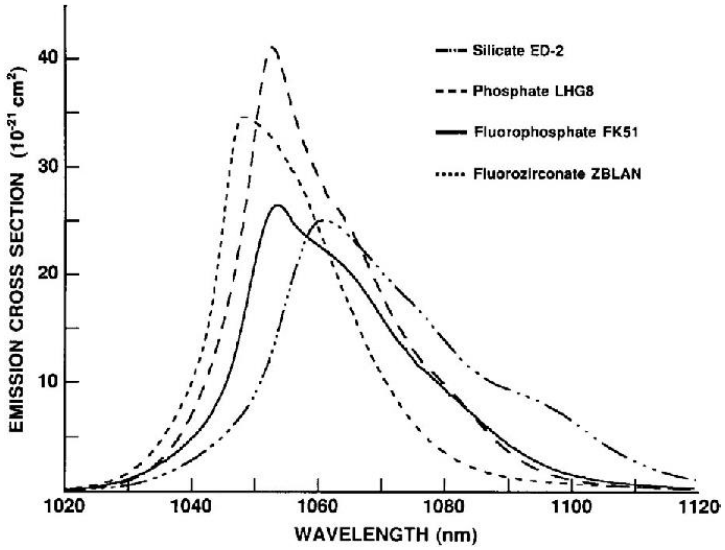

(b)

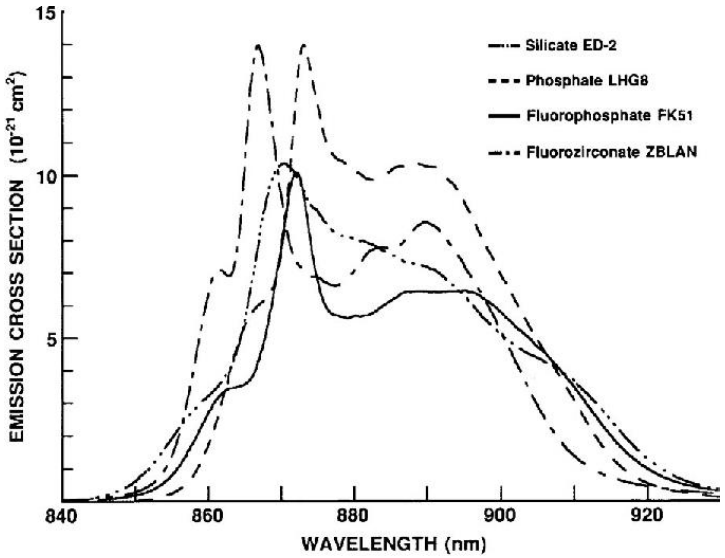

(c)

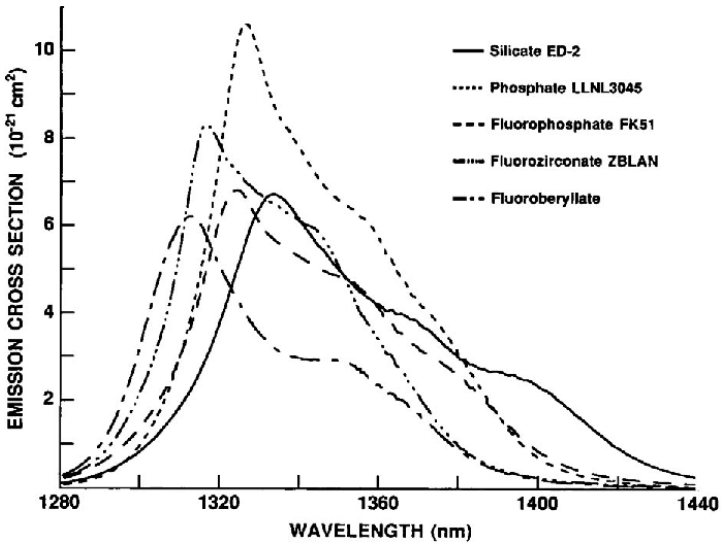

Figure 3.9. Nd^{3+} ion emission cross section spectra for representative glass compositions, illustrating the variation in magnitude and shape. (a)$^4F_{3/2} \rightarrow {}^4I_{11/2}$ (b) $^4F_{3/2} \rightarrow {}^4I_{9/2}$ (c) $^4F_{3/2} \rightarrow {}^4I_{13/2}$. Excitation at 800 nm. [9]

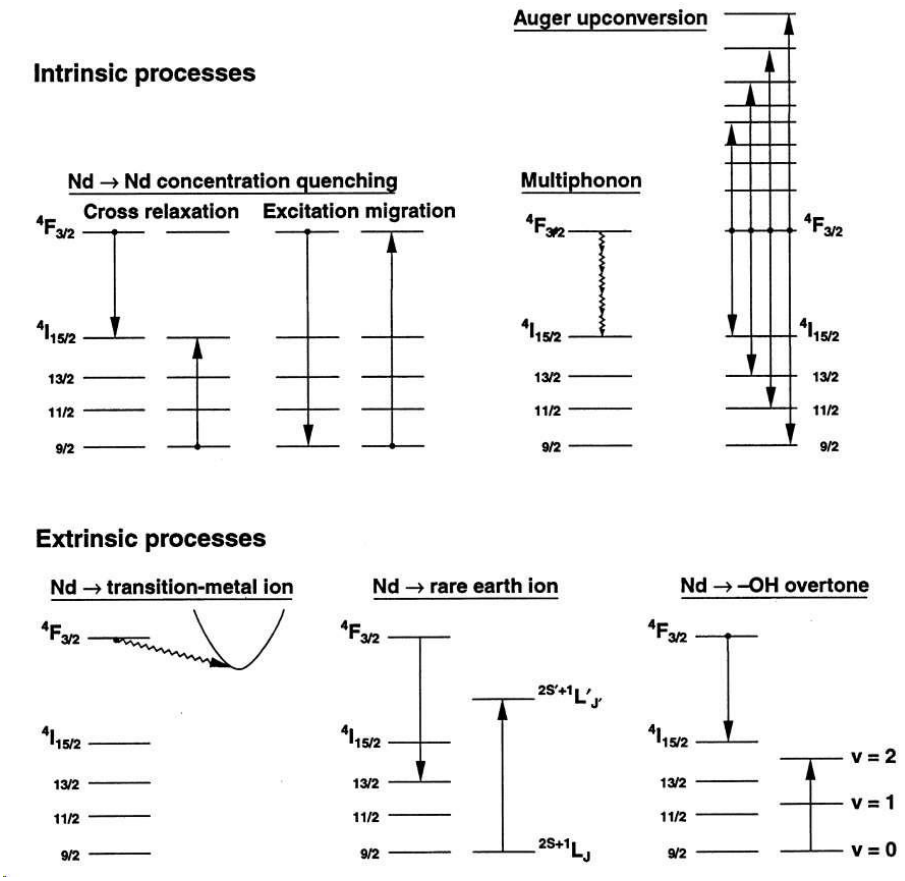

Figure 3.10. Non-radiative Nd^{3+} relaxation processes in phosphate laser glasses [11].

The data indicate that K^+ and Ba^{2+} should give the best results and indeed one or both of these two modifiers are used in commercial laser glass compositions.

Concerning extrinsic non-radiative losses, great attention has to be done to avoid contamination during glass processing in order to achieve optimum laser performance. However, it must be said, that in modern commercial phosphate laser glasses the problems associated with impurities have been largely eliminated by proper choice of raw materials and melting equipment.

On the other hand, water (i.e. OH^-) contamination can be a large problem because of the hygroscopic nature of most phosphate laser glasses. To achieve the maximum fluorescent lifetime, hydroxyl absorption should be kept lower than 2.0 cm^{-1} at 3000 cm^{-1}, corresponding to about 200 ppmw of OH [11]. Most laser glass manufactures can

meet this specification but it is often difficult for university researchers to prepare dry samples during small scale test melt.

The presence of OH^- ions affect in particular the emissions at 1300 nm ($^4F_{3/2} \rightarrow {}^4I_{13/2}$) and 900 nm ($^4F_{3/2} \rightarrow {}^4I_{9/2}$) that are directly affected by absorption from overtones of the water fundamental absorption located at 1383 nm and 950 nm.

3.3 Fibre laser

For solid state laser several geometries of the gain media have been developed such as rod, disc, slab and fibre. The oldest and most common geometry is the rod, with dimensions of few millimetres in diameter and several centimetres in length. However, conventional rod lasers suffer from thermo-optical problems leading to thermal lensing effects or induced birefringence, thus simple power scaling by maintaining a good beam quality is limited.

A promising alternative to bulk solid-state laser systems are fibre lasers, in which the gain medium is an optical fibre doped with RE ions (Nd^{3+}, Yb^{3+}, Er^{3+}, Tm^{3+}…).

Fibre lasers are not only one of the fastest growing photonic technologies, but also an industrial reality, thanks to their unmatched performance, especially in terms of beam management and quality [29,30].

3.3.1 The advantages of fibre laser

Optical fibre lasers have several key advantages over conventional bulk solid state laser:

- Outstanding heat-dissipation capability thanks to their high surface-to-volume ratio and the distribution of the thermal load over a considerably long length, resulting in excellent heat dissipation. Thermal distortion of the beam is thus negligible, and the beam quality depends primarily on the physical design of the fibre.
- Tight confinement of both pump and laser light, resulting in a low threshold and high optical conversion efficiency.
- Excellent beam quality, quite insensitive to thermal and mechanical perturbations. Single mode fibre laser exhibit a ***diffraction-limited Gaussian beam*** that is a beam that can be focused to the smallest spot possible for a given wavelength, i.e. the

beam quality is ideal. For a given optical power, a diffraction-limited beam has also the highest brightness. Often beam quality is quantified using a parameter, called M^2, which compares the divergence of a laser beam to that of a pure Gaussian single-mode beam with the same waist located at the same position. The value of M^2 for a single mode fibre laser is 1, while some high-power lasers (e.g. solid-state bulk lasers and semiconductor lasers such as diode bars) can have a very large M^2 of more than 100 or even well above 1000. Beam quality is a key point for all the applications in which narrow focusing of the beam is required, such as laser material processing, printing, marking, cutting and drilling. High beam quality allows also a simplification in the delivery optics.

- Simplified beam handling and beam delivery that enables to transport higher levels of power inside the laser, using higher brilliance to deliver more useful power at the workpiece.
- Possibility of pumping with low cost reliable diode lasers.
- Scalability to high power level through modularity. Commercial devices at kW level commonly employ more sophisticated architecture than a single stage laser resonator. They often use one or more high power amplifier stages that are seeded by a medium or even high power fibre oscillator (MOPA - Master Oscillator Power Amplifier configuration). Optical pumping is achieved using a large number of single emitter diode sources pigtailed with 100 µm fibres. These are then combined, using sophisticated fibre arrangements, to achieve high power in a fibre network before being launched into the RE doped fibre [32]. Another possibility is the so called *tandem pumping*, in which one or several fibre lasers pump another one [33].
- Possibility to realize the whole laser resonator only using fibre components, *all-fibre setup*, such as fibre Bragg gratings and fibre couplers. This configuration avoids the use of free-space optics, that can be critical in presence of vibrations or large temperature variations; in addition light in fibres is totally confined within the core-cladding structure and thus completely shielded from the environment. Using an *all-fibre setup,* a robust and compact system design is possible, thus enabling the usability of fibre lasers outside the laboratory.

- Large variety of temporal output properties that can be supported. Due to the very large spectral bandwidths achievable from RE ions in glass, fibre lasers can be built to operate from the CW regime down to pulse durations of just a few fs.
- High wall-plug efficiency up to 30% compared with typically less than 5% for conventional bulk solid-state lasers. Higher wall-plug efficiency means that air cooling rather than water cooling is often sufficient. Diode lasers can reach higher wall-plug efficiency (up to 60%) but they cannot always be used, because of their poor beam quality and their inability to generate intense pulses.

The drawback of fibre laser, as opposed to conventional diode-pumped solid-state laser systems, is that the significantly longer interaction length and the tight confinement of the laser radiation enforce disturbing nonlinear effects (such as self-phase modulation, Raman scattering and stimulated Brillouin scattering), which constitute the main restriction of RE-doped fibre laser systems. These effects basically limits the performance of RE-doped fibre systems before limitations due to thermo-optical effects or fracture of the fibre are reached [34, 35].

3.3.2 Optical resonator

The most common fibre laser resonator is the Fabry-Perot (Fig. 3.11a-c), formed by ordinary dielectric mirrors in close contact with the ends of the doped fibre (Fig. 3.11a). Pump light is launched from the left-hand side, through the dichroic mirror, into the doped fibre. Laser light is generated in the fibre through a stimulated emission process, and it is extracted on the right-hand side. A variation of this design is possible by depositing dielectric reflector directly on fibre ends, usually with some evaporation method.

The Fresnel reflection from a bare fibre end face is often sufficient for the output coupler of a fibre laser, especially in lasers based on a high gain transition (such as Nd^{3+}:${}^4F_{3/2} \rightarrow {}^4I_{11/2}$).

For commercial products, it is common to avoid the use of free space optics and all-fibre Fabry-Perot resonator designs are preferred. Figure 3.11b shows a resonator in which the optical feedback is provided by two Sagnac fibre loops, one at each end of the doped fibre. Each loop is made of a length of doped fibre closed by a coupler. They

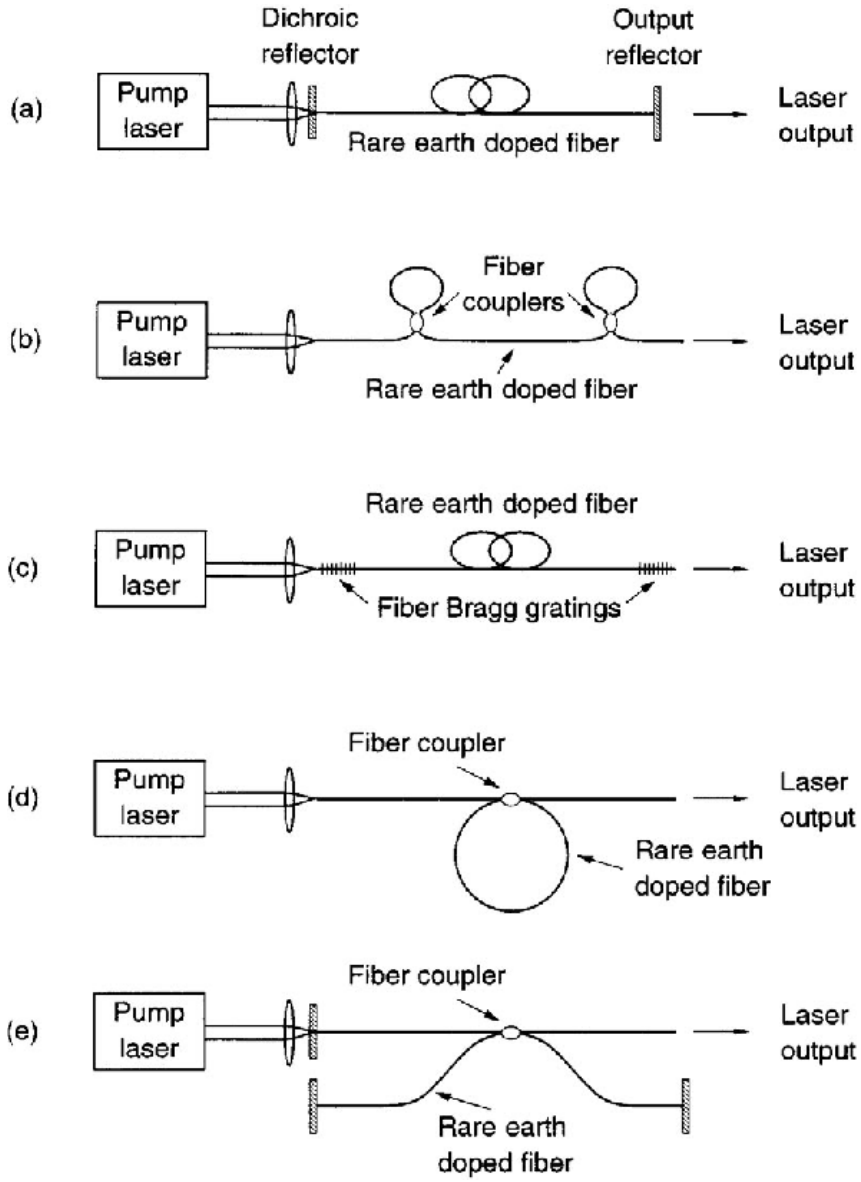

Figure 3.11. Setup of various fibre resonators: (a) Fabry–Perot with dielectric reflectors; (b) Fabry–Perot with all-fibre reflectors; (c) Fabry–Perot with fibre Bragg gratings; (d) ring; and (e) Fox–Smith [9].

have a typical insertion loss of less than 0.3 dB, so that the loss of this resonator can be quite low.

Another solution is provided by the use of fibre Bragg gratings (Fig. 3.11c), that can be either spliced to the fibre end or, if possible, directly written in the doped fibre, reducing the number of splice and consequently the loss.

A particular benefit of this design is the possibility to use as pump source a fibre pigtailed laser diode that can be spliced directly to the fibre laser, thus reducing pump coupling loss.

Alternative setup for fibre laser is the *all-fibre ring resonator* (Fig. 3.11d), which consists in a loop of doped fibre with a low loss fused fibre coupler. The displayed ring laser resonates in both directions and, therefore, has a bidirectional output. This means that its conversion efficiency is only half compared to the one of Fabry–Perot cavity. It is possible to overcome this limitation by introducing an optical isolator in the ring, which forces unidirectional operation. However, this element introduce also a small loss, thus unidirectional ring fibre lasers require higher threshold.

A less commonly used solution is the Fox-Smith resonator (Fig. 3.11e), which consists in a standard Fabry-Perot resonator coupled through a fibre coupler, to a third branch with a mirror at its end. The doped fibre is positioned in one of the arms and pumped through one of the reflectors [9].

3.3.3 Double cladding optical fibre

In a conventional fibre laser pumped with laser diode, where just the RE doped single mode core can guide light, the pump light is coupled into the fibre core. This requires the use of a single-mode pump laser diode, whose output power is currently limited to a few watts due to the damage threshold of the semiconductor materials used for their fabrication and imposes a major limitation on the maximum output power that can be obtained by a fibre laser. Moreover, only a fraction of pump power can be efficiently coupled into the fibre core, typically about 60% or less, because of astigmatism of the laser diode beam. Therefore, the output power of a single-clad fibre laser is restricted to a few watts.

This limitation can be overcome by the use of the double-clad (DC) fibre design, invented in 1988 by Snitzer [36] that has allowed in last decade a significant improvement in scaling fibre lasers to higher power levels.

DC fibres (see Fig. 3.12) consist in a single–mode core, doped with RE ions, surrounded by an inner cladding of lower refractive index, itself surrounded by an outer cladding of still lower index. In most cases the outer cladding is made of a polymer material rather than glass. Pump light is coupled in the inner cladding and

spatially overlaps the RE doped single mode core of the fibre and it is absorbed by the

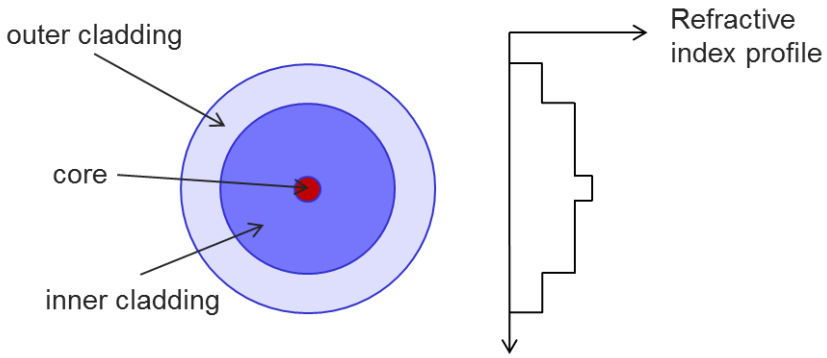

Figure 3.12. Basic design of double cladding optical fibre and its index profile.

dopant over the entire fibre length.

The benefit of this design is the fact that due to the larger area (10 ÷ 100 times larger than core area) and larger numerical aperture, the pump cladding supports many more modes than the core (see Fig. 3.13). This allows to use multimode high power laser diode, as optical pump source, with relatively poor beam quality and to obtain single mode laser radiation with excellent beam quality. So the DC fibre laser is an efficient and simple mean to convert low brightness pump light into high brightness laser radiation, this is why it is also called ***brightness converter***.

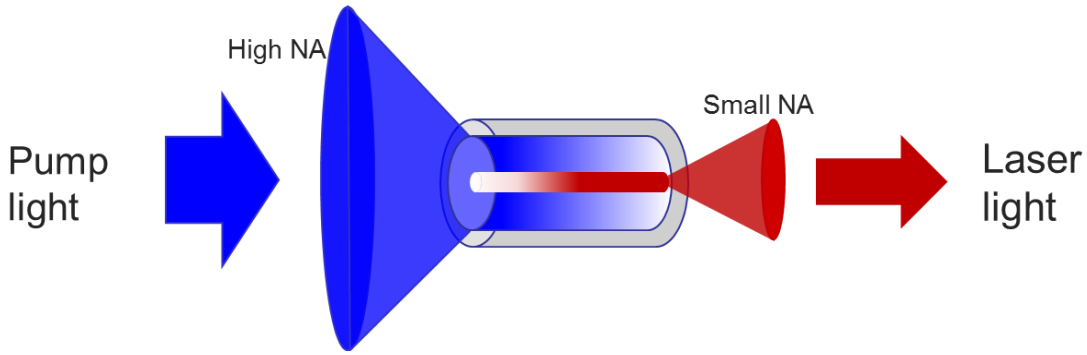

Figure 3.13. Principle of cladding pumping.

Another significant advantage is that the alignment tolerance in coupling pump light to the large-area first cladding is typically tens of microns [37], rather than the submicron tolerance for coupling into a single-mode fibre core [9].

The drawback of DC fibres is the reduced pump light absorption compared to a core-pumped fibre, because of the small spatial overlap between the pump and the doped core that results in an increase of fibre length. The pump light absorption can be significantly improved by breaking the cylindrical symmetry of the inner cladding, using other geometries, such as D-shaped or rectangular pump cores. Alternatively, the absorption of pump radiation can be enhanced in symmetrical fibres by periodic bending of the fibre. A particularly effective design involves bending the fibre in a kidney-shaped geometry [38].

3.3.4 Pulsing methods

As already mentioned, one of the great attractions of fibre laser technology, is the possibility to operate from the CW regime down to pulse durations of just a few fs, thanks to the very large spectral bandwidths achievable from RE ions in glass.

In this paragraph a brief introduction to the main techniques for obtaining pulsed fibre laser is reported.

The simplest method of pulsing a fibre laser is to modulate the pump laser diodes. Because the rise time of the diode sources is around 5 μs, the minimum pulse duration achievable with this method is about 10 μs. Pulse repetition rates up to 50 kHz have been demonstrated.

A very common method for generating laser pulses, is the ***Q-switching*** technique that allows to obtain energetic short (but not ultrashort) pulses from a laser by modulating the intracavity losses and thus the Q factor (the ratio of the energy stored in the cavity to the energy loss per cycle) of the laser resonator. Q-switching involves inserting a switchable device in the laser cavity that initially has high loss and prevents the laser from operating. Then the loss of the device is quickly switched off and the laser can emit a short high power pulse.

Both active and passive switching elements have been used to this effect such as semiconductor saturable absorber mirrors (SESAM), electro-optic devices, acousto-optic devices or saturable Bragg reflectors.

In a passive Q-switch the absorption of laser radiation is dependent on the intensity. The switchable device becomes more transparent as the fluence increases, and at very high fluence levels the material saturates and becomes transparent. In an acousticoptic

Q-switch a fraction of the optical beam is diffracted out of the resonator as a result of the modulation of the refractive index by the oscillating mechanical pressure of a sound wave. In an electro-optic Q-switch, an external electric field is applied to a crystal to modulate its birefringence, in combination with one or more polarizing elements which translate any change of the state of polarization of the laser field into a loss modulation.

The minimum pulse durations from Q-switched fibre lasers are just a few nanoseconds, although pulse durations of the order or tens to hundreds of nanoseconds are more typical for cladding-pumped devices. Pulse energies can range up to 50 mJ.

As the pulse energy increases, the beam quality decreases. For typical Q-switched fibre lasers, the value of the beam quality parameter M^2 is ~1 for pulses with 1 mJ of energy, while increases to about 40 for pulse energy near 50 mJ.

Q-switched fibre lasers are mainly used in laser marking and micromachining.

Another method (or actually a group of methods) for generating laser pulses, is ***mode locking*** of lasers that allows producing pulses with very short duration, down to the femtosecond regime. A laser produces mode locked pulses when there is a fixed phase relationship between the modes in the resonant cavity. Interference between these modes produces a train of pulses of very short duration, typically between 30 fs and 30 ps, in extreme cases down to ~ 5 fs. For that reason, the peak power of a mode-locked laser can be orders of magnitude higher than the average power.

Both passive and active techniques have been used to produce mode locking.

In the first case, a passive nonlinear element (a saturable absorber) in combination with the radiation itself generates a periodic modulation that leads to a fixed phase relationship of the axial modes.

In the second case an RF signal applied to a modulator (electrooptic or acousto-optic) provides a phase or frequency modulation, which leads to mode-locking. Active mode locking is more complicated than passive one, because requires an additional operating device in the laser cavity and also an external modulating signal. However, it can provide higher pulse repetition rates than passive mode locking.

Ultrafast fibre lasers are used in several fields ranging from material processing to medical applications.

3.4 Nd^{3+} doped phosphate glass fibre laser

Fibre lasers are nearly as old as the glass laser itself. The first demonstration of a fibre laser dated back to the 1960's when C. J. Koester and E. Snitzer [39,40] developed a flash lamp pumped neodymium doped fibre with a large core. However, after these pioneering efforts, work in fibre lasers essentially stopped until 1985, when D. N. Payne and co-workers at Southampton University [41-43] reawakened interest in fibre lasers announcing the fabrication of the first low-loss single mode fibres containing Nd and Er, made by the extension of MCVD technology.

In that period, fibre lasers were investigated mainly for their applications in telecommunication field, as optical amplifier for both long-haul (1.5 μm) and local area network (1.3 μm). They were mostly single mode devices with an average output power that ranged from a few mW to at most tens of mW.

The next significant step forward in fibre laser evolution was the introduction in 1988 [36] of the double clad fibre structure (see section 3.3.3), that lead to a gradual increase in fibre laser output power in the intervening decade, thanks also to the increase of pump diode powers and brightness, as well as a decreasing cost per watt.

In the past few years, CW kW-level lasers have been demonstrated from RE doped silica fibres using length of tens of meters to provide an effective absorption of pump power [44]. Power scaling of these sources is eventually limited by stimulated Brillouin scattering (SBS) and photo-darkening, which can limit the maximum attainable output power or induce output power degradation over time.

Compared to silica host, phosphate glass can possess several advantages (see chapter 1) such as higher RE ion solubility, higher SBS threshold and higher photo-darkening threshold, that make them suitable for the realization of high power, high brilliance single-frequency laser sources.

To date, several cladding-pumped RE doped phosphate DC fibre lasers at 1.0–1.1 μm and 1.5 μm doped with Yb and Yb-Er, producing a multiwatt-level CW output power have been experimentally demonstrated [45-48], also in single-mode operation. At 1.5 μm *all fibre setup* fibre laser have been demonstrated, using fibre Bragg gratings to form the laser cavity [49,50]. These results confirmed that, although limited by

relative low thermal damage threshold, phosphate glass has a great potential as host materials for compact high-power and single-frequency fibre lasers.

Concerning Nd doping, CW or mode-lock operation of Nd phosphate glass laser in form of rod [51] and slab [52, 53] have been widely investigated [54] for high power laser amplifier systems, like that in the laser fusion program.

Less effort has been devoted to the realization of Nd-doped phosphate fibre lasers. Nonetheless some experimental demonstrations were reported in single clad and double clad fibres, as well as in photonic crystal fibre (PCF) and a multicore fibre [55-62].

Table 3.2 summarizes the main characteristics of representative Nd-doped phosphate fibre lasers reported in literature. The highest efficiency was reported in 2001 [60] by using a heavily Nd-doped DC phosphate fibre pumped by a laser diode emitting at 795 nm. Watt-level output power was obtained with less than 10 cm of active fibre, although in multimode operation.

More recently [62] single mode operation was reported in a DC fibre laser having an output power of 1.42 W and an efficiency of 34% with respect to the absorbed pump power. The result was obtained thanks to an improving of coupling efficiency between the pump diode and the active fibre obtained by local water cooling of the coupling point.

Table 3.2. Characteristics of representative cw Nd-doped phosphate fibre lasers .

Output wavelength [μm]	Nd concentration	Fibre length (cm)	Core diameter [μm]	Max output power [W]	Pumping wavelength [nm]	Threshold [W]	Efficiency vs absorbed pump power [%]	Efficiency vs launched pump power [%]	Other features	Ref.
1.053	2% Nd_2O_3	1.3	100	$130 \cdot 10^{-3}$	807	$98 \cdot 10^{-3}$	40	31		55
1.053				$8 \cdot 10^{-3}$	800		30.6			56
1.054	9 wt% Nd_2O_3	53	50	2.1	808	~2.3	34		DC	57
1.056	$2.26 \cdot 10^{20}$ cm^{-3}	21	20	$8.5 \cdot 10^{-3}$	808	$160 \cdot 10^{-3}$		2	microstructured	58
1.055	$2.26 \cdot 10^{20}$ cm^{-3}	8.5	8.2 each	$20 \cdot 10^{-3}$	808	$100 \cdot 10^{-3}$		9	3 core /phase lock	59
1.055	$2.26 \cdot 10^{20}$ cm^{-3}	9.5	8.2 each	$60 \cdot 10^{-3}$	808	$170 \cdot 10^{-3}$			7 core	59
1.053	$3.5 \cdot 10^{20}$ cm^{-3}	26	14	2.87	795		44.7		DC	60
1.053	$3.5 \cdot 10^{20}$ cm^{-3}	36	50	7.92	795	~2	38.1		microstructured	61
1.053	$3.5 \cdot 10^{20}$ cm^{-3}	21	5.3	1.42	808		34.1	18.4	DC - single mode	62

REFERENCES

[1] S. O. Kasap, " Optoelectronics and Photonics: Principles and Practices," Upper Saddle River: Prentice-Hall, 2001.

[2] J. P. Gordon et al., "The Maser—New Type of Microwave Amplifier, Frequency Standard, and Spectrometer," Phys. Rev. 99, pp. 1264-1274, 1955.

[3] T. H. Maiman, "Stimulated optical radiation in ruby," Nature 187, pp. 493–494, 1960.

[4] http://www.rp-photonics.com/

[5] F. J. Duarte, "Multiple-prism grating solid-state dye laser oscillator: optimized architecture," Appl. Opt. 38, pp. 6347-6349, 1999.

[6] http://www.worldoflasers.com/index.htm

[7] W. Koechner, M. Bass, "Solid-State Lasers: A Graduate Text, " Springer, 2003.

[8] P. C. Becker, N. A. Olsson, and J. R. Simpson, "Erbium-doped Fiber Amplifiers-Fundamentals and Technology," Academic Press Inc, San Diego, Calif, USA, 1997.

[9] M. J. F. Digonnet, "Rare-Earth-Doped Fiber Lasers and Amplifiers," 2a ed. New York: Marcel Dekker, Inc., 2001

[10] S. Hiifner, "Optical Spectra of Rare Earth Compounds," Academic Press, New York, 1978.

[11] J. H. Campbell and T. I. Suratwala, "Nd-Doped Phosphate Glasses for High-Energy/High-Peak-Powerlasers,"J. Non-Cryst. Solids 54, pp. 318-341, 2000.

[12] M. Yamane and Y. Asahara, "Glasses for Photonics," Cambridge University Press, 2004.

[13] B. R. Judd, "Optical Absorption Intensities of Rare-Earth Ions," Phys. Rev. 127, pp. 750-761, 1962.

[14] G. S. Ofelt, "Intensities of Crystal Spectra of Rare-Earth Ions,"J. Chem. Phys. 37, pp. 511-520, 1962.

[15] L. A. Riseberg and M. J. Weber, "Relaxation phenomena in rare earth luminescence," in Progress in Optics. E. Wolf, ed. North-Holland, Amsterdam, pp. 90–159, 1976.

[16] W. T. Carnell, et al., “Spectral Intensities of the Trivalent Lanthanides and Actinides in Solution. II. Pm^{3+}, Sm^{3+}, Eu^{3+}, Gd^{3+}, Tb^{3+}, Dy^{3+}, and Ho^{3+},” J. Chem. Phys. 49, pp. 4412-4423, 1968.

[17] T. Miyakawa and D. L. Dexter, “Phonon sidebands, multiphonon relaxation of excited states, and phonon-assisted energy transfer between ions in solids,” Phys. Rev. B1(7), pp. 2961–2969, 1970.

[18] L. A. Riseberg and H. W. Moos “Multiphonon orbit-lattice relaxation of excited states of rare-earth ions in crystals,” Phys. Rev. 174, pp. 429-438, 1968.

[19] R. Reisfeld and C. K. Jùrgensen, “Excited State Phenomena in Vitreous Materials in Handbook on the Physics and Chemistry of Rare Earth,” Vol. 9, ed. K. A. Gschneidner Jr. and L. Eyring, North Holland, Amsterdam, 1987.

[20] W. J. Miniscalco, “Erbium-doped glasses for fiber amplifiers at 1500 nm,” J. Lightwave Technol. 9, pp. 234-250, 1991.

[21] H. Kuroda, at al., “Development of highly repetitive phosphate glass lasers,” J. Appl. Phys. 51, pp 1351-1356, 1980.

[22] S. E. Stokowski: Laser program Annual Report - 83 (Lawrence Livermore National Laboratory, pp. 6-40, 1984.

[23] V. P. Gapontsev, V. P at al., “Erbium glass lasers and their applications,” Opt Laser Technol 14, pp.189–196, 1982.

[24] S. E. Stokowski, “CRC Handbook of Laser Science and Technology, Vol. I, Lasers and Masers,” Ed. M. J. Weber, CRC Press Inc., Boca Raton FL, p. 215, 1985.

[25] R. C. Powell, “Physics of Solid-State Laser Materials,” Springer, New York, 1998.

[26] C. Bibeau at al., “Direct measurements of the terminal laser level lifetime in neodymium-doped crystals and glasses,” J. Opt. Soc. Am. B 12, pp. 1981-1992, 1995.

[27] C. Bibeau and S. Payne, “Terminal-level relaxation in Nd-doped laser materials,” ICF Quarterly Report, Lawrence Livermore National Laboratory Report UCRL-LR-105821-95-2, p. 1-11, 1995.

[28] C. Bibeau, et al., "Pulse length and terminal-level lifetime dependence of energy extraction for neodymium-doped phosphate amplifier glass," IEEE J. Quantum Electron. 32, pp. 1487-1496, 1996.

[29] J. Nilsson and D. Payne, "High-power fiber lasers," Science 332 (6032), pp. 921-922, 2011.

[30] A. Tünnermann et al., "The renaissance and bright future of fibre lasers" J. Phys. B At. Mol. Opt. Phys. 38, pp. S681-S693, 2005.

[31] M. Shimizu et al., "High-efficiency Nd-doped fibre lasers using direct coated dielectric mirrors," Electron. Lett. 23, pp. 768–769, 1987.

[32] D. J. Richardson et al., "High power fiber lasers: current status and future perspectives," J. Opt. Soc. Am. B 27, pp. B63-B92, 2010.

[33] E. Stiles, "New developments in IPG fiber laser technology,"in Proceedings of the 5th International Workshop on Fiber Lasers, 2009.

[34] D. C. Brown et al., "Thermal, stress and thermo-optics effects in high average power double-clad silica fiber lasers, " IEEE J. Quantum Electron. 37, pp. 207-217, 2001.

[35] J. Limpert et al., "SPM-induced spectral compression of picosecond pulses in a single-mode Yb-doped fiber amplifier, " Appl. Phys. B 74, pp. 191–195, 2002.

[36] E. Snitzer et al., "Double-clad, offset core Nd fiber laser Optical Fiber Sensors," Proc. Conf. Optical Fiber Sensors, Postdeadline paper PD5, 1988.

[37] T. Weber et al., "Cladding-pumped fiber laser, ". IEEE J. Quant. Electron. 31, pp. 326–329, 1995.

[38] H. Zellmer et al., "Double-clad fiber laser with 30 W output power, "Proc Optical Amplifiers and Their Applications. OSA Trends Opt Photon Ser 16, pp. 137–140, 1997.

[39] E. Snitzer, "Optical Maser Action of Nd^{+3} in a Barium Crown Glass," Phys. Rev. Lett. 7, pp- 444-446, 1961.

[40] C.J. Koester and E. Snitzer, "Amplification in a fiber laser," Appl. Opt. 3, pp. 1182-1186, 1964.

[41] S. B. Poole et al., "Fabrication of low-loss optical fibres containing rare-earth ions," Electron. Lett. 21, pp. 737-738, 1985.

[42] R. J. Mears et al., "Neodymium-doped silica single-mode fibre lasers," Electron Lett. 21, pp. 738-740, 1985.

[43] S. B. Poole et al., "Fabrication and characterization of low-loss optical fibers containing rare earth ions," J. Lightwave Technol. LT-4, pp. 870-876, 1986.

[44] Y. Jeong et al., "Ytterbium-doped large-core fiber laser with 1.36 kW continuous-wave output power," Opt. Express 12, pp. 6088–6092, 2004.

[45] Y. W. Lee et al., "20W single-mode Yb^{3+}-doped phosphate fiber laser," Opt. Lett. 31, pp. 3255–3257, 2006.

[46] Y.W. Lee et al., "High-power Yb^{3+}-doped phosphate fiber amplifier," IEEE J. Sel. Topics Quantum Electron. 15, pp. 93–102, 2009.

[47] T. Qiu et al., "Generation of 9.3-W multimode and 4-W single-mode output from 7-cm short fiber lasers," IEEE Photon. Technol. Lett. 16, pp. 2592–2594, 2004.

[48] L. Li, M. Morrell et al., "Short cladding-pumped Er/Yb phosphate fiber laser with 1.5 W output power," Appl. Phys. Lett. 85, pp. 2721–2723, 2004.

[49] A. Schülzgen, et al., "Single-frequency fiber oscillator with watt-level output power using photonic crystal phosphate glass fiber," Opt. Express 14, pp. 7087–7092, 2006.

[50] A. Poynkin et al., "Single-frequency fiber ring laser with 1 W output power at 1.5 μm," Opt. Express 13, pp. 3179–3184, 2005.

[51] S. Kishida et al. "cw oscillation in a Nd: Phosphate glass laser," Appl. Phys. Lett. 34, pp. 273–275, 1978.

[52] L. Yan, et al., "An actively mode-locked continuous wave Nd: Phosphate glass laser oscillator and regenerative amplifier," IEEE J. Quantum Electron. 24, pp. 418–426, 1988.

[53] L. Yan et al., "Picosecond-pulse generation from a continuous-wave neodymium: Phosphate glass laser," Opt. Lett. 11, pp. 502–503, 1986.

[54] J. H. Campbell, "High-Power Solid-State Lasers: a Laser Glass Perspective," International Journal of Applied Glass Science 2, pp. 3-29, 2011.

[55] U. Griebner et al., "Efficient laser operation with nearly diffraction-limited output from a diode-pumped heavily Nd-doped multimode fiber," Opt. Lett. 21, pp. 266–268, 1996.

[56] G. Zhang et al., "Nd^{3+}-doped phosphate glass for fiber laser," Proc. SPIE 3862, International Conference on Industrial Lasers, 301, 1999.

[57] R.Wu et al., "Nd-doped cladding pumped fiber laser," in Proc. Fiber Optics and Communication Technologies Optics in the Southeast, Charlotte, NC, Nov. 4–5, 2001.

[58] G. Zhang et al., "Nd-doped phosphate glass microstructured optical fiber laser," Laser Phys. 20, pp. 1425–1427, 2010.

[59] G. Zhang et al., "Phase locking of a compact Nd-doped phosphate multicore fiber laser," Laser Phys. 21, pp. 1–4, 2011.

[60] G. Zhang, et al., "Efficient generation of watt-level output from short-length Nd-doped phosphate fibre lasers," IEEE Photon. Technol. Lett. 23, pp. 350–352, 2011.

[61] G. Zhang et al., "Neodymium-doped phosphate fiber lasers with an all-solid microstructured inner cladding," Opt. Lett. 37, pp. 2259-2261, 2012.

[62] G. Zhang et al., "Local-Cooled Watt-Level Nd-Doped Phosphate Single-Mode Fiber Laser," Laser Phys. 22, pp. 1235-1239, 2012.

Chapter 4

Glass fabrication and characterization

The first step towards the realization of a Nd^{3+}-doped phosphate glass fibre laser emitting at 1.06 μm is the design and engineering of the active material.

First of all a host glass composition was developed in-house in order to have a glass stable, robust, able to incorporate high amount of RE ions and suitable for fibre drawing. Several Nd^{3+}-doped phosphate glass samples were fabricated by doping the developed host glass with concentrations of Nd^{3+} up to 10 mol%. The samples were then characterized in order to measure their physical, thermal and spectroscopic properties. The effect of Nd^{3+} doping concentration on emission spectra and lifetimes was investigated in order to study the concentration quenching effect on luminescence performance.

In the first part of this chapter, the developed phosphate glass composition is reported and samples fabrication method is described. In the second part of the chapter, main glass characterization techniques are briefly reviewed and measurements results obtained from the fabricated glasses are presented and discussed. Particular attention is devoted to the fluorescence spectroscopy measurement, for which a dedicated setup on optical bench was realized as part of the work of this thesis.

4.1 Glass synthesis

Glass samples (30g batch) used in this research were prepared by conventional melt-quenching technique using chemicals of 99+% purity. The host glass with the

composition of $65P_2O_5{:}17Li_2O{:}3Al_2O_3{:}4B_2O_3{:}5BaO{:}6La_2O_3$ (mol%) was ad hoc developed for this research in order to have a stable and robust glass, able to incorporate high amount of RE and suitable for fibre drawing.

Six different glasses, named for short Nd1 ÷ Nd6, were obtained by doping the host material with an increasing level of Nd_2O_3 (ranging from 0.05 to 5 mol%) added in substitution of La_2O_3. The full list of glass samples manufactured for this research and their doping concentrations are reported in Table 4.1.

Table 4.1. Molar and ionic concentration of dopants in the manufactured phosphate glass samples.

Glass label	Nd^{3+} concentration	
	[mol%]	[x 10^{20} ions/cm^3]
Nd1	0.1	0.134
Nd2	1	1.32
Nd3	2	2.66
Nd4	4	5.33
Nd5	6	7.72
Nd6	10	13.3

In order to have the Li_2O, B_2O_3 and BaO in the final glasses, Li_2CO_3, H_3BO_3 e $BaCO_3$ were used, considering that in the furnace the following reactions will take place:

$$Li_2CO_3 \rightarrow Li_2 + CO_2 \tag{4.1}$$

$$2H_3BO_3 \rightarrow B_2O_3 + 3H_2O \tag{4.2}$$

$$BaCO_3 \rightarrow Ba + CO_2 \tag{4.3}$$

All the chemicals were weighted and mixed in a dry box in order to reduce the incorporation of OH groups in the glass, since they have negative influence on the radiation of RE ions in phosphate glasses and thus degrade the laser performance. Despite all the precautions taken during glass synthesis aiming at reducing the presence

of OH groups, a small quantity of these ions was anyway incorporated in the phosphate glass since they were generated during melting from reaction 4.2.

After weighing and mixing, the batched chemicals were melted in an alumina crucible in a vertical furnace at a temperature of 1500 ºC for 2 hours; a mix of O_2/N_2 gases was purged into the furnace during melting in order to minimize the hydroxyl ions (OH^-) content. The melt was then cast into a brass mould preheated at 480 °C and annealed at the same temperature for 10 h to relieve glass internal stresses.

The obtained glasses were cut down to 2 mm thickness samples using a precision cutter Hitech Europe C100 equipped with a diamond coated disc blade. Then they were lapped and polished to optical smoothness for optical and spectroscopic characterization. Lapping was carried out using a Logitech PM5 machine equipped with a cast iron plate with a suspension of 9 µm alumina in demineralized water. Optical polishing was obtained using Logitech PM5 equipped with a polyurethane plate with 1 µm diamond paste in water.

In figure 4.1 a picture of two polished samples is reported, the different colour being related to the different Nd^{3+} ion doping level.

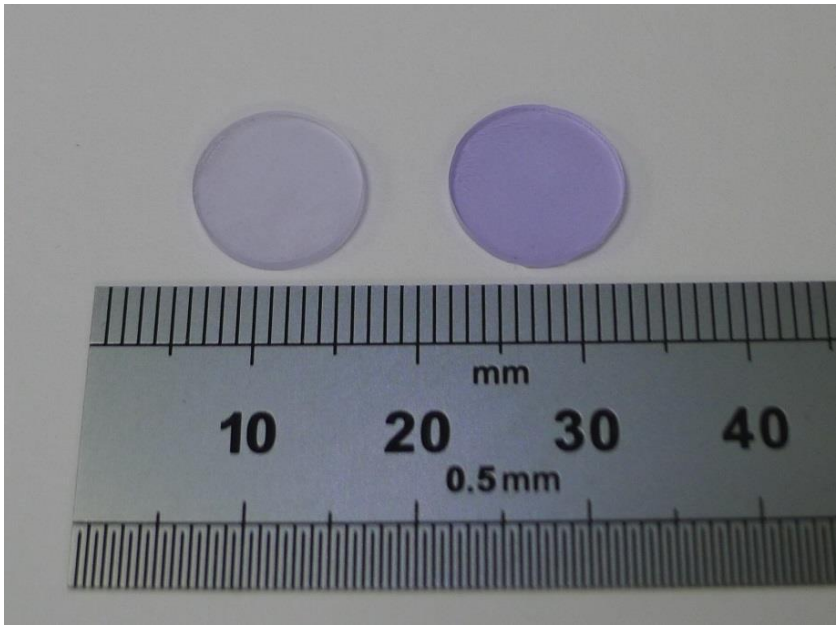

Figure 4.1. Nd doped phosphate glass samples after polishing.

4.2 Glass characterization techniques

4.2.1 Density measurement

Density of doped glass is required to calculate the dopant ionic concentration needed for the absorption cross section calculation (see section 4.2.6). A simple and effective method to determine density of a glass sample is based on Archimede's principle: upward buoyant force experienced by a submerged object is equal to the weight of the liquid displaced by the object.

The glass sample is weighed both in air and suspended in a liquid of known density (in our case distilled water). The difference in weight equals the weight of the displaced liquid. Since the density of the liquid is known, ρ_l, the displaced volume can be calculated using the formula:

$$V = \rho_l \, m \tag{4.4}$$

Thus knowing the weight of the sample in air, W, and the suspended weight of the sample W_s, the density of the glass ρ is calculated from the following expression:

$$\rho = \frac{W\rho_l}{(W - W_s)} \tag{4.5}$$

In order to obtain the true density of the material, the glass sample must be free of bubbles, voids or other defects that give a reduction of the density as well as crystals or particles of unmelted batch that tend to increase the measured density.

4.2.2 Thermal analysis

Thermal analysis is carried out on glass samples in order to measure the characteristic temperatures T_g (glass transition temperature) and T_x (onset crystallization temperature). Their measurement allows assessing the corresponding glass stability parameter $\Delta T = T_x\text{-}T_g$ that is an estimation of the fibre drawing ability of the glasses. In fact fibre drawing needs to take place at a temperature greater than T_g, where the glass is in a liquid phase and able to be processed and shaped into the optical fibre. A smaller ΔT, for a glass host, means smaller working range during sample fibre drawing, because the material tends to crystallize at or before drawing. Moreover with a small glass stability

parameter, it is difficult to find a suitable cladding glass with compatible thermal and optical properties.

Two thermoanalytical techniques were used to measure the fabricated glass samples: *differential scanning calorimetry* (DSC) and *differential thermal analysis* (DTA).

DSC measures the difference in the amount of heat required to increase the temperature of a sample and a reference as a function of temperature. Both the sample and reference are maintained at the same temperature during the experiment. The basic principle underlying this technique is that when the sample undergoes a physical transformation such as phase transitions, more or less heat will need to flow to it than the reference to maintain both at the same temperature. If the sample undergoes an exothermic process, it will require less heat, while in case of endothermic process more heat will need to flow to the sample.

An alternative technique to perform glasses thermal analysis is DTA. In this technique it is the heat flow to the sample and reference that remains the same rather than the temperature. When the sample and reference are heated identically, phase changes and other thermal processes cause a difference in temperature between the sample and reference.

In summary, DSC measures the energy required to keep both the reference and the sample at the same temperature while DTA measures the difference in temperature between the sample and the reference when they are both put under the same heat. Both DSC and DTA provide similar information on thermal properties of a glass sample.

Figure 4.2 shows a typical DSC curve obtained for a generic glass sample. As the temperature of the sample is increased, glass transitions may occur and this transition will appear as a step change in the curve, considering that no formal phase change takes place, but only a change in heat capacity. With further increase of temperature, the glass will become less viscous and, at the crystallization temperature T_x, the molecules will gain enough freedom of motion to spontaneously arrange themselves into a crystalline form. This transition is an exothermic process and results in a positive peak in the DSC signal. As the temperature increases, the sample eventually reaches its melting temperature T_m. Since the melting is an endothermic process, it results in a negative peak in the DSC curve.

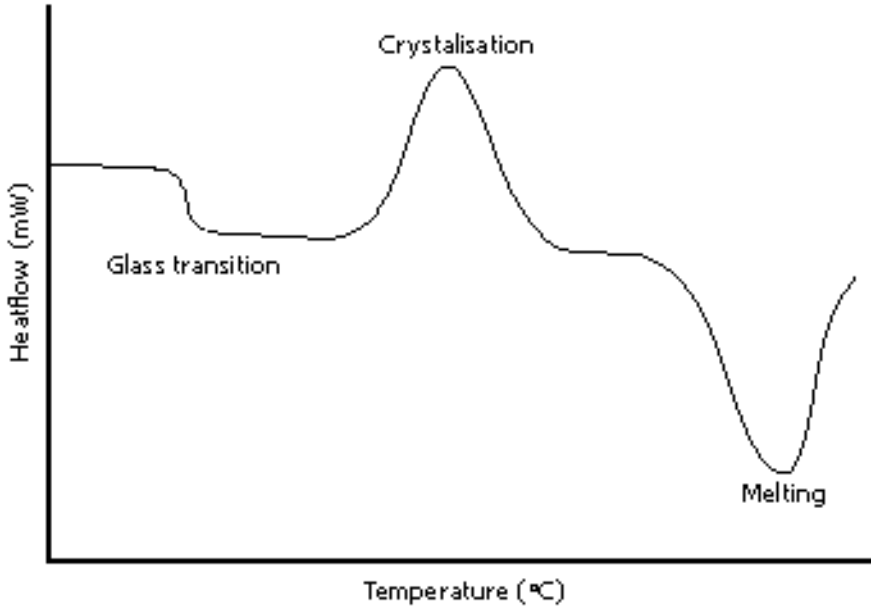

Figure 4.2. Typical DSC curve obtained for a generic glass sample. Conventionally exothermic process are shown with a positive peak.

For this research, DSC analysis on fabricated glass samples were performed using a Perkin Elmer DSC-7 differential scanning calorimeter up to 550 ºC under Ar flow with a heat rate of 10 ºC /min in sealed Al pans using typically 30 mg samples.

DTA analysis were performed using a Netzsch DTA 404 PC Eos differential thermal analyzer up to 1400 ºC under Ar flow with a heat rate of 10 ºC/min in sealed Pt pans using typically 30 mg samples.

In both cases the glass sample was broken into small pieces in order to have a better thermal contact with the pan's bottom.

In order to determine the onset characteristic temperatures of the glass from the DSC/DTA curve, the tangent method was used. The temperature was found as the intersection of tangents to the curve, traced on the baseline and on the low temperature peak side.

An error of ± 3 ºC was observed in measuring the characteristic temperatures.

4.2.3 Dilatometry

Dilatometry is a thermo-analytical method for measuring the shrinkage or expansion of materials under negligible load when subjected to a controlled temperature program. It

allows obtaining the thermal expansion coefficient α_L of the material. The latter is defined as the fractional change in length per degree of temperature change and it is expressed as:

$$\alpha_L = \frac{1}{L_0}\frac{\Delta L}{\Delta T} \tag{4.6}$$

where L_0 is the initial length and $\frac{\Delta L}{\Delta T}$ is the change of length due to the temperature change ΔT.

To perform a dilatometric analysis, in this research, a horizontal pushrod dilatometer was used. The sample under test is inserted into a holder within a movable furnace. A pushrod is positioned directly against the sample and transmits the length change to a linear variable displacement transducer (LVDT). As the sample length changes over the temperature program, an output signal proportional to the displacement is recorded. The temperature is measured by a thermocouple placed in direct proximity to the sample. Since the measuring system is exposed to the same temperature as the sample and thereby likewise expands, it is thus necessary to correct the raw dilatometer data in order to subtract the effect of the system.

Figure 4.3 shows a typical diagram obtained from dilatometric analysis for a generic glass sample. Due to the thermal expansion of the material, the height of the sample increases linearly as the temperature increases up to the glass transition temperature where the glass softens. The slope of the linear range gives the thermal expansion coefficient of the material.

At the glass transition temperature, rearrangements that occur in an amorphous material lead to characteristic discontinuity of thermal expansion coefficient. This discontinuity allows an estimation of the glass transition temperature.

In this research, measurements of the thermal expansion coefficient of the glasses were performed with a dilatometer Netzsch Dil 402 PC with high displacement sensitivity (up to 8 nm) and a temperature range up to 1550 °C. The samples were cylinders of about 25 mm of height and they were placed in an alumina holder. The thickness as a function of time and temperature was recorded as the temperature was increased at a rate of 5°C/min under a constant compressive force of 5 mN.

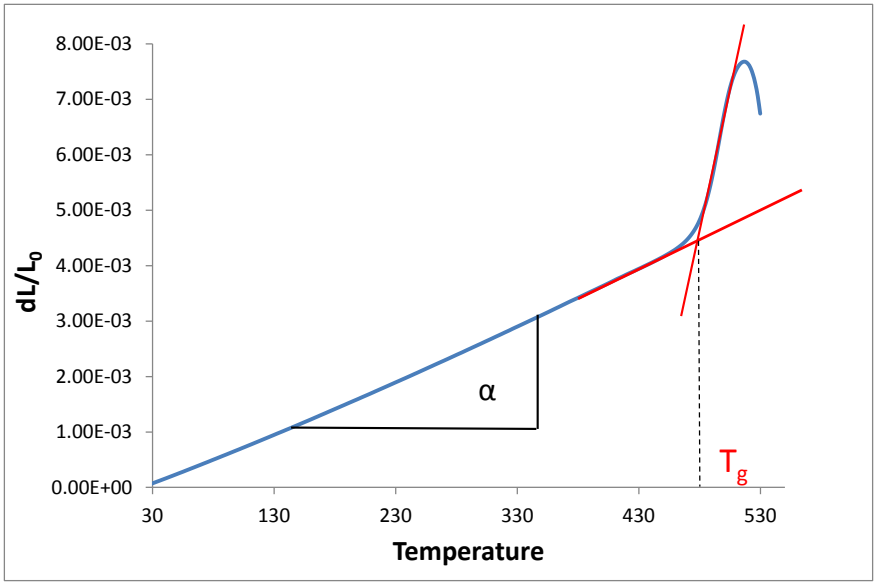

Figure 4.3. Typical diagram obtained from dilatometric analysis for a generic glass sample.

4.2.4 Refractive index measurement

The propagation of light through the core of an optical fibre is based on total internal reflection of the light wave (see section 2.4). In order to realize an optical fibre, it is thus essential to engineer glasses for the core and the cladding with a definite refractive index contrast.

In this research, the refractive index of the manufactured glasses was measured by prism coupling technique using the instrument Metricon, model 2010/M. The instrument is equipped with 5 lasers emitting at the wavelength of 633, 825, 1061, 1312 and 1533 nm, so dispersion curve (index versus wavelength) can be obtained.

The refractive index measurement principle is shown in figure 4.4. If a bulk material with index n is brought into close contact with a prism with index n_p, laser light directed onto the base of the prism will be totally reflected at the prism base until the angle of incidence becomes less than the critical angle Θ_c, where

$$\Theta_c = \arcsin\left(\frac{n}{n_p}\right) \tag{4.7}$$

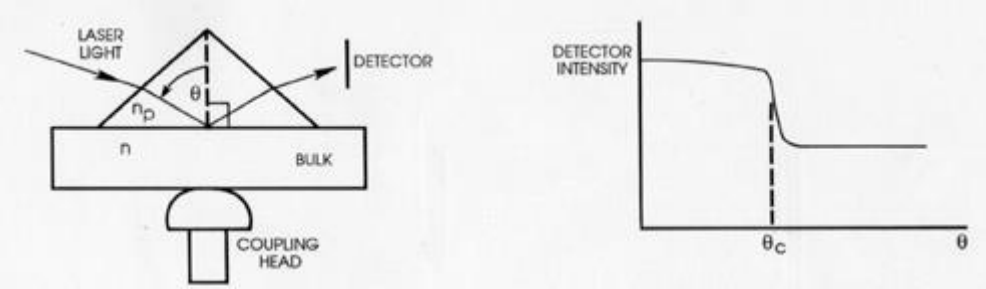

Figure 4.4. Refractive index measurement principle by prism coupling technique [1].

Θ_c is easily measured using the detector in Fig. 4.4, since the detector intensity drops abruptly as Θ drops below the critical angle and light starts to leak into the bulk material. Since n_p is known, n can then be determined from Equation 4.7.

4.2.5 Absorption spectroscopy

Absorption spectroscopy is one of the fundamental optical characterizations of a doped glass. In fact a complete knowledge of the absorption levels of the glass is crucial in order to make a proper choice of the most suitable pump wavelength for fluorescence/laser applications.

Absorption spectra are recorded by measuring the optical transmittance of a sample with a broadband light source. Light from the source is passed through a dispersing element and light exiting from the sample is recorded using a detector. The spectrometer output is usually given in terms of *absorbance* defined as:

$$A = log_{10}\left(\frac{1}{T}\right) = log_{10}\left(\frac{I_0}{I}\right) \tag{4.8}$$

where T is the transmittance, I_0 is the intensity of light before it passes through the material (incident radiation) and I is the light that has passed through the material (transmitted radiation).

The absorbance could also be expressed by Lambert-Beer's law as linear function of the light path length in the material:

$$A = \varepsilon cL \tag{4.9}$$

where ε is the molar absorptivity, c the molar concentration of absorbing species in the material and L is the distance the light travels through the material (i.e. the path length).

For a solid containing N non-interacting absorbing centres per unit volume which absorb radiation at a wavelength λ, the attenuation of a beam of intensity I_0 by a solid of thickness L is also expressed as:

$$I = I_0\, e^{(-\propto L)} \tag{4.10}$$

where α is the absorbing coefficient of a the material at a particular wavelength, expressed in cm^{-1}. Thus it can be written:

$$\alpha(\lambda) = \frac{1}{L}\, ln\left(\frac{I_0}{I}\right) \tag{4.11}$$

The relationship between absorbance A and $\alpha(\lambda)$ is given by:

$$A = \frac{\alpha L}{2.303} \tag{4.12}$$

It is also possible to define an absorption cross section of the dopant, in our case Nd^{3+} ion as:

$$\sigma_a = \frac{\alpha}{N} \tag{4.13}$$

where N is the concentration of the Nd^{3+} ions per cm^3. Thus from equation 4.12 it can be derived:

$$\sigma_a(\lambda) = \frac{2.303\ \mathrm{A}(\lambda)}{NL} \tag{4.14}$$

with L, the glass sample thickness, expressed in cm.

UV–VIS–NIR spectroscopy was carried out on all prepared samples for wavelengths ranging from 300 to 3000 nm using a double beam scanning spectrophotometer Varian Cary 500. The use of a double beam operation (see for reference figure 4.5) increases the accuracy of the measurements.

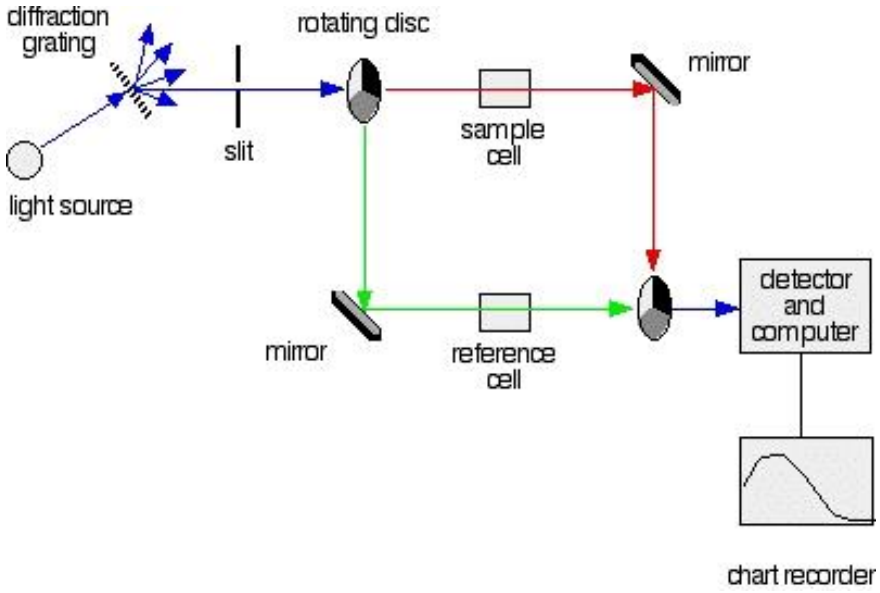

Figure 4.5. Schematic diagram of a double beam spectrometer.

To extract all necessary data from the raw absorption spectra received from the spectrometers, the baseline of each spectrum was corrected, since we were only interested in the effect of RE dopants and not in the properties of the glass host. Then from each spectrum, using equation 4.14, the absorption cross section of Nd^{3+} ion was calculated.

The inhomogeneously broadened bands of the spectra were assigned to the transitions from the ground state $^4I_{9/2}$ to the excited states of Nd^{3+} ions using the Russel-Saunders notation (see section 3.2.1) using as reference the Nd^{3+} energy levels diagram reported in figure 3.7.

4.2.6 Fluorescence spectroscopy

In order to study the emission properties of RE doped glass samples, a dedicated optical bench was developed in clean room environment. The bench was conceived to be versatile not only for use with the Nd^{3+} doped glasses studied for this research, but also for other RE dopants, such as Er^{3+}, Yb^{3+},Tm^{3+},Pr^{3+}, Dy^{3+}, etc.

Figure 4.6 and 4.7 show a schematic illustration and pictures respectively of the developed experimental setup. Glass sample is excited by laser light emitted by

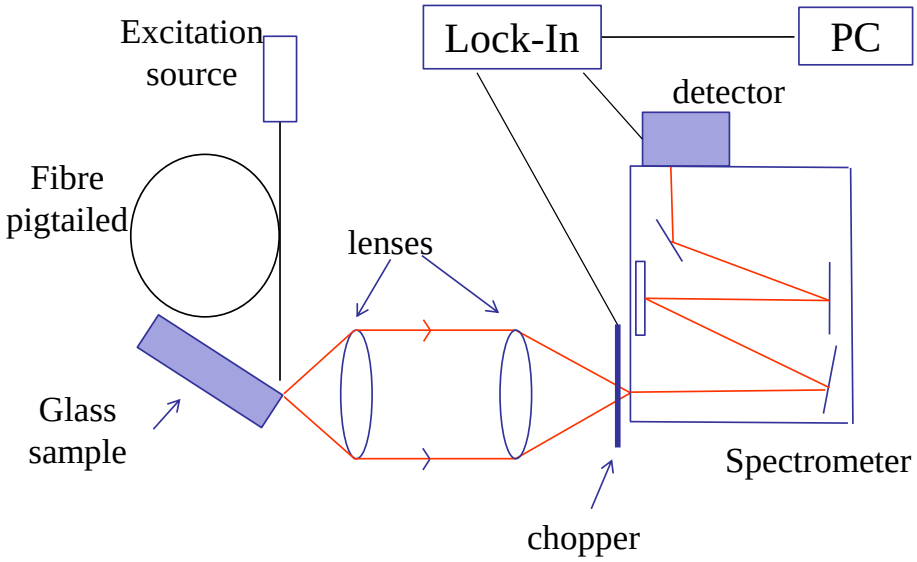

Figure 4.6. Schematic illustration of the experimental setup realized for RE emission spectroscopy measurement.

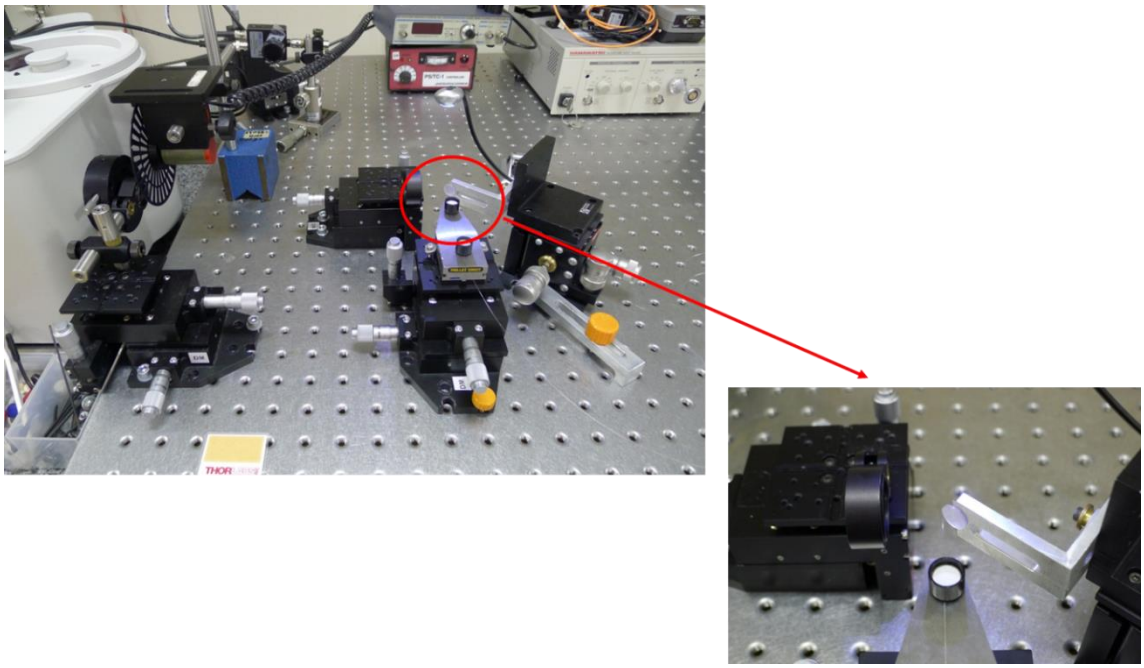

Figure 4.7. Pictures of the experimental setup realized for RE emission spectroscopy measurement. On the right the Nd^{3+} doped sample and the fibre pigtailed of the laser diode used as excitation source are visible.

semiconductor pigtailed laser diode at a suitable wavelength depending on the absorption bands of the RE doping of the glass under test. If requested, as excitation light, also broadband sources could be used.

Several laser diodes and broadband sources are available for testing glass sample with different RE doping:

- 660 nm, SM fibre pigtailed, output power up to 10 mW (Qphotonics QFLD-660-10S);
- 785 nm, MM fibre pigtailed, up to 1.4 W (Axcel B1-785-1400-15A);
- 795 nm, SM free space, up to 150 mW (Qphotonics QLD-795-150S);
- 793 nm, MM fibre pigtailed, up to 35 W (LIMO35-F200-DL793-EX1360);
- 976 nm, SM fibre pigtailed, up to 650 mW (3SPGroup 1999CHP);
- 1300 nm, SM fibre pigtailed, up to 2 mW;
- 1550÷1600 nm (tunable), SM fibre pigtailed, up to 5 mW (HP 8168F);
- Supercontinuum source (Coheras SuperK Extreme);
- UV lamp (Hamamatsu LC 8).

Fluorescence light emitted from the sample is then collected by suitable optics and sent to the entrance of the spectrometer, a Jobin Yvon iHR320, that resolves light in its components through a diffraction grating monochromator with a spectral resolution up to 0.2 nm (see for reference Fig. 4.8). The spectrometer can host two detectors in parallel, able to detect light in different portions of the electromagnetic spectrum. Several detectors are available for this measurement:

- Photomultiplier tube Hamamatsu R928P: range from 200 to 900 nm;
- Solid state cooled PbSe single channel detector (DSS-PSE020T): range from 1 to 5 μm;
- InAs cooled single channel detector (Hamamatsu P4631-02): range from 1 to 3.45 nm;
- InGaAs dectector (PDA10D Thorlabs): range from 1.2 to 2.6 μm;
- InGaAs dectector (PDA10CS Thorlabs): range from 0.7 to 1.8 μm.

The photodetector converts fluorescence light into photocurrent which is amplified and converted to a voltage signal. Since the signal could be weak, phase sensitive

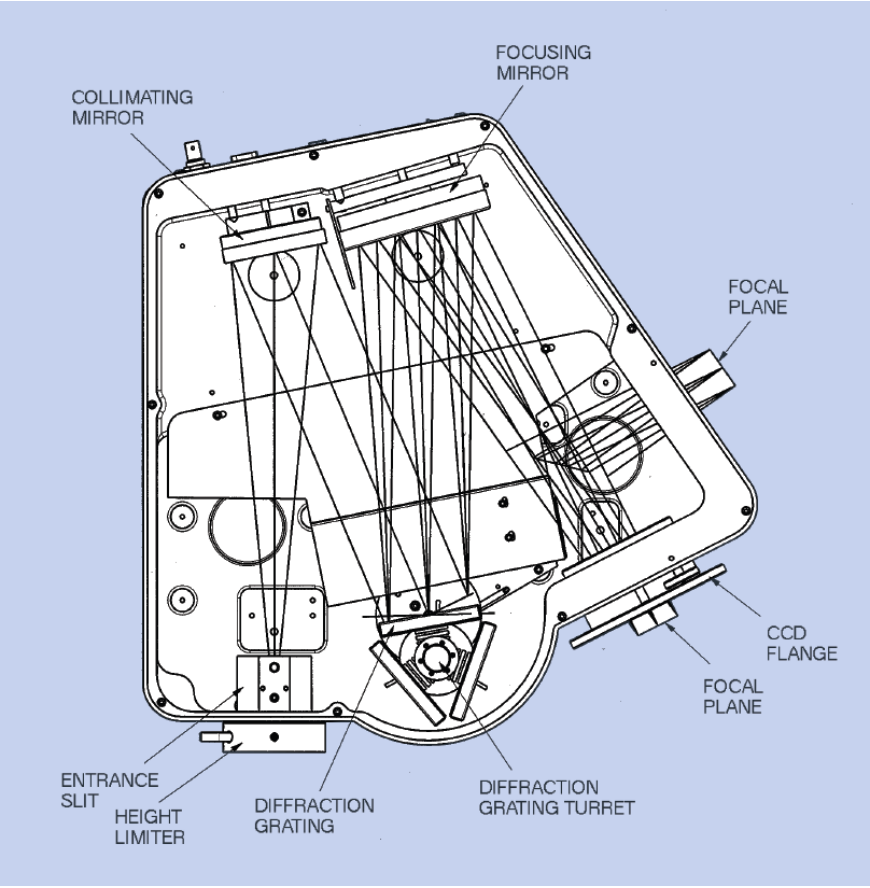

Figure 4.8. Schematic of the operation principle of the spectrometer Jobin Yvon iHR320 [2].

detection techniques is usually employed in order to reduce noise of the electrical measurement. The fluorescence light is modulated by a chopper at a certain reference frequency (usually 1 KHz); the detection system, equipped with a lock-in amplifier (SR830DSP) is then set to record signals at the reference frequency only. This effectively eliminates all noise signals except those closely centred on the modulation frequency.

Fluorescence spectra of Nd^{3+} doped samples fabricated for this research were acquired using the Jobin Yvon spectrometer equipped with the InAs cooled single channel detector Hamamatsu P4631-02. Emission spectra were obtained by exciting the samples with a monochromatic light at the wavelengths of 785 nm, emitted by a fibre pigtailed laser diode (Axcel B1-785-1400-15A). Figure 4.9 reports a picture and the emission spectrum of the butterfly module laser diode used.

Fluorescence spectra were collected by exciting the samples at the very edge in order to minimize reabsorption.

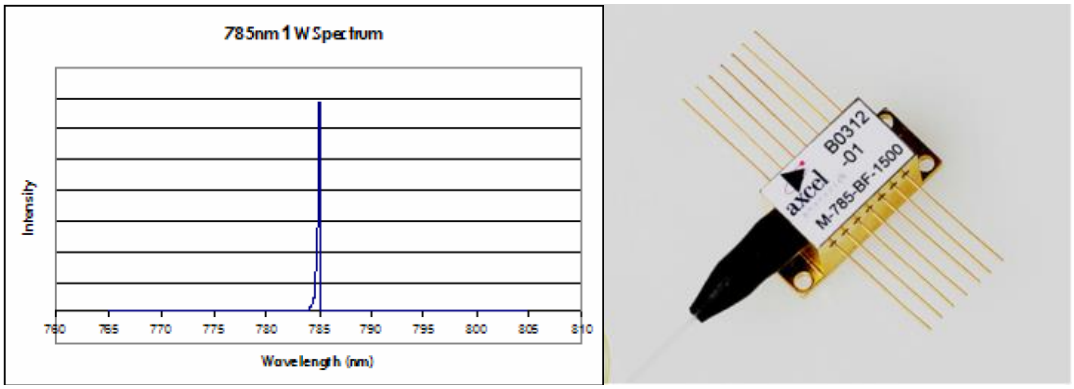

Figure 4.9. Emission spectrum of the laser diode Axcel B1-785-1400-15A used for emission spectroscopy measurement of the fabricated glass samples. Inset: picture of the butterfly module laser diode [3].

4.2.7 Time resolved emission spectroscopy

Another experimental parameter required for characterizing the emission properties of RE ions in a host medium, and therefore its suitability for active optical devices, is the excited state lifetime. Moreover, the fluorescence lifetime is one of the requested parameter for laser design.

Lifetime is the expected time before the excited state electron returns to a lower energy state by photon emission. In particular for a Nd^{3+}-doped laser operated at 1.06 μm, the important parameter is the ${}^4F_{3/2}$ level lifetime: the longer the lifetime, the higher the population inversion between this level and the ${}^4I_{11/2}$ one.

Figure 4.10 reports a schematic of the experimental setup used for lifetime measurements. Glass sample is excited by pulsed laser light emitted by semiconductor pigtailed laser diode at a suitable wavelength depending on the absorption bands of the RE doping of the glass under test. Pulses are usually in the range 5÷20 Hz, depending from the lifetime that is being measured. In fact, in order to perform a correct measurement, after a pulse it is necessary that all the excited state electrons decay to the ground state before the following pulse arrives.

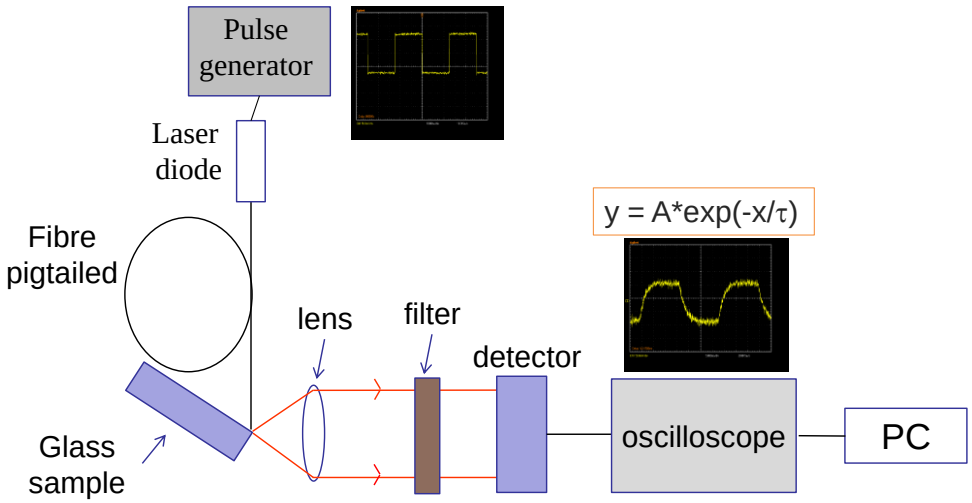

Figure 4.10 Schematic illustration of the experimental setup realized for fluorescence lifetime measurement.

The fluorescence emitted light is then collected by a lens and sent to the entrance of a detector. A suitable filter is used to select the emission wavelength range to be measured. The detector signal is displayed and recorded by a digital oscilloscope. The lifetime τ is then obtained by fitting the stored decay traces by single exponential ($exp(t/\tau)$).

Lifetime measurements must be collected by exciting the samples at the very edge in order to minimize reabsorption.

Figure 4.11 shows a typical decay trace obtained from a time resolved emission spectroscopy measurement. The point corresponding to the pump switched off is highlighted. From this moment the signal correspond to the emission of light from excited state electron that returns to a lower energy state.

For this research, the decay curves of the $^4F_{3/2}$ were measured for all the fabricated Nd^{3+}-doped glasses obtained by exciting the samples at the wavelength of 785 nm emitted by a fibre pigtailed laser diode (Axcel B1-785-1400-15A) with a repetition rate of 20 Hz. The detector used was a Thorlabs PDA10CS and the dichroic filter a Thorlabs FEL 950. The choice of the detector was driven by the high sensitivity in the wavelength range of Nd^{3+} main emission (see figure 4.12) and the fast response time necessary for measuring the fluorescence decay.

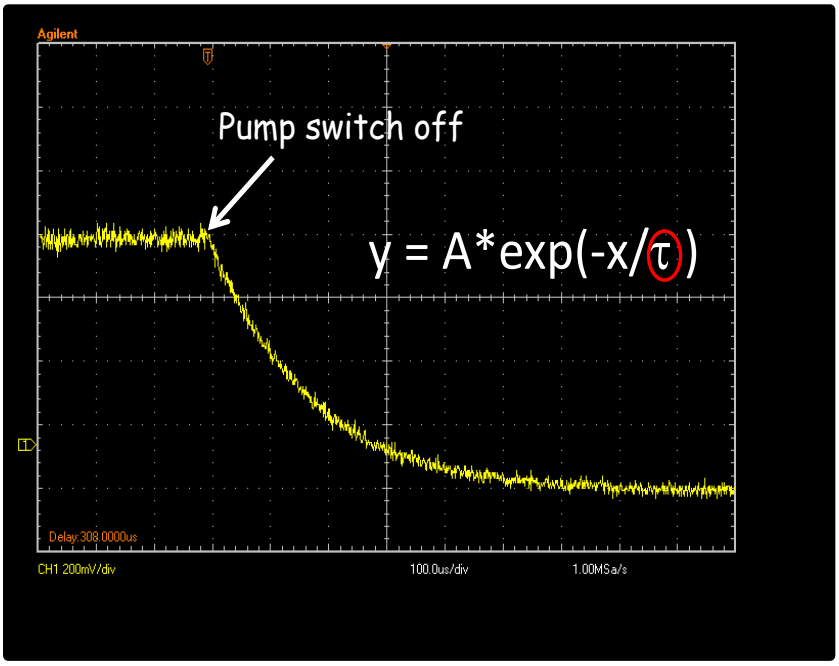

Figure 4.11. Typical fluorescence decay trace used for excited state lifetime measurement.

The decay traces were then recorded by a digital oscilloscope (Tektronix TDS350) and fitted by single exponential. The fits were performed between 10% and 90% of the measured intensity in order to cut on one side the possible pump residual effect and on the other side data with low signal to noise ratio.

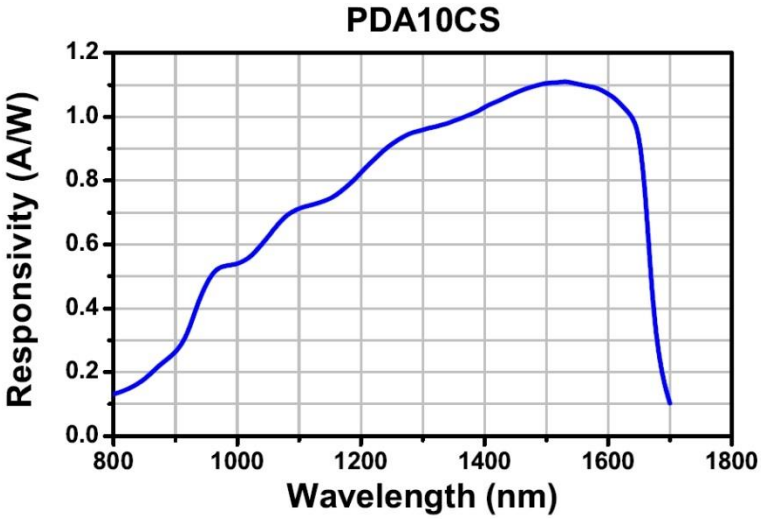

Figure 4.12. Response curve of detector PDA10CS used for lifetime measurement [4].

4.3 Results and discussion

4.3.1 Physical and thermal properties

Table 4.2 reports the typical physical properties of the manufactured glass samples. These values did not change significantly with changing the doping level of the glasses, due to the fact that the doping oxide Nd_2O_3 was added in substitution of La_2O_3 in the host matrix.

Table 4.2. Typical physical properties values of the manufactured glass samples.

Density	2.88 ± 0.05 g/cm^3
Glass transition temperature (T_g)	509 ± 3 ºC
Crystallization temperature (T_x)	702 ± 3 ºC
Glass stability parameter ($\Delta T = T_x - T_g$)	193 ± 6 ºC
Coefficient of thermal expansion	10 E-6 °C^{-1}

The measured characteristic temperatures, T_g and T_x, indicate satisfying thermal properties of the glasses. As already discussed in section 4.2.2, their measurement allowed assessing the corresponding glass stability parameter $\Delta T = T_x - T_g$ that is commonly used as an estimate of the glass stability and of glass ability to be processed in fibre form without crystallization. The obtained value is about ΔT = 193 ± 6 ºC, which suggests that these glasses are suitable for preform fabrication and crystal-free fibre drawing.

Figure 4.13 reports DSC curves obtained from the samples Nd1÷Nd6.

Concerning the linear thermal expansion coefficient, although this value remains an order of magnitude higher than silica glass, it is nonetheless suitable for practical applications, in particular in the form of thin glass fibres.

4.3.2 Refractive index measurement

Refractive index of the Nd^{3+}-doped glasses was measured at 5 different wavelengths by prism coupling technique. Five scans were performed for each wavelength, the average value of these five measurements representing the refractive index. Estimated error on

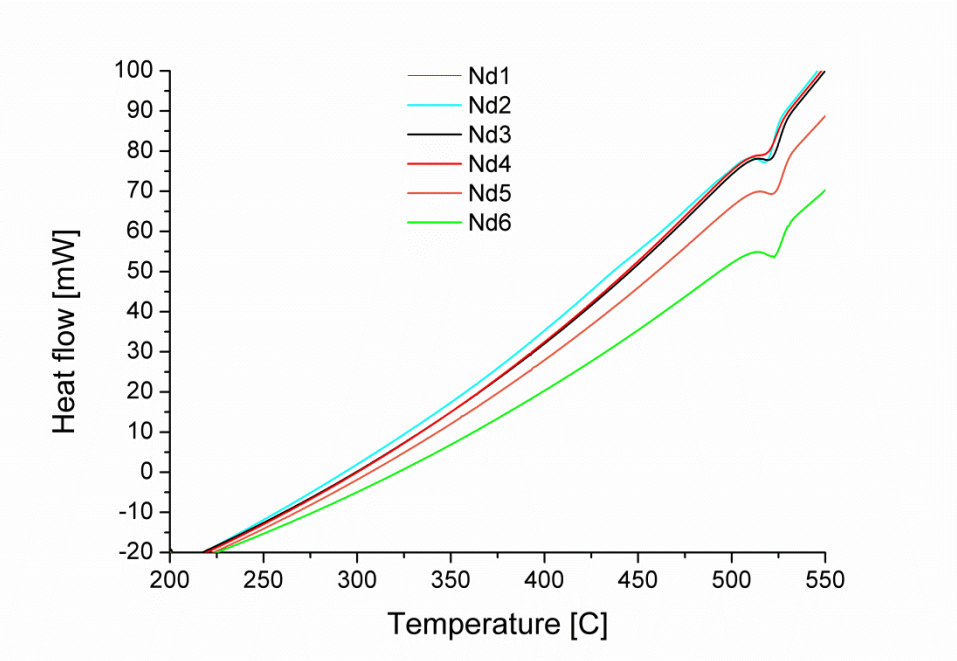

Figure 4.13. DSC curves obtained from glass samples Nd1÷Nd6.

the measurement was 0.001. The measured refractive indexes of the manufactured glass samples are reported in Table 4.3.

Table 4.3. Refractive index of the manufactured glasses at 5 different wavelengths. Estimated error on the measurement is 0.001.

Glass sample	Wavelength [nm]				
	633	825	1061	1312	1533
Nd1	1.5516	1.5456	1.5431	1.5392	1.5359
Nd2	1.5514	1.5462	1.5426	1.5394	1.5367
Nd3	1.5528	1.5477	1.5422	1.5389	1.5363
Nd4	1.5507	1.5456	1.5421	1.5391	1.5364
Nd5	1.5468	1.5456	1.5409	1.5367	1.5343
Nd6	1.5482	1.5436	1.5389	1.5368	1.535

The refractive index of each sample was found, as expected, to decrease monotonously with increasing wavelength. The wavelength dependence of the

refractive index is called dispersion and it is described by empirical formula such as the Cauchy or Sellmeier equations [5].

Figure 4.14 reports the dispersion curve of glass Nd2 fitted by the Cauchy equation:

$$n = B + \frac{C}{\lambda^2} + \frac{D}{\lambda^4} \tag{4.15}$$

The following values of fitting parameters were obtained: B = 1.5320, C = 1.3207 and D = -2.2014.

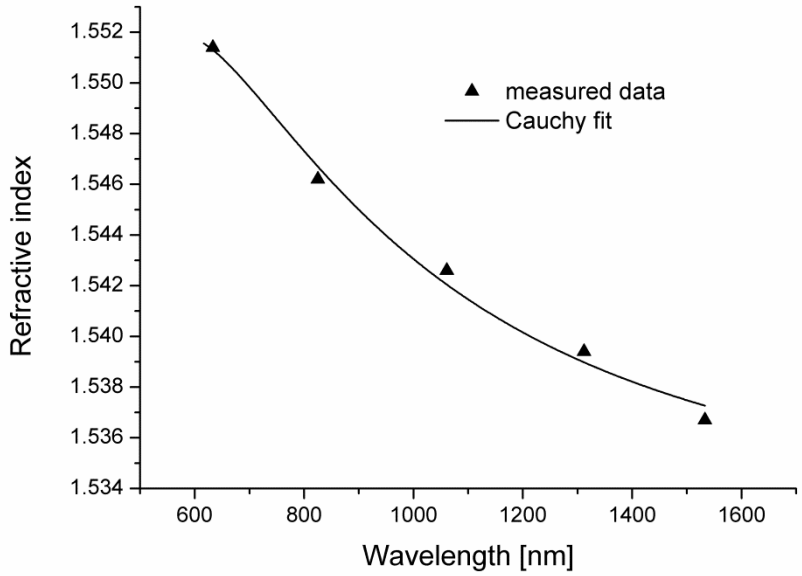

Figure 4.14. Dispersion of sample Nd2 with Cauchy fit of the experimental data.

4.3.3 UV-VIS-NIR spectroscopy

UV–VIS–NIR spectroscopy was carried out on all prepared samples and absorption spectra were recorded. Absorption cross-section σ_a was calculated from experimental data using equation 4.14. The sample thickness was measured with a calliper, the Nd^{3+} ionic concentration was calculated as:

$$N\left[\frac{ions}{cm^3}\right] = \frac{Wt\%(Nd_2O_3)}{MM(Nd_2O_3)[gmol^{-1}]}\ 2\ N_A\ [mol^{-1}]\rho[gcm^{-3}] \tag{4.16}$$

where *Wt%* and *MM* are respectively the weight percentage and the molecular mass of dopant, N_A is the Avogadro constant ($6.022 \cdot 10^{23}$ mol^{-1}), while ρ is the density measured as described in paragraph 4.2.1.

Figure 4.15 shows the absorption cross-section values obtained for glass sample Nd04. The inhomogeneously broadened bands are assigned to the transitions from the ground state $^4I_{9/2}$ to the excited states of Nd^{3+} ions (see for reference Figure 3.7).

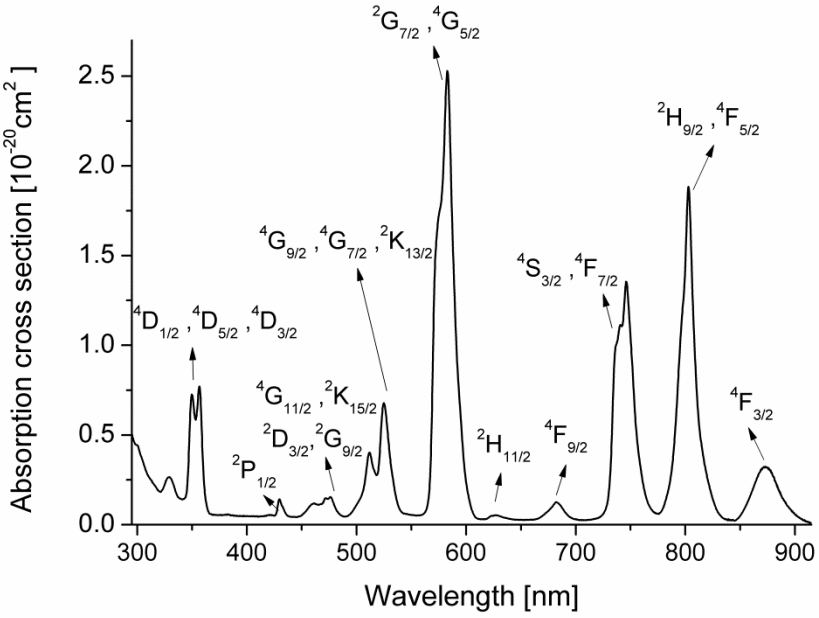

Figure 4.15. Absorption cross-section spectrum for sample Nd04. The main Nd^{3+} levels are labelled, considering absorption from the ground state $^4I_{9/2}$.

The occurrence of the strong absorption peak of the transitions $^4I_{9/2} \rightarrow {}^2H_{9/2} + {}^4F_{5/2}$ allows pumping at about 800 nm by AlGaAs diode lasers. This pumping is extremely effective for exciting the $^4F_{3/2}$ metastable state leading to very efficient Nd^{3+} doped diode pumped fibre laser. Despite the large number of closely spaced excited states, it is noteworthy that Nd^{3+} does not suffer more from ESA. In fact the $^4F_{3/2} \rightarrow {}^2D_{5/2}$ ESA transition occurs at a wavelength close to 800 nm, but it is extremely weak and does not significantly degrade the 800 nm pumping. For all glasses Judd-Ofelt analysis reveals that oscillator strength is less than 1% of the GSA transition [6].

4.3.4 Fluorescence emission spectra

Fluorescence spectra of the Nd^{3+} single doped glass samples, Nd1 ÷ Nd6, were measured in the wavelength range 1000÷1500 nm upon excitation at 785 nm.

A typical spectrum is shown in figure 4.16. The emission spectrum consists of two large and non-symmetric bands: a main peak centered around 1055 nm assigned to the transition $^4F_{3/2} \rightarrow {}^4I_{11/2}$ and a less intense peak centered around 1325 nm corresponding to the $^4F_{3/2} \rightarrow {}^4I_{13/2}$ transition of Nd^{3+} ion (see section 3.2.4).

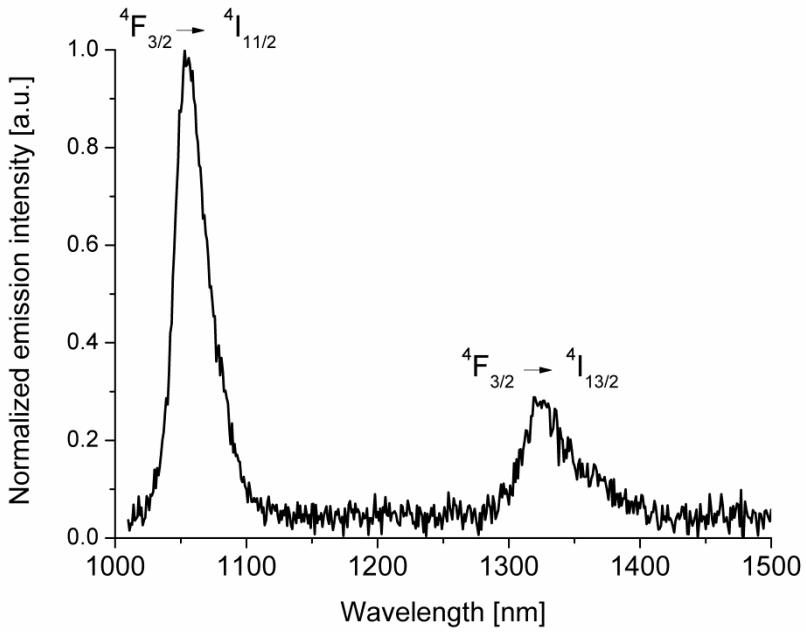

Figure 4.16. Emission spectra of the sample Nd5 (6 mol% Nd^{3+} concentration) upon excitation at 785 nm.

Further analysis on the fluorescence spectra indicated that the shape of the main emission peak did not change with increasing Nd^{3+} doping level. Fig. 4.17 reports the peak height of the 1055 nm emission with respect to the Nd^{3+} ion concentration. It can be observed that the peak emission intensity increases steadily with rising doping concentration, due to the increasing absorption of pump source at the beginning stage. But when Nd^{3+} concentration becomes higher than 7.7 x 10^{20} ions/cm^3 (sample Nd5) the absorption saturation of pump source is reached and the rate of the increase of emission intensity starts decreasing. Moreover, for high Nd^{3+} ions concentration, unwanted energy transfer between Nd^{3+} ions occurs, hence decreasing the fluorescence intensity.

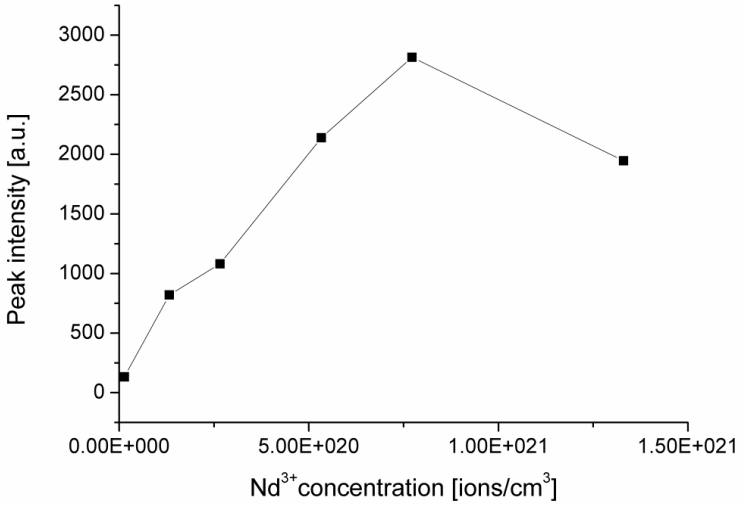

Figure 4.17. Dependence of the peak height of the Nd^{3+}: ${}^4F_{3/2} \rightarrow {}^4I_{11/2}$ transition on Nd^{3+} ion concentration.

Fluorescence spectra of the Nd^{3+} single doped glass samples, Nd1 ÷ Nd6, were also measured in the wavelength range 850÷930 nm upon excitation at 785 nm.

A typical spectrum is shown in figure 4.18. The emission spectrum, assigned to the transition ${}^4F_{3/2} \rightarrow {}^4I_{9/2}$, consists of a large and non-symmetric band with a maximum peak around 878 nm and a shoulder which extends towards higher wavelengths.

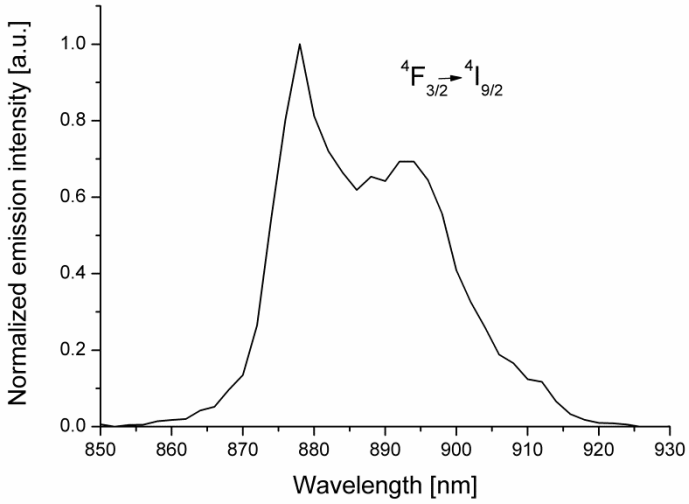

Figure 4.18. Emission spectra of the sample Nd2 (1 mol% Nd^{3+} concentration) upon excitation at 785 nm.

4.3.5 Fluorescence lifetime

The fluorescence lifetime determines the decay rate for radiation from a particular transition. It is an essential parameter for the characterization of the emission properties of RE ions in a host medium, and therefore its suitability for active optical devices. Moreover, the fluorescence lifetime is one of the requested parameter for laser design.

As already discussed in section 4.2.7, for a Nd^{3+}-doped laser operated at 1.06 μm, the important parameter is the $^4F_{3/2}$ lifetime. A longer lifetime of level $^4F_{3/2}$ benefits the population inversion between this level (the upper laser level) and the $^4I_{11/2}$ one (the lower laser level).

The decay curves of the Nd^{3+}: $^4F_{3/2}$ was measured under 785 nm excitation for all single doped and co-doped samples and the results are listed in Table 4.4. Examples of the measured curves are reported in Fig. 4.19 with intensity expressed in logarithmic scale.

Table 4.4. Fluorescence decay time of the $^4F_{3/2}$ state of Nd^{3+} ion in doped samples under laser excitation at 785 nm.

Glass label	Nd^{3+} concentration	Nd^{3+}:$^4F_{3/2}$ lifetime
	[mol%]	[μs] ±15μs
Nd1	0.1	365
Nd2	1	358
Nd3	2	327
Nd4	4	212
Nd5	6	177
Nd6	10	92

From the data of Table 4.4, it can be observed that the lifetime of Nd^{3+}:$^4F_{3/2}$ decreases with increasing dopant concentration, because of the unwanted energy transfer between ions at high concentration levels. This concentration dependence, referred to as concentration quenching, has important implications for the performance of active devices because it results in the loss of excitation, and thus an efficiency reduction. This effect could be described by the empirical formula [6]:

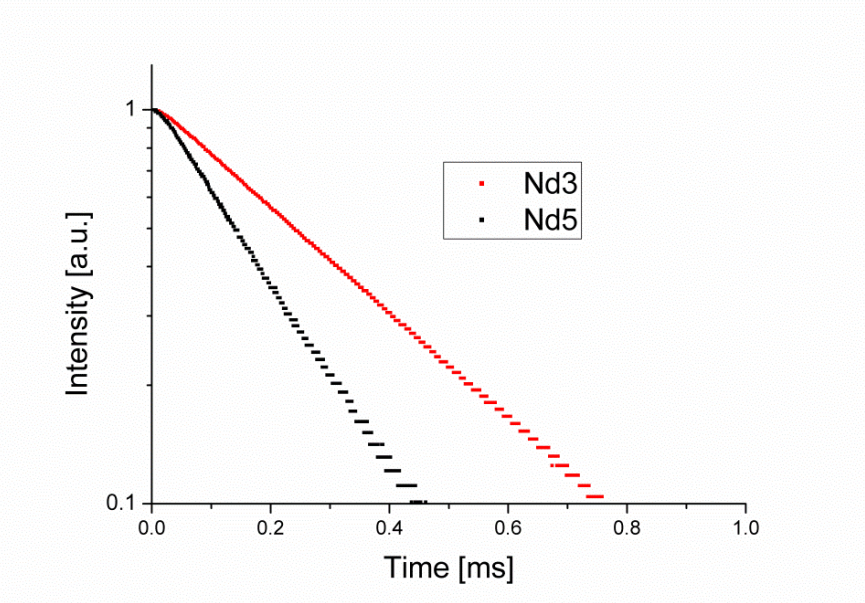

Figure 4.19. Room temperature decay curves of the Nd^{3+}: $^4F_{3/2}$ in two different samples obtained upon excitation at 785 nm. The intensity data are reported on a Log scale.

$$\tau(N) = \frac{\tau_0}{1+\left(\frac{N}{N_0}\right)^2} \tag{4.17}$$

where τ is the measured lifetime at a given Nd^{3+} ion concentration N, τ_0 is the lifetime in the limit of "zero" concentration, i.e. the radiative lifetime and N_0 is the quenching concentration.

The experimental data were fitted by the above formula and good agreement with the fit curve for the whole range of concentration was found (see figure 4.20). The following values of fitting parameters were obtained: τ_0 = 367 μs and N_0 = 8.47 E+20 ions/cm^3. These results agree with values reported in literature [7-8].

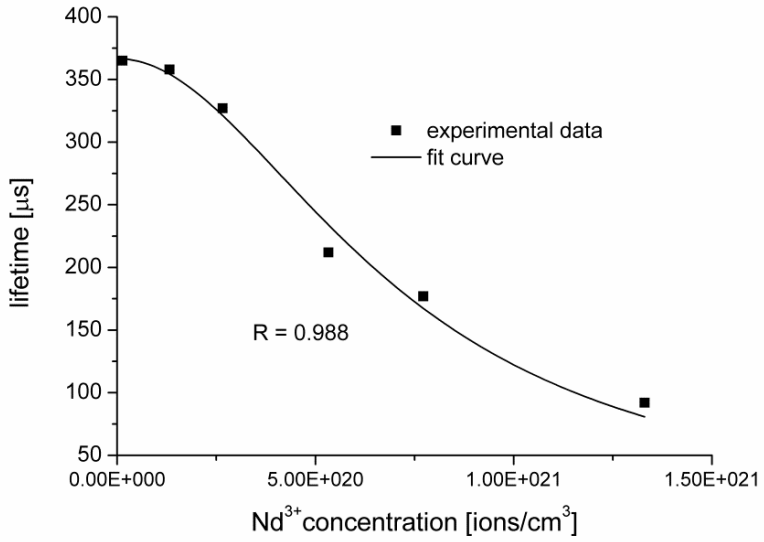

Figure 4.20. Experimental and fitted values of Nd^{3+}: $^4F_{3/2}$ excited state lifetime in single doped samples Nd1÷Nd6.

4.3.6 Conclusions

In this chapter physical and optical properties of a novel Nd^{3+} doped phosphate glass system proposed for the development of a fiber laser emitting at 1.06 μm are presented. All prepared glass samples were homogeneous and presented a good thermal stability and thus were found suitable for fiber drawing. A strong emission at 1.06 μm was measured for each glass sample by using a laser emitting at the wavelength of 785 nm as excitation source.

The effect of Nd^{3+} doping concentration on optical properties was investigated in order to study the concentration quenching effect on luminescence performance. No changes in the shape of the fluorescence spectrum were found with increasing the Nd^{3+} doping level. Lifetimes of the Nd^{3+}:$^4F_{3/2}$ were found to decrease with increasing Nd^{3+} concentration. The following characteristic values parameters were obtained: radiative lifetime τ_0 = 367 μs and quenching concentration N_0 = 8.47 E+20 ions/cm^3.

REFERENCES

[1] www.metricon.com

[2] www.horiba.com

[3] www.axcelphotonics.com

[4] www.thorlabs.com

[5] F. A. Jenkins and H. E. White, "Fundamentals of Optics," 4th ed., McGraw-Hill, Inc. 1981.

[6] M. J. F. Digonnet, "Rare-Earth-Doped Fiber Lasers and Amplifiers," 2a ed. New York: Marcel Dekker, Inc., 2001.

[7] J. H. Campbell and T. I. Suratwala, "Nd-Doped Phosphate Glasses for High-Energy/High-Peak-Powerlasers,"J. Non-Cryst. Solids 54, pp. 318-341, 2000.

[8] S. A. Payne et al., "Laser properties of a new average-power Nd-doped phosphate-glass," Appl. Phys. B 61, pp. 257-266, 1995.

Chapter 5

Fibre drawing and fibre laser demonstration

The first part of this chapter reports on the fabrication of three different phosphate glasses using a custom designed glass composition, with the aim to fabricate a Nd^{3+}-doped DC optical fibre laser emitting at 1.06 µm. By changing properly the concentration and constituents present in our phosphate glass, the refractive indexes of the three glasses were adjusted in order to obtain an adequate numerical aperture between core and inner cladding, and between inner and outer cladding, while maintaining similar thermo-mechanical properties in view of the fibre drawing process. Physical, thermal and spectroscopic properties of the glasses are presented and discussed.

In the second part of the chapter, the fabrication of the preform and the drawing of the Nd^{3+}-doped DC optical fibre are described. Morphological and optical characterisation of the fibre are reported and discussed.

In order to optimize Nd^{3+}-doped fibre laser design, a numerical analysis of the lasers was performed and resulting design curves are presented.

At last, the experimental demonstration of a CW cladding pumped fibre laser based on 9 cm of fabricated Nd^{3+}-doped optical fibre is reported. Experimental setup, fibre laser PI curve along with laser emission spectrum are presented and preliminary conclusions of the work are also drawn.

5.1 Glass fabrication and characterization

5.1.1 Glass composition and synthesis

Glass samples used for optical fibre fabrication were prepared by conventional melt-quenching technique using chemicals of 99+% purity. Three different glasses (core, inner cladding and outer cladding) were manufactured in order to obtain the desired refractive index contrast and then the desired NA between core and inner cladding, and between inner cladding and outer cladding. The details of the glass composition are given in Table 5.1.

Table 5.1. Composition of the phosphate glasses synthetized to fabricate the DC optical fibre.

Glass	mol (%)								
	P_2O_5	Li_2O	Al_2O_3	B_2O_3	BaO	PbO	MgO	La_2O_3	Nd_2O_3
Core	65	9	3	4	5	7	-	6	1
Inner cladding	65	14	3	4	2	5	-	7	-
Outer cladding	65	20	8	4	-	-	3	-	-

The composition of the core was slightly changed compared to the Nd^{3+} glasses reported in Chapter 4 (reduction of Li_2O contents and addition of PbO) in order to allow a more precise tailoring of the refractive index as requested for the fibre fabrication. Moreover the fabrication method was partially modified, reducing melting temperature and time, in order to reduce the incorporation of alumina of the crucible into the glass, to avoid crucible fracture during glass preparation and improve reproducibility of the glass properties/performances.

The chemicals were weighted and mixed inside a dry box in order to reduce the incorporation of OH^- groups in the glass. The core composition was doped with 2.3 wt.% of Nd_2O_3, corresponding to $2.4 \cdot 10^{20}$ Nd^{3+} ions/cm^3. The batched chemicals were then transferred into an alumina crucible for melting in a furnace for 1h at 1350° C, with a flux of a mix of O_2/N_2 gases in order to minimize the OH^- content. The melt was

then cast into a brass mould preheated at 400° C and annealed at 480° C for 10 h to relieve glass internal stresses.

The obtained glasses were cut to about 2 mm thick samples using a precision cutter Hitech Europe C100 equipped with a diamond blade. Then they were lapped and polished to optical smoothness for optical and spectroscopic characterization. The lapping was realized using a Logitech PM5 equipped with a cast iron plate with a suspension of 9 µm alumina in demineralized water. Optical polishing was performed using Logitech PM5 equipped with a polyurethane plate with 1 µm diamond paste.

5.1.2 Physical and thermal properties

Thermal properties, linear thermal expansion coefficient and refractive index of fabricated glasses are reported in Table 5.2.

Table 5.2 Glass transition temperature (T_g), crystallization temperature (T_x), glass stability parameters (ΔT), linear thermal expansion coefficient and refractive index of the manufactured phosphate glasses.

Glass	T_g [°C] ± 3° C	T_x [°C] ± 3° C	$\Delta T = T_x - T_g$ [°C] ± 6° C	α [E-6 °C^{-1}] ± 0.5 E-6 °C^{-1}	n @ 1061 nm ±0.001
Core	489	675	186	9.7	1.571
Inner cladding	489	675	186	9.5	1.561
Outer cladding	485	672	187	10.2	1.516

The measured characteristic temperatures, T_g and T_x, indicate good thermal properties of the glasses. The resulting stability parameter ($\Delta T = T_x - T_g$) is higher than 185 ºC and thus demonstrates that these glasses are stable against crystallization and suitable for fibre drawing. This result is mainly related to the presence of network modifiers (B_2O_3, Al_2O_3) that, in phosphate glass, helps enhancing the stability against devetrification.

Concerning the linear thermal expansion coefficient, although this value remains an order of magnitude higher than silica glass, it is nonetheless suitable for practical applications, in particular in the form of thin glass fibres.

From the measured refractive indexes, it is possible to calculate the numerical aperture of the core and of the inner cladding of the fibre to be manufactured by using the equation (5.1):

$$NA = \sqrt{n_a^2 - n_b^2} \tag{5.1}$$

where n_a and n_b are respectively the refractive index of the core and inner cladding, for the NA of the core, and the refractive index of inner cladding and outer cladding for the NA of the first cladding, both at the wavelength of 1061 nm.

The results obtained are 0.18 for NA of the core and 0.37 for NA of the inner cladding.

5.1.3 Absorption spectroscopy

UV–VIS–NIR spectroscopy was carried out on core sample glass and absorption spectra were recorded. Absorption cross-section σ_a was calculated from experimental data using the formula 4.13.

Figure 5.1 shows the absorption cross-section values obtained for the core glass sample. The inhomogeneously broadened bands are assigned to the transitions from the ground state $^4I_{9/2}$ to the excited states of Nd^{3+} ions (for reference on Nd^{3+} energy levels, see section 3.2.4).

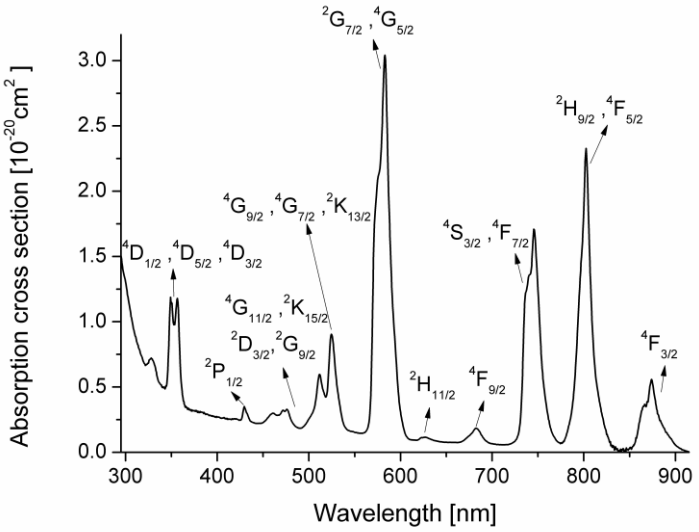

Figure 5.1. Absorption cross-section spectrum for core sample. The main Nd^{3+} levels are labelled, considering absorption from the ground state $^4I_{9/2}$.

As already observed in 4.3.3, the occurrence of the strong absorption peak of the transitions ${}^4I_{9/2} \rightarrow {}^2H_{9/2} + {}^4F_{5/2}$ allows pumping at about 800 nm by AlGaAs diode lasers. This pumping is extremely effective for exciting the ${}^4F_{3/2}$ metastable state leading to very efficient Nd^{3+} doped diode pumped fibre laser.

5.1.4 Emission spectroscopy

Figure 5.2 illustrates the fluorescence spectra of the core glass in the wavelength range 1000÷1500 nm under 785 nm excitation. The emission spectrum consists of two large and non-symmetric bands: a main peak centred at around 1055 nm corresponding to the transition ${}^4F_{3/2} \rightarrow {}^4I_{11/2}$ and a less intense peak centred at around 1325 nm assigned to the ${}^4F_{3/2} \rightarrow {}^4I_{3/2}$ transition of Nd^{3+} ion.

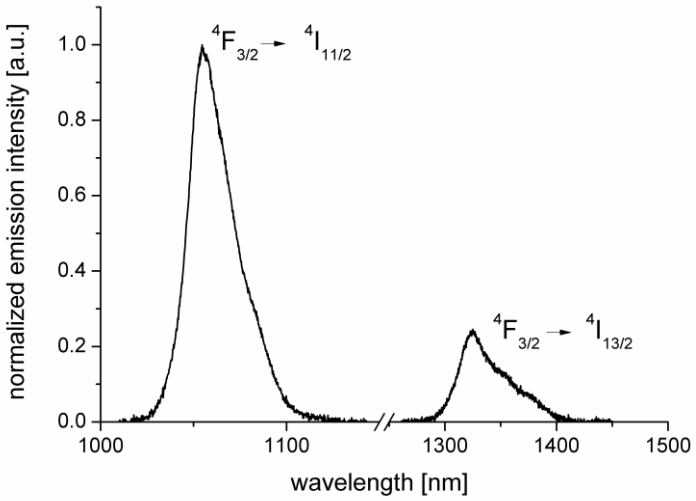

Figure 5.2. Emission spectra of the core sample under excitation at 785 nm.

As already mentioned in section 4.2.7, an important experimental parameter required to characterize the emission properties of RE ions in a host medium, and therefore its suitability for active optical devices, is the fluorescence lifetime. Moreover, the fluorescence lifetime is one of the requested parameter for laser design.

For a Nd^{3+}-doped laser operated at 1.06 μm, the important parameter is the ${}^4F_{3/2}$ lifetime: the longer the lifetime, the higher the population inversion between this level and the ${}^4I_{11/2}$ one.

The decay curves of Nd^{3+}:$^4F_{3/2}$ was measured under 785 nm excitation for core glass, the value obtained is 305 ± 15 μs (Fig. 5.3). This result is in line with previous measurements performed on similar glass system in order to evaluate the effect of concentration quenching on luminescence performance at high concentration level (see chapter 4).

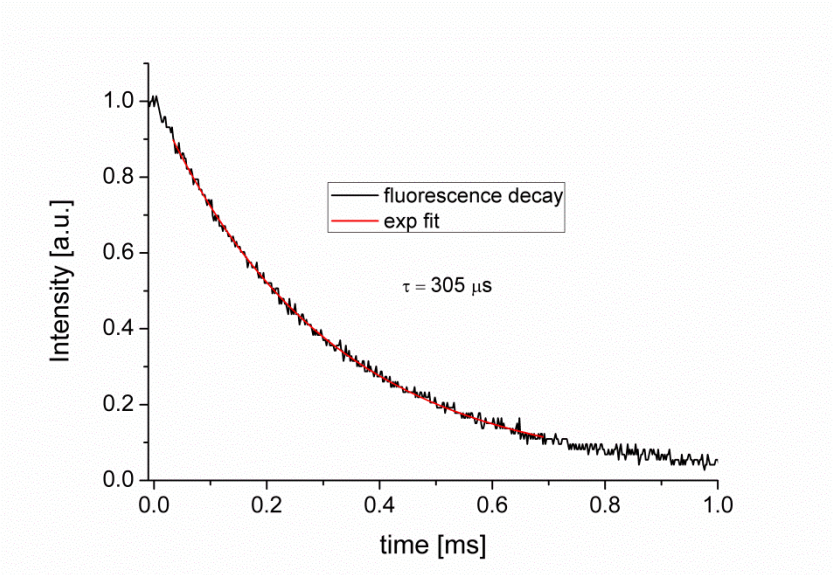

Figure 5.3. Room temperature decay curves of the Nd^{3+}: $^4F_{3/2}$ in core glass sample under excitation at 785 nm. In red the exponential fit is reported.

5.2 Fibre drawing and characterization

5.2.1 Fibre fabrication

The most important step for the fibre quality is the preform fabrication. The first step for the fabrication of the preform used in this work was to fabricate the core rod. Core glass composition was melted and cast in a pre-heated cylindrical brass mould. In order to obtain excellent surface quality, the rod core was polished with SiC papers of different grain sizes. In figure 5.4 a picture of the manufactured core rod is shown.

The phosphate glass tubes used for the claddings were produced by means of rotational casting technique from the molten glass at a rotation speed of 3000 rpm using an equipment developed in-house. The parameters of the rotational casting process (rotation speed and time, casting temperature and mould temperature) were optimized

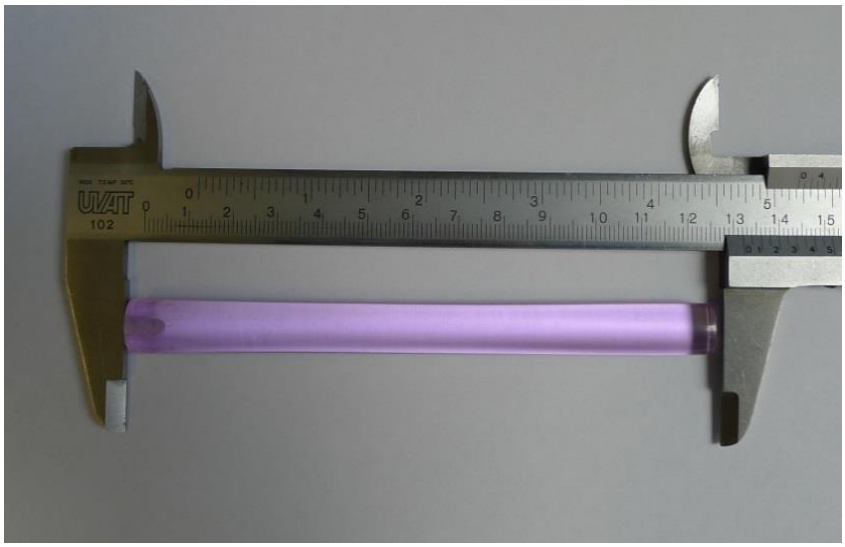

Figure 5.4. The core glass rod after polishing.

for the inner and outer cladding glass compositions. This process allows obtaining fibres with very good interfaces between core-inner cladding and inner-outer claddings, using the inner surfaces of the tubes as fabricated so without any post processing [1]. The external surfaces of the cladding tubes were polished carefully with SiC papers of different grain sizes. In figure 5.5 a picture of the fabricated rod for the core and tubes for the claddings is shown.

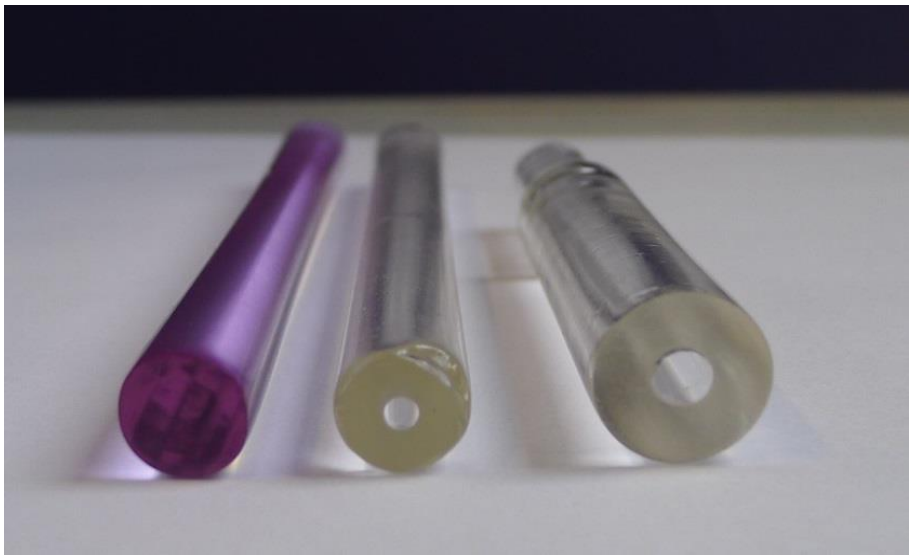

Figure 5.5. The core glass rod and claddings tubes after polishing of the external surfaces.

The preform was then manufactured by rod-in-tube technique, as described in paragraph 2.7.1, with one additional step in order to realize a DC structure. The core rod was stretched in the drawing tower available in our laboratory, to fit into the inner cladding tube. After stretching, the rod was inserted in the inner cladding tube. The obtained core/first cladding structure was then stretched and placed in the second cladding tube (see figure 5.6).

The preform and fibre fabrication parameters were set to generate a DC fibre with the following diameters: 8 μm, 35 μm and 105 μm for the core, inner and outer cladding, respectively. The preform was drawn into fibre at a speed of 6 m/min under a tension of 200 mN using the drawing tower. The fibre diameter was monitored during the drawing process. About 200 m of pristine fibre were manufactured without showing any sign of crystallization.

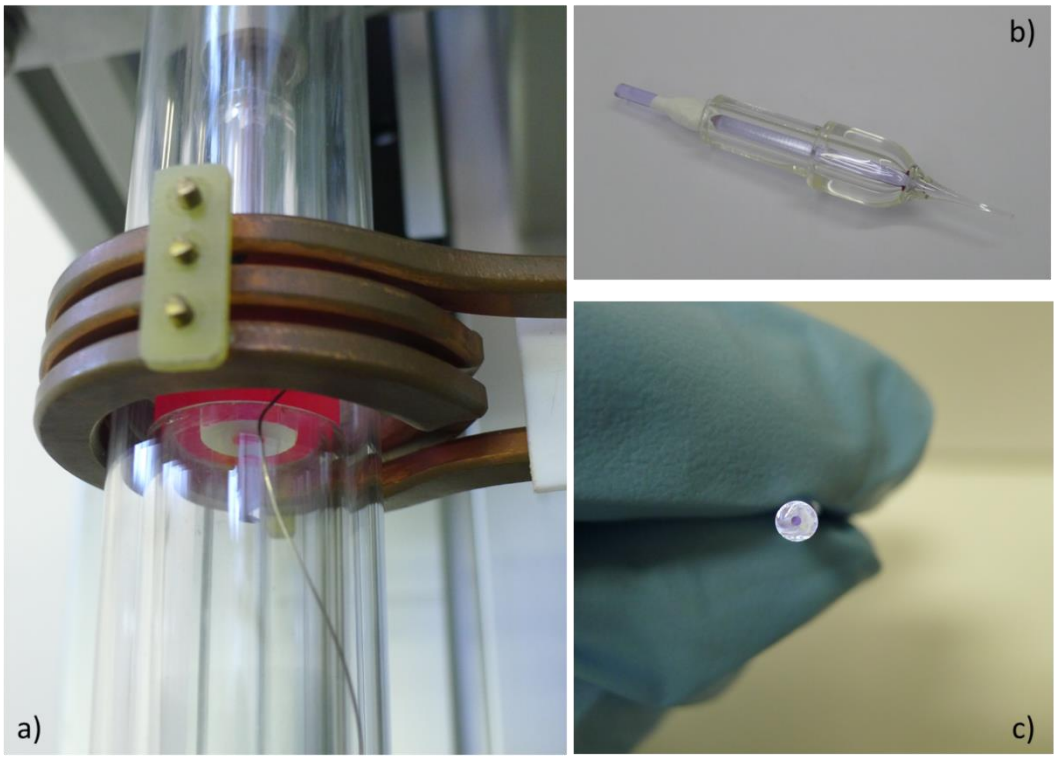

Figure 5.6 Fabrication of the preform by rod-in-tube technique. Core rod stretching in the drawing tower furnace consisting in a graphite ring heated by induction (a); neck down of the core-inner cladding structure after drawing (b); core-inner cladding rod obtained after the stretching (c).

5.2.2 Fibre characterization

The quality and morphology of the fabricated optical fibre was inspected by means of a Nikon ECLIPSE E 50i microscope. An optical micrograph of a section of the fibre is shown in figure 5.7, where the triple glass structure, featuring the Nd^{3+}-doped glass in the centre, is clearly evident. The damaged area of the outer cladding in the upper part of the picture, it is due to pressure applied by the diamond wedge scribe used for the fibre facet cleaving.

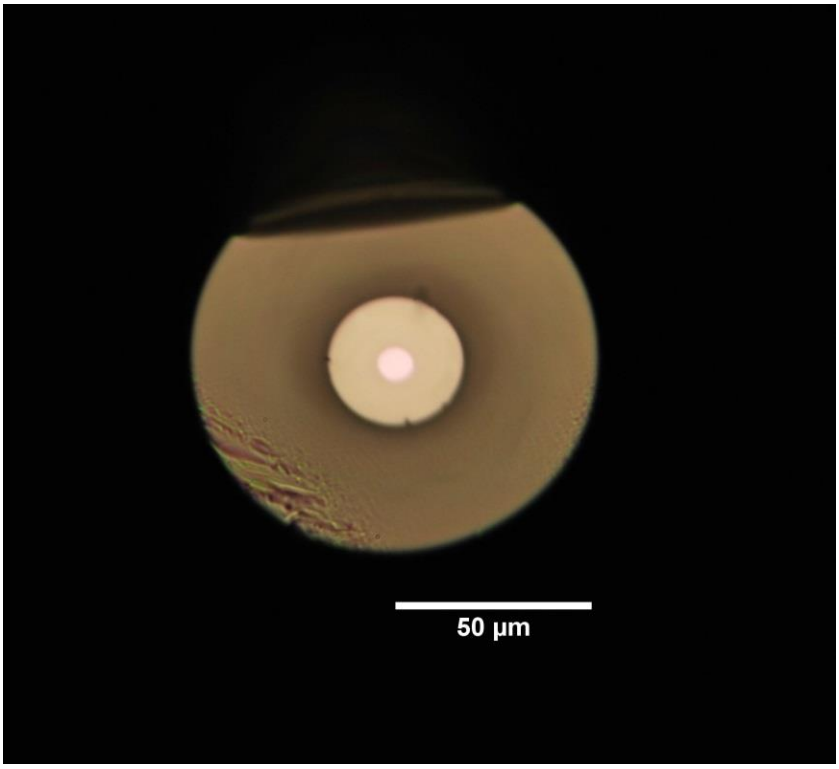

Figure 5.7. Optical microscopy image of the Nd^{3+}-doped DC optical fibre.

No bubbles were observed at the interfaces between different glasses in the analysed fibre section, but some defects at the interface between the two claddings were evident. These defects seemed to be crystalline formations, but a following analysis with X-ray diffraction excluded the presence of crystals in the glass. Further investigations seemed to indicate that the defects could be related to the conditions and materials used during the polishing phase of the tubes external surfaces. The problem is at the moment still under investigation.

The near-field image of the active fibre was measured in order to evaluate the guiding properties of the fibre. Figure 5.8 shows the near field micrograph of the fibre end face at 980 nm. It can be observed that the light is practically completely confined inside the core. A slightly diffused area can barely be seen inside the inner cladding. This fact ensures that the fibre is able to guide light and this confirms that the defects are located mainly at the inner/outer cladding interfaces, without consequences on the guiding inside the core.

Fibre losses were measured by cut-back technique using a length of about 300 cm with a single mode fibre pigtailed laser diode source at 1300 nm. The laser was butt-coupled to one of the active fibre ends. The attenuation value was calculated through linear least square fitting of the experimental data as reported in Figure 5.9. The obtained attenuation coefficient was 5.7 dB/m. Experimental measurements showed small variations with respect to the fitted slope that can be due to either experimental errors or the presence of scattering and absorption particles.

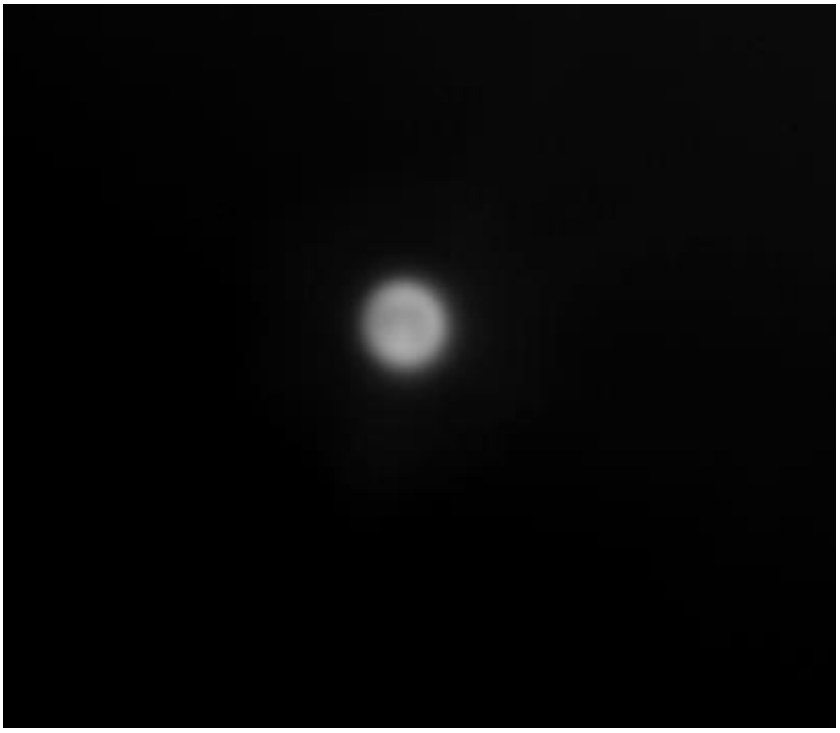

Figure 5.8. Near field image of the Nd^{3+}-doped DC optical fibre.

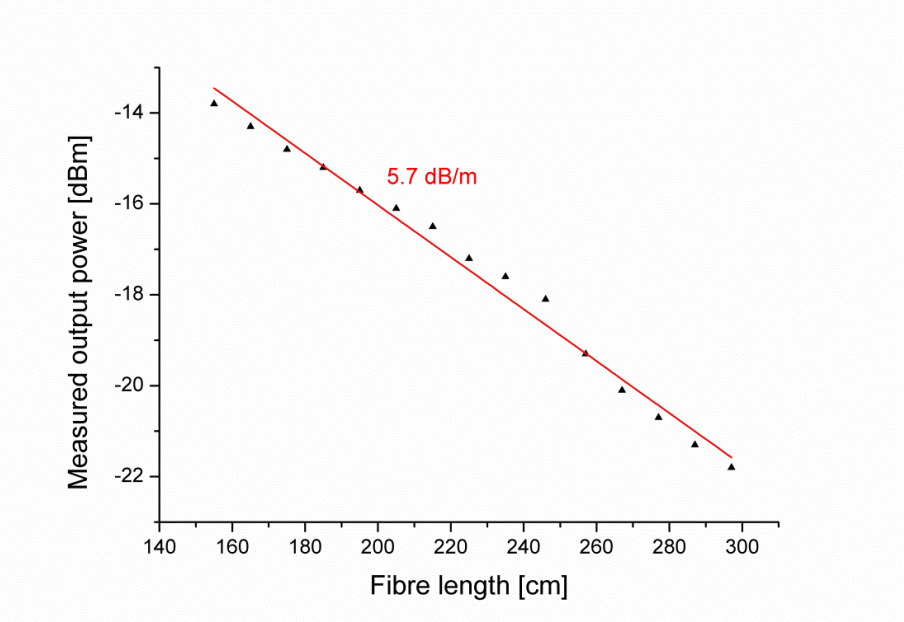

Figure 5.9. Attenuation coefficient measured on Nd^{3+} phosphate glass fibre obtained by exciting at 1300 nm. After fitting the curve a mean value of 5.7 dB/m was found.

5.3 Fibre laser design

In order to optimize Nd^{3+}-doped fibre laser design, a numerical analysis of the laser was performed using a fibre laser simulator developed in-house. The software was originally designed for optical fibre amplifier, but later it was upgraded in order to model also fibre laser. The developed model takes into account the most important phenomena governing the laser emission from solid-state laser where the active medium is formed by a RE doped host and it is based on the simultaneous solution of the rate equations governing the absorption and emission of photons by the RE ions and the signal and pump propagation equations. The correctness of implementation of the developed model was assessed through comparisons with previously reported fibre laser.

Figure 5.10 shows the graphical user interface (GUI) of the software that allows setting all the requested parameters for the laser design.

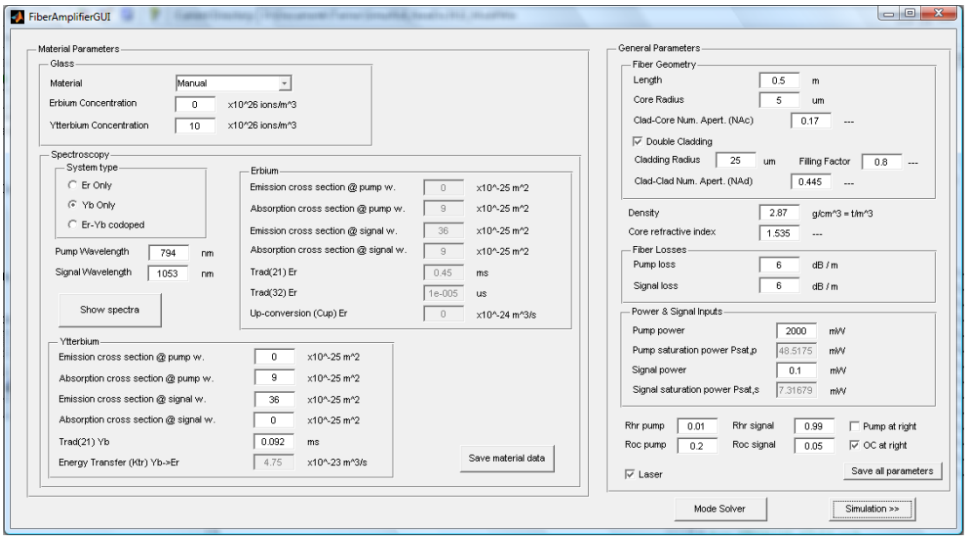

Figure 5.10. Graphical user interface of the fibre laser simulator developed in-house.

Using the software, design maps of the laser can be generated. They allow summarizing in one plot the existing relationship of the most pertinent design parameters. Figure 5.11 reports a map generated by setting the fibre geometrical parameters such as core and clad dimensions and numerical apertures, along with the amount of pump power available. This map shows the laser output power as a function of the active medium length and neodymium concentration. Not unique solution exists but instead several output power–length–concentration triplets. From figure 5.10 it can be observed that with the concentration level used for manufacturing the core glass ($2.4 \cdot 10^{20}$ Nd^{3+}/cm^3), an output power around 0.6 W could be obtained using 10 cm of active fibre, thus obtaining a 30% optical conversion efficiency with respect to the launched pump power. Further increase of fibre length will not result in higher output power.

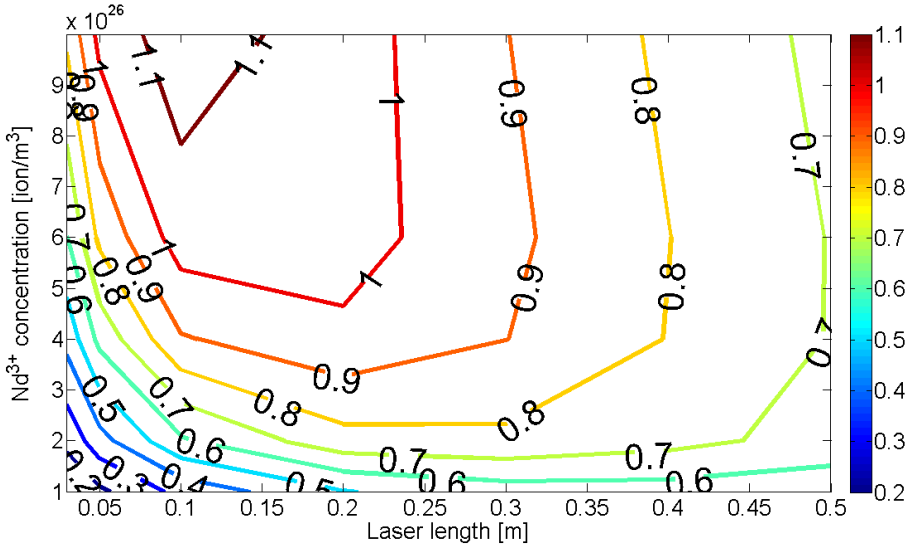

Figure 5.11. Design map for launched pump power *Pp*= 2W, NAcore = 0.18, NAcladding=0.37, core radius=5µm, inner cladding radius =25µm.

5.4 Optical fibre laser demonstration

5.4.1 Experimental details

A 9 cm long section of the fabricated Nd^{3+}-doped phosphate glass fibre was used to demonstrate laser emission at the wavelength around 1 µm. Figure 5.12 reports a schematic of the experimental setup.

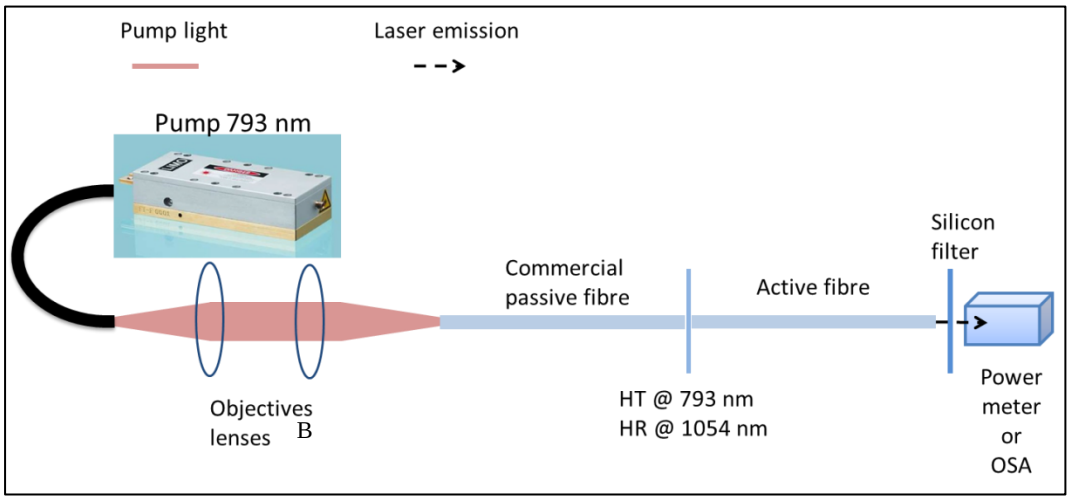

Figure 5.12. Schematic diagram of the Nd^{3+}-doped phosphate fibre laser setup.

The active fibre was cladding pumped at the wavelength of 793 nm using laser light emitted by a multimode fibre pigtailed laser diode (LIMO35-F200-DL793-EX1360). The pump laser peak wavelength is not exactly centred on Nd^{3+} absorption peak ($^4I_{9/2} \rightarrow {}^2H_{9/2} + {}^4F_{5/2}$), so not all the pump power was actually available for pumping. Considering the dimension and NA of the LIMO fibre pigtailed in order to launch as much power as possible in the active fibre and to have an easier alignment process, the pump light was first coupled through objectives lenses in a commercial passive fibre with dimension similar to the Nd^{3+}-doped fibre (see table 5.3 for details on the components used). The passive fibre was then butt coupled to the active fibre.

Table 5.3. Details of the components used for the Nd^{3+}-doped fibre laser demonstration.

Component	Description	Relevant parameters
Pump laser	LIMO LIMO35-F200-DL793-EX1360	λ = 793 nm $P_{out\ max}$ = 35 W
Pump laser output fibre	LIMO-SMA905-F200-3	$Ø_{core}$ = 200 µm / $Ø_{clad}$ = 280 µm NA= 0.22
Passive fibre	Nufern, MM-S105/125-22A	$Ø_{core}$ = 105 µm / $Ø_{clad}$ = 125 µm NA = 0.22
Nd^{3+}-doped fibre		$Ø_{core}$ = 8 µm / $Ø_{clad}$ = 35 / 105 µm NA_{core} = 0.18 / NA_{clad} = 0.37
Objective lens (A)	Newport M-20X	Magnification 20X, NA = 0.4 Focal length f = 9 mm
Objective lens (B)	Newport M-40X	Magnification 40X, NA = 0.65 Focal length f = 4.5 mm
HR mirror	Altechna A-E-24	HR @ 1030÷1064 nm HT @ 400÷ 940 nm
OSA	Agilent 86140B	Max 30 dBm or 23 dBm in 10 nm
Power meter	Thorlabs PM 100 equipped with S144A InGaAs detector	800÷1700 nm 1µW÷1W

The laser cavity was formed on one side by Fresnel reflection provided by perpendicular cleaved end of the active fibre, which acts as output coupler, and at the other side by a broadband high reflector at 1020–1090 nm butt-coupled to the other end (see Fig. 5.13). The collected laser signal was sent to either a power meter or an optical spectrum analyser (OSA) for measurement. A silicon filter ensures that only laser light is sent and measured by the instruments.

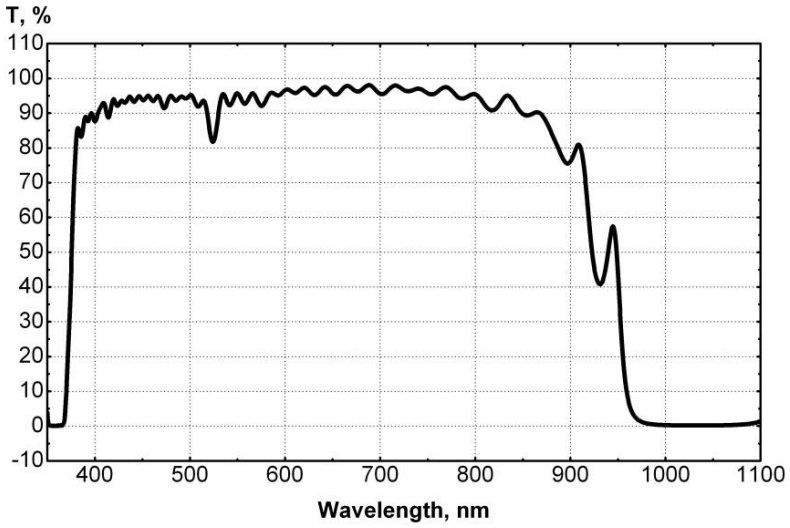

Figure 5.13. Altechna A-E-24 HR mirror transmission spectrum.

Fibre ends must be prepared to a high quality, i.e. they must be flat and perpendicular to the fibre axis. For the passive commercial fibre a standard cleaving tool was used (Fujikura CT-04B), while the active phosphate fibre was cleaved by a manual procedure using a diamond wedge scribe (Thorlabs S90W). The quality of the manual cleave was inspected under a microscope, since it was a quite unreliable operation, with approximately 50% success rate.

Due to the small dimensions of the doped fibre, very precise control over the movement of all the optical components of the setup was necessary in order to optimise the pump power coupling. For this reason all the optical elements were mounted on the following micro positioners: Thorlabs MBT616D with 50 nm of resolution and RB13M with 10 µm resolution for components with less critical positioning.

As first step of the experimental procedure, the tip of the pump laser fibre pigtail was placed in the focus of objective A. The objective B was placed at a distance of approximately 2 cm on the same optical axis. Thus the collimated pump light from objective A was focused by objective B. The tip of the passive commercial fibre was then placed in the focus of this latter objective. The correct positioning of the fibre was accomplished initially using an IR viewing card to check if light exits from the other end of the fibre, then using a power meter that measured the amount of light exiting the fibre. The positioning of each optical element was then carefully adjusted in order to maximize the measured power.

At this point the HR mirror and the active fibre were placed in the setup. The active fibre was butt coupled to the passive one and this operation was monitored by a microscope to ensure it never came in contact with the mirror face. The fluorescence light exiting the active fibre was monitored by the OSA. The positioning of the active fibre was then adjusted to maximize the output light. Once the maximum was reached, the current of the pump diode was progressively increased until a laser signal was detected on the OSA. The laser was then characterized by measuring the threshold current, the output power with respect to the pump power and the output spectrum.

In order to evaluate more accurately the amount of pump power launched into the active fibre inner cladding, and thus have a better calculation of Nd^{3+}-doped fibre laser efficiency, after the experiment, the active fibre was replaced by a phosphate single cladding passive fibre made of the same glass and with core dimension of 40 μm. The output power of this fibre was measured while increasing the launched pump power. In fact, the commercial passive fibre has a core dimension (105 μm) that is considerably higher compared to the active fibre inner cladding (35 μm), moreover also the NA are different. This means that a significant part of launched pump power was not coupled into the active fibre.

5.4.2 Results and discussion

Figure 5.14 shows the amplified spontaneous emission (ASE) of the fibre when pumped at 793 nm. The main Nd^{3+} emission peaks (see section 3.2.4) are visible.

Figure 5.15 displays the laser output power as a function of launched pump power in the active fibre, valued as explained in section 5.4.1. The experimental data (excluded

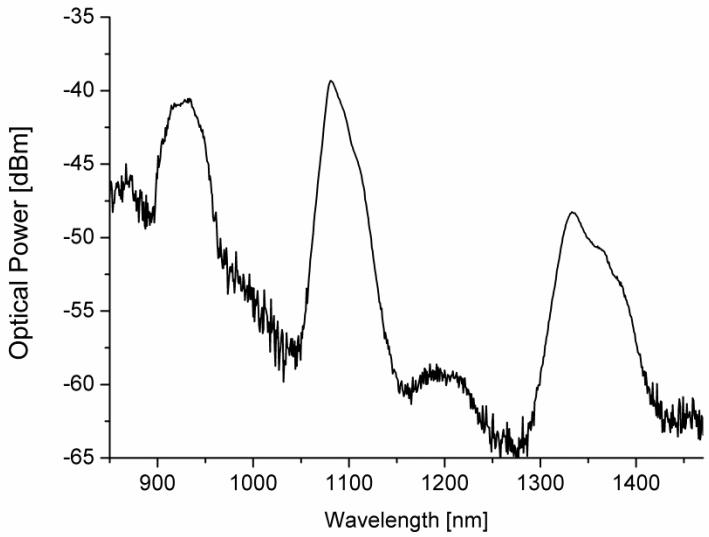

Figure 5.14. Amplified spontaneous emission of the Nd^{3+} phosphate fibre when pumped at 793 nm.

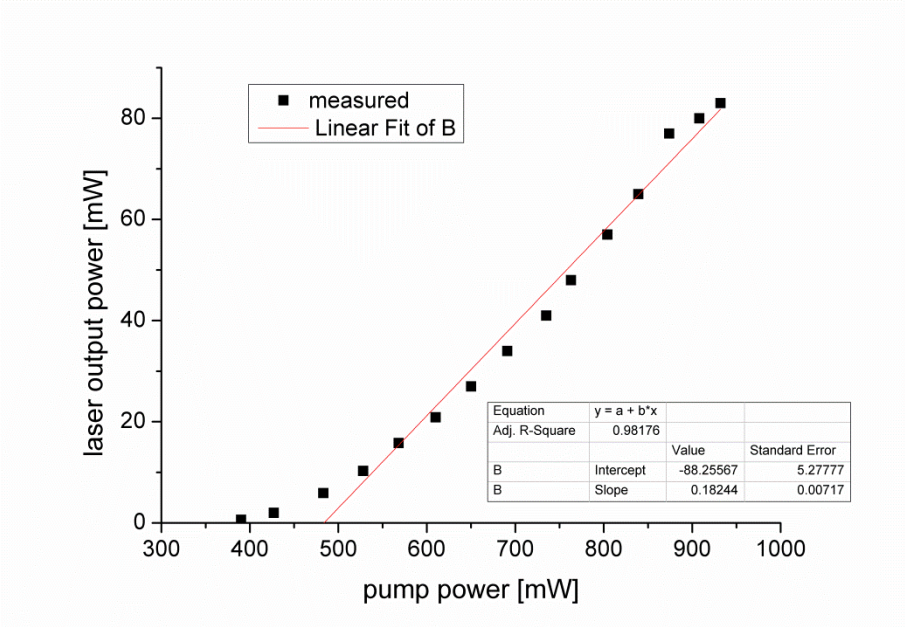

Figure 5.15. Fibre laser measured output power as a function of the launched pump power.

the first two points) were fitted by a linear fit. The calculated laser threshold, i.e. the value of launched pump power at which the fibre laser began to lase, was 483 mW. The slope efficiency, i.e. the efficiency with which the pump power above threshold was converted into laser output power, was 18%.

Figure 5.16 shows the typical spectrum of the Nd^{3+} phosphate fibre laser at the output of 40 mW. In the picture on the left a peak of the residual pump at 793 nm is noticeable. A more detailed spectrum (OSA resolution 0.2 nm) of the fibre laser at the same power level is reported in figure 5.17. The emission was centred at 1054.5 μm. The full width half maximum (FWHM) is around 1.8 nm, in line with results previously reported in Nd^{3+} phosphate glass fibre lasers [2].

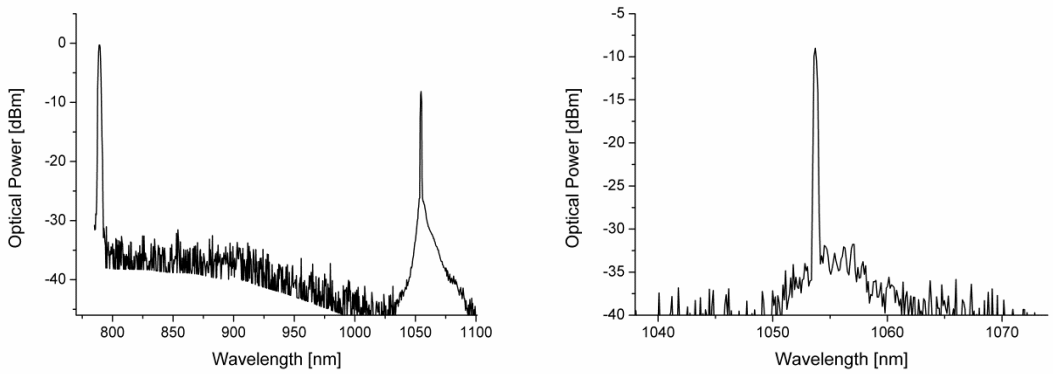

Figure 5.16. Nd^{3+} phosphate fibre laser spectrum at an output power of 40 mW. In the spectrum on the left a peak of the residual pump at 793 nm is observable.

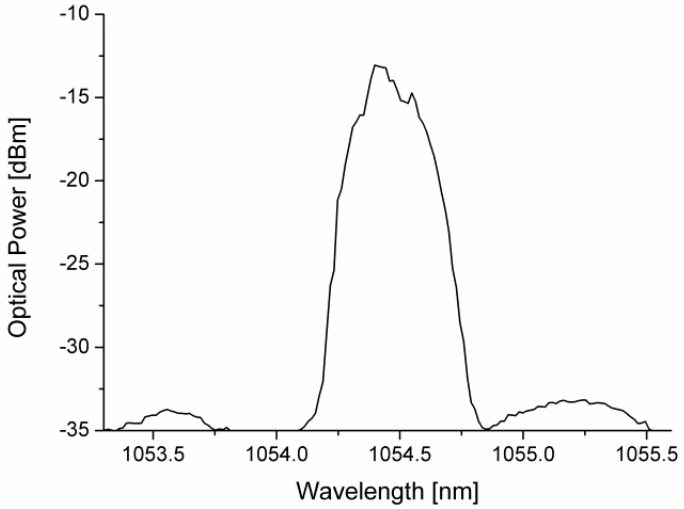

Figure 5.17. Detailed spectrum of the Nd^{3+} phosphate fibre laser an output power of 40 mW.

5.5 Conclusion and future development

Three phosphate glasses suitable for DC optical fibre fabrication were synthesized and characterized using a custom designed glass composition: the core glass, doped with 2.3 wt. % of Nd_2O_3 and two un-doped glasses with lower refractive index for the inner and outer cladding. The glasses showed great stability toward crystallization due to the presence of network intermediate (R_2O_3) and limited glass transition temperature.

The Nd^{3+}-doped core glass exhibited a strong emission at 1.06 μm when excited by a laser diode emitting at 785 nm. The lifetimes of the Nd^{3+}:$^4F_{3/2}$ was measured; the value obtained (305 ± 15 μs) was in line with previous measurements performed on the same glass system and discussed in chapter 4.

Numerical analysis of the Nd^{3+}-doped fibre lasers was performed in order to optimize laser design. With the concentration level used for manufacturing the core glass ($2.4 \cdot 10^{20}$ Nd^{3+} ions/cm^3) and the numerical aperture obtained from our glasses, an output power around 0.6 W could be obtained using 10 cm of active fibre (10/50/125 μm), thus obtaining a 30% optical conversion efficiency with respect to the launched pump power.

A Nd^{3+} doped DC optical fibre based on the developed glass host composition was successfully drawn and characterized with the dimension of 8/35/125 μm. The fabricated fibre was free from air bubbles but presented some defects at the interface between inner and outer cladding. It was assessed that the defects were not crystals, but the reason of their formation is still under investigation.

Guiding properties inside the core was verified by near field measurement, thus confirming that the defects are located mainly at less critical interface between inner and outer cladding. The measured attenuation coefficient was 5.7 dB/m.

A CW cladding pumped fibre laser based on 9 cm of fabricated Nd^{3+}-doped optical fibre emitting at 1054.5 μm was demonstrated, with a slope efficiency of 18% with respect to the launched pump power. A maximum output power of 85 mW was obtained for a launched pump power of 930 mW, thus obtaining an optical conversion efficiency of 9.1%.

The obtained optical efficiency (9.1%) is relatively low compared to the one (30%) foreseen from the laser design. This result could be explained by several factors. First

of all the fibre dimensions used for laser design where slightly bigger than the real ones: 10/50/125 μm against 8/35/125 μm. Moreover the fabricated fibre showed some defects at the interface between the two claddings, which certainly affected the confinement of the pump light into the inner cladding. At last mechanical tolerances in the positioning of the flexure stages could have caused imperfect alignment between the optical elements forming the laser cavity.

In order to optimize laser output emission from the Nd^{3+} doped fibre, additional work will be carried out in order to address the problem of defects formation at the interface between the two cladding during fibre drawing.

Further work on spliceability of phosphate fibres to commercial silica based fibre and fibre components, will allow the realization of the whole laser resonator in fibre (*all fibre setup*) avoiding the use of free-space optics, with their stringent requirements for precise alignment.

REFERENCES

[1] Lousteau, J., et al., "Er^{3+} and Ce^{3+} co-doped tellurite optical fiber for lasers and amplifiers in the near infrared wavelength region: fabrication, optical characterization and prospects," IEEE Photon. J., vol. 4 n. 1, pp. 194-204, 2012.

[2] G. Zhang, et al., "Efficient generation of watt-level output from short-length Nd-doped phosphate fibre lasers," IEEE Photon. Technol. Lett. 23, pp. 350–352, 2011.

Chapter 6

Solar pumped laser

If we consider the energy level diagram of the Nd^{3+} ion (see Fig. 3.7), we can observe that several absorption bands are located in the visible and near IR. This has allowed in the first Nd^{3+}-doped laser [1] the use of flashlamps as pumping sources. More recently, with the increasing availability of laser diodes at the requested wavelength, a more efficient and compact pumping scheme has been realized using laser diodes. But for Nd^{3+} ion, also a more unconventional pumping solution is possible: the pumping by concentrated solar light. In fact Nd^{3+} ion presents very strong absorption bands where sun spectral density is almost maximum.

After a brief introduction about solar radiation, in the first part of the chapter the concept of solar pumped laser (SPL) is introduced along with its potential applications on the earth and in space. Then the long history of SPL is briefly reviewed in order to present the state of the art in this research field.

In the following, a new technological approach to SPL, based on fibre laser technology is presented and its key advantages over conventional solid state lasers based on bulk rods or disk active media is discussed.

With the aim to realize a Nd^{3+}-doped solar pumped fiber laser, based on the developed phosphate glass host presented in chapter 4, a preliminary study of active material performances for SPL application was conducted. In order to exploit the unabsorbed solar energy by Nd^{3+} ions, Eu^{3+} co-doping of Nd^{3+}-doped phosphate glasses was also investigated to assess a potential increase in the overall pump power

conversion efficiency. Experimental results of this active material study are reported in last part of the chapter.

6.1 Solar radiation introduction

An important parameter about solar radiation is the solar constant, the total radiation energy received from the sun per unit of time per unit of area on a theoretical surface perpendicular to the sun's rays and at Earth's mean distance from the sun. The solar constant varies by ± 3.4% on annual basis, but the value of 1.353 kW/m^2 is often found in literature [2].

As solar radiation passes through the atmosphere, it is attenuated by about 30% due to Rayleigh scattering by molecules, Mie scattering by aerosols and dust particles and absorption by atmospheric gases such as oxygen, ozone, water vapour and carbon dioxide. After scattering and absorption followed by partial re-radiation into space, approximately 1 kW/m^2 reaches the ground under clear weather conditions. However this amount varies significantly from one point to another due to atmospheric conditions and position of the Earth with respect to the sun.

In addition to the total energy in the solar spectrum (i.e. the solar constant), it is useful to know the spectral distribution of solar the radiation. Figure 6.1 shows different solar spectra [2] defined as follow:

- Extraterrestrial Radiation: solar spectrum at top of atmosphere at mean Earth-sun distance.
- Global Tilt : spectral radiation from solar disk plus sky diffuse and diffuse reflected from ground on south facing surface tilted 37°C from horizontal. The integrated power of this radiation is about 1 kW/m^2.
- Direct: Direct Normal Irradiance Nearly parallel (0.5 deg divergent cone) radiation on surface with surface normal tracking (pointing to) the sun, excluding scattered sky and reflected ground radiation.
- Circumsolar : spectral irradiance within +/- 2.5 degree (5 degree diameter) field of view centred on the 0.5 deg diameter solar disk, but excluding the radiation from the disk.

The direct plus circumsolar spectrum has an integrated power density of 900 W/m^2.

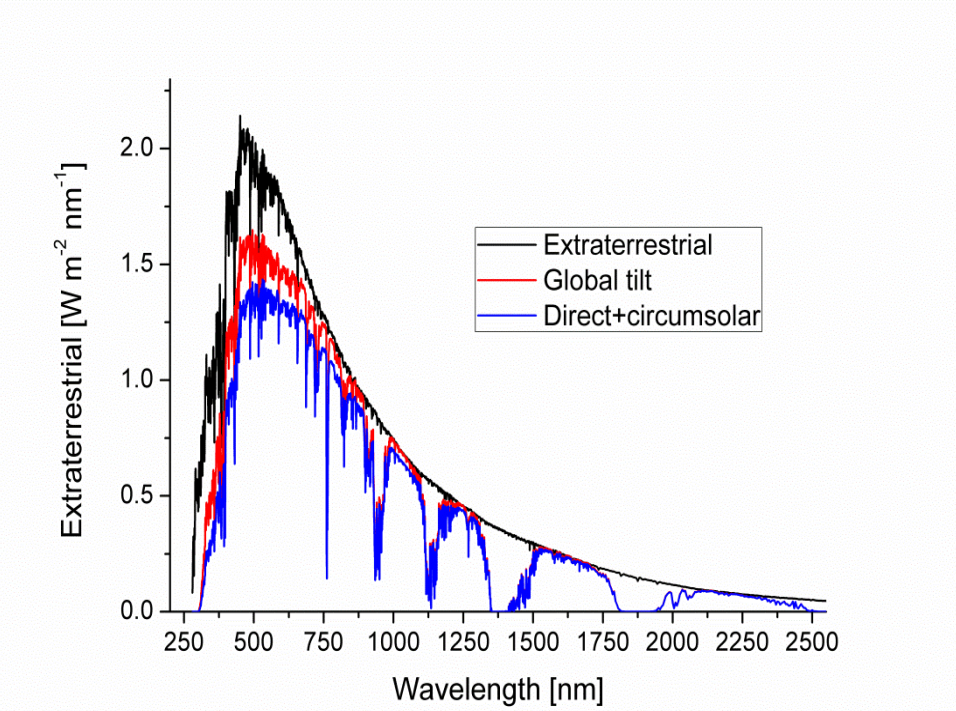

Figure 6.1. In black: solar spectrum at top of atmosphere (extraterrestrial). In red: solar spectral radiation from solar disk plus sky diffuse and diffuse reflected from ground (global tilt). In blue: direct radiation from the sun plus the circumsolar component in a disk 2.5 degrees around the sun.

6.2 Solar pumped laser concept and applications

On the earth our primary source of clean, renewable, abundant and free energy is the sun. More energy from sunlight reaches the Earth in one hour ($4.3 \cdot 10^{20}$ J) than all the energy consumed on the planet in a year ($4.1 \cdot 10^{20}$ J) [4]. Thus, considering the world increasing energy demand, interest on new way of solar energy harvesting is rising. In this framework, a concept that has gained an ever-increasing importance in recent years [5] is the SPL, a device that converts broad-band solar radiation cantered in the visible into coherent and narrow-band laser radiation in the near IR (see Fig. 6.2).

Compared to the traditional use of sunlight for producing electricity through photovoltaic cells, which in turn produces the pump signal through pump diodes, direct solar pumping of solid state lasers avoids two energy conversion steps. This approach is therefore potentially more efficient, simpler (due to the complete elimination of the electrical power generation system and power conditioning unit) and more reliable [6] and in principle it would also provide a limitless operative lifetime.

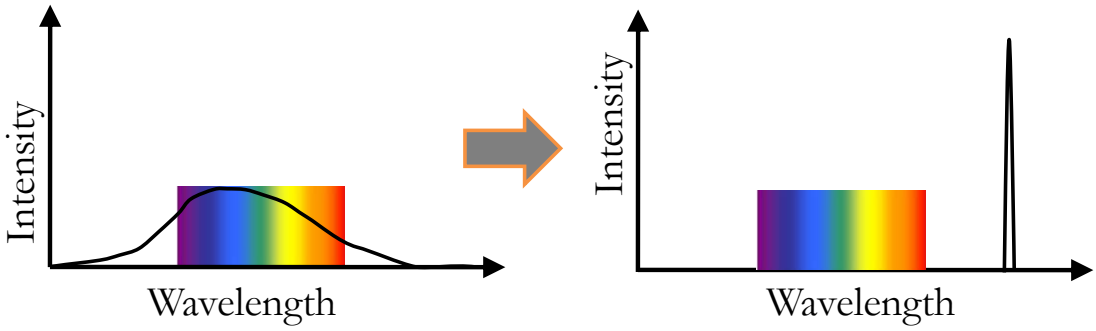

Figure 6.2. Schematic representation of a SPL concept. Broad-band and incoherent solar radiation centred in the visible (on the left) is converted into coherent and narrow-band laser radiation in near IR (on the right).

Reasonable cost diode pumped solid state lasers have efficiency around 30-40% with respect to the electric input power, commercial photovoltaic cells have an efficiency ranging between 14-19%, but considering conversion losses and deterioration of the cells, a net efficiency of 10% to 13% seems to be realistic. Combining these values of efficiency stated above, we obtain an overall efficiency of about 3-5.2% [4]. Using direct solar radiation into laser, net conversion efficiency of 4.3% have been already reported [4] and it is noteworthy to observe that much less consideration has been devoted to SPL research and thus this technology is currently much less mature.

6.2.1 SPL applications in space

Numerous present and future missions include instruments for spatial exploration based on lasers for monitoring, sensing or measuring (see table 6.1). The range of applications of these systems is broad, and, besides telemetry, it encompasses altimetry for the investigation of the topography of the planetary surface, on-site spectrometric analysis of soil samples, LIDAR (light detection and ranging) applications for atmospheric investigations, precision interferometry and optical communications.

Beyond these mainstream applications, novel concepts for laser employment in space have been proposed: wireless energy transmission from space to Earth or to space vehicles [7], deep space communications [8], laser propulsion [9] and Near Earth Objects (NEO) deflection [10].

Table 6.1. Laser systems for space applications [11].

Category	Application	Instrument / Mission
optical telemetry	metrology between Earth and satellites	n.a.
	metrology between satellites	LISA
	formation flying	PROBA-3
altimetry	on Earth	IceSats (Nasa)
	for planetary missions	BELA / BepiColombo
		LALT / Kaguya (Jaxa)
		EJSM-Laplace
optical communication	communications between spacecraft	SILEX programme
		TerraSAR-X and NFIRE
		Alphasat and Sentinel1+2
	communications between spacecraft and Earth	ARTEMIS to Optical Ground Station
LIDAR	wind Doppler LIDAR	ADM Aelous
	backscatter LIDAR	ATLID / EarthCare
		CALIPSO / CloudSat (Nasa)
	differential absorption LIDAR	A-SCOPE
optical sensors	structure and payload monitoring	*FOSAT project*
	propulsion system monitoring	Proba II
	attitude and orbit control	Sloshsat-FLEVO

Although the numerous applications of lasers require different architectures (laser material, resonator design, pump delivery) and working parameters (CW output power, pulse energy, spectral properties, stability), almost all space lasers are based on the same technology: diode pumped solid state lasers and among them one of the most common are lasers based on Nd^{3+}-doped YAG crystal, due to the technology maturity, robustness and performance of this laser.

However, despite the broad range of possible laser applications in space, owing to the use of a diode based pump source, current Nd^{3+}-doped solid state laser technology presents several limitations in terms of lifetime, electricity generation, power consumption, mass, operating temperatures, mechanical stability, resistance to ionising radiation and reliability. All these drawbacks reduce the effective laser employment in

space and limit technical and economic feasibility of missions planned to last many years.

SPL is a very promising concept able to overcome current laser technology for its intrinsic advantages that make it particularly attractive for space applications where long lifetimes are required and where efficiency, compactness and reliability are critical.

Moreover the use of the solar laser in outer space has the advantages to use the whole solar energy avoiding the attenuation, the absorption and the reflection through the earth's atmosphere. Those physical actions decrease the useful part of the solar radiation needed to overcome the threshold pumping power of the laser medium.

6.2.2 SPL applications on the earth

On the earth, high power SPL could be employed in industrial applications like material welding, soldering, cutting and hardening, especially in the field of the micro-mechanics. This can be realized in a factory where one laser produces the radiation which is delivered via glass fibres to the application sites.

Another interesting application of SPL is to activate particular chemical reactions that require very high temperatures to occur and thus require a lot of electricity. An example of this application has been proposed in Japan in 2006 [12] for converting the magnesium oxide, MgO, of sea water into pure magnesium, simply by heating it to temperatures of around 4000° K to induce a reduction reaction (see Fig. 6.3). Such high temperatures aren't possible simply by focusing natural sunlight alone, but it is indeed possible with the focused output from a SPL. The produced pure Mg can enter a cycle in which it

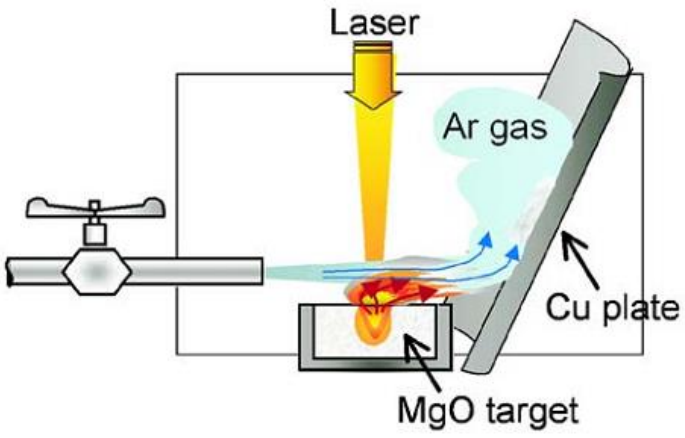

Figure 6.3. Schematic diagram of SPL ablation of a MgO target with argon gas flow [11].

reacts with water and produces hydrogen, magnesium oxide, and releases a large amount of energy. Such energy and hydrogen are used for turbine, reciprocal engine, fuel cell and so on. The only waste of the reaction is MgO that can be recycled by the SPL for using once again. The rationale behind this research is the possibility to store pure Mg as a reservoir of energy that can be used when needed, for example in cloudy days.

Another possible terrestrial application could be the pollutant control and analysis of samples with a mobile measuring system that can be used in remote location where electricity is not available.

SPL can also be used for conversion to electricity, but in a different way with respect to the conventional use of photovoltaic panel (see Fig. 6.4). The broadband solar radiation can be firstly converted to narrowband laser radiation with suitable photon energy. This energy must be equal to the gap of the semiconductor used for the realization of the photovoltaic panel. In this way, the conversion could be in principle more efficient since all the photons will be absorbed by the semiconductor and problems related to heat generation will be overcome.

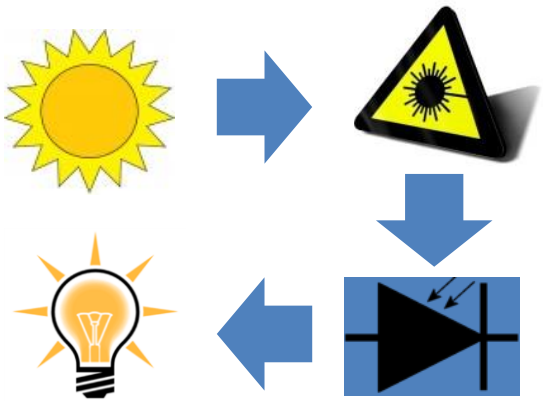

Figure 6.4. Schematic representation of electricity production system using SPL in combination with photovoltaic cells.

6.3 SPL state of the art

The very first SPL was obtained using Dy^{3+} ions as active element in a CaF_2 matrix [13]. Soon after, Young [14] demonstrated a sun pumped continuous wave Nd^{3+}:YAG laser, with an output power of 1 W using a modified Cassegrain sun-tracking telescope consisting of a 61 cm diameter paraboloidal primary mirror collector. In the same work 1.25 W of output power were obtained in 7 ms pulses from an uncooled, sun-pumped, neodymium-doped glass rod. From then on, the choice of Nd^{3+} as emitting ion became

practically a standard because it presents a very strong absorption band where sun spectral density is almost maximum.

Several authors have reported on the demonstration of sunlight pumped lasers. Among them, the highest output power of 500 W was achieved in 1993 by Krupkin et al. [15] by side-pumping a Nd-YAG rod with light concentrated from a 660 m^2 collecting mirror system. However, in this work the collection efficiency, i.e. the ratio of laser power to primary mirror area, was very low, around 0.76 W/m^2.

In 2003 Lando et al [6] reported on a solar side-pumped Nd-YAG laser experiment exhibiting a record collection efficiency of 6.7 W/m^2. Before this work solar facility were usually multipurpose and consisted of over-dimensioned parabolic mirrors, which resulted in small laser output with respect to the solar light collecting area. On the contrary, in this experiment, the laser facility was specifically designed for SPL experiments, with the collection efficiency and laser rod dimensions considered to be important design goals.

In recent years a further increase of solar laser power efficiency was obtained using an alternative solar power collection means, i.e. a Fresnel lens tracking automatically the sun trajectory [16,17], and by using as active medium a chromium (Cr^{3+}) co-doped Nd^{3+}:YAG ceramics in order to enhance the absorption of solar radiation [4].

Concerning the idea of a solar pumped fibre laser, this was proposed for the first time in 1997 [18] and recently the first realization under natural sunlight has been reported [19]. However in this work the use of an end-pumping configuration results in a very low output power of less than 1 mW. Moreover the chosen host material, fluoride glass, suffers from poor chemical durability and temperature stability and require stringent manufacturing process in order to avoid crystallization.

6.4 A new technological approach

Despite the long history of the research on SPL as novel renewable energy source, in order to spread this technology worldwide, reliability, cost/performance and optical-to-optical conversion efficiency of the system must still be improved considerably. We believe that this can be achieved with a new technological approach based on fibre laser technology, a mature and well spread technology with unmatched performance, especially in terms of beam management and quality [20].

Optical fibre lasers have several key advantages over conventional bulk solid state laser:

- optical fibres possess outstanding heat-dissipating capability thanks to their high surface-to-volume ratio. By contrast, in the case of bulk laser thermal effects can degrade the beam quality, leading for example to thermal lensing effects, which could lead eventually to fractures in the active medium rod. As a consequence, highly efficient and thus costly cooling systems to avoid "fatal" heat loads required for bulk solid state laser are not required when using fibres.
- The use of an optical fibre configuration as active medium of the solar laser will exploit the benefit of the optical confinement provided by a waveguide structure resulting in a low threshold and an high optical conversion efficiency.
- Fibre lasers can easily exhibit a diffraction-limited beam quality that allows strong focusing and maximizes the output intensity.
- Fibre is a thin and flexible device that allow a flexible remote delivery.
- Another key advantage of fibre technology is the possibility of developing the whole laser resonator in fibre (all-fibre setup) so light is totally confined within the core-cladding structure and thus completely shielded from the environment. Moreover this solution avoids the use of free-space optics with their stringent requirements for precise alignment, which can be critical in some applications, like space missions, in presence of vibrations or large temperature variations.

Moreover, the new technological approach is extremely versatile and could be customized to suit the different laser applications in terms of output power, beam quality and dimension, spectral properties, output stability, etc. Also a pulsed regime, requested in many applications, can be achieved by a technique known as passive Q-switching, i.e. a method that does not require drivers and electrical power supply, thus making it a simple and reliable device. Till now, passive Q- switching of Nd^{3+}:YAG lasers pumped by either non-solar or solar light has been successfully obtained using a Cr^{4+}:YAG crystal saturable absorber [21,22]. A similar approach in fibre configuration will allow the realization of an all fibre pulsed SPL, eliminating the use of optical discrete components and thus resulting in higher laser reliability.

Our proposal for an innovative SPL, is the development of a Nd^{3+}-doped side pumped fibre laser made by the engineered phosphate glass material presented in chapter 4.

Phosphate glass system (see chapter 1) presents features that makes it a suitable host material for compact high-power and single-frequency fibre lasers: a large glass formation region, a high solubility for rare earth oxides, good thermo-mechanical and chemical properties and no evidence of photodarkening even at high population inversion [23].

Concerning the doping ion, the choice of Nd^{3+} as has been driven by the overlapping ratio between the standard solar spectrum and the ion absorption bands that was calculated to be 0.14 [24]. Moreover Nd^{3+} is one of the most important RE activators for crystalline and bulk glass lasers because of the power and efficiency available from the transition around 1064 nm (see section 3.2.4). A Nd^{3+}-doped laser operated at this wavelength behaves like a four-level laser system, so a positive internal gain is possible even for very small pump power and, therefore, a very low threshold can be achieved.

Another novelty of the proposed solar laser system is the side pumping of the optical fibre by concentrated solar light. An optical fibre is very thin and flexible, thus it can be coiled in a desired area. In this way a perfect match between solar concentrator image in the focal plan and pumping absorbing area could be achieved thus resulting in an higher conversion efficiency (see Fig. 6.5).

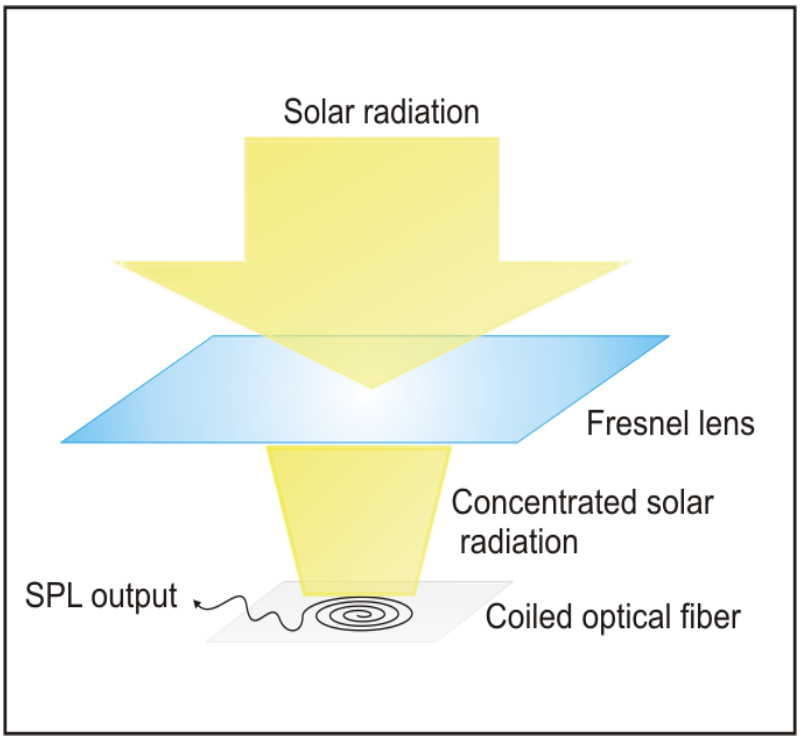

Figure 6.5. Schematic of a side pumped solar pumped laser concept.

6.5 Nd^{3+}-doped phosphate glass as active material for SPL

We used for this study Nd^{3+}-doped phosphate glass samples Nd1÷Nd6 whose composition and synthesis was described in section 4.1. For measurement results of the major physical, thermal and optical properties of the glasses we remand the reader to chapter 4, in the following we will report only some additional characterization specific of SPL application.

6.5.1 Absorption spectroscopy

In order to assess the possibility to pump Nd^{3+}-doped phosphate glasses by solar radiation, absorption cross section calculated from UV–VIS–NIR spectroscopy (see section 4.3.3) was compared to solar spectral irradiance.

Figure 6.6 reports the absorption cross-section obtained for glass sample Nd04, with Nd^{3+} levels labelled considering absorption from the ground state $^4I_{9/2}$, and direct solar spectral irradiance at sea level. From the picture it can be observed that Nd^{3+} ion

presents several strong absorption bands in the visible where the sun has its maximum emission, making it a suitable doping ion for the development of a SPL.

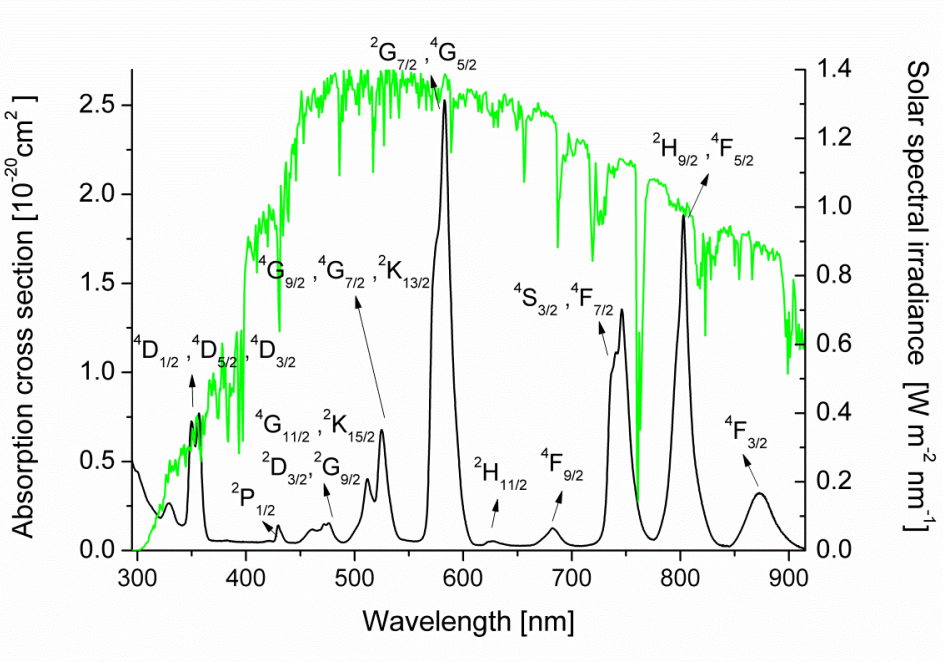

Figure 6.6. Absorption cross-section spectrum for sample Nd04. The main Nd^{3+} levels are labelled, considering absorption from the ground state $^4I_{9/2}$. In green, for reference, the direct solar spectral irradiance at sea level is reported (ASTM G173-03) .

6.5.2 Emission spectroscopy

In order to study the fluorescence of Nd^{3+}-doped phosphate glasses under solar radiation, emission spectroscopy was performed on glass samples using as excitation source a broadband visible light (Supercontinuum source Coheras SuperK Extreme) that simulates solar radiation.

The setup used for the measurements is described in chapter 4.2.6.

Figure 6.7 illustrates the measured fluorescence spectrum obtained from glass Nd05 (6 mol% Nd^{3+} concentration) in the wavelength range 1010÷1110 nm. For comparison the picture reports also the fluorescence spectrum obtained from the sample under excitation with a monochromatic light at 795 nm emitted by a single mode fibre pigtailed laser diode (Qphotonics QFLD-795-100S).

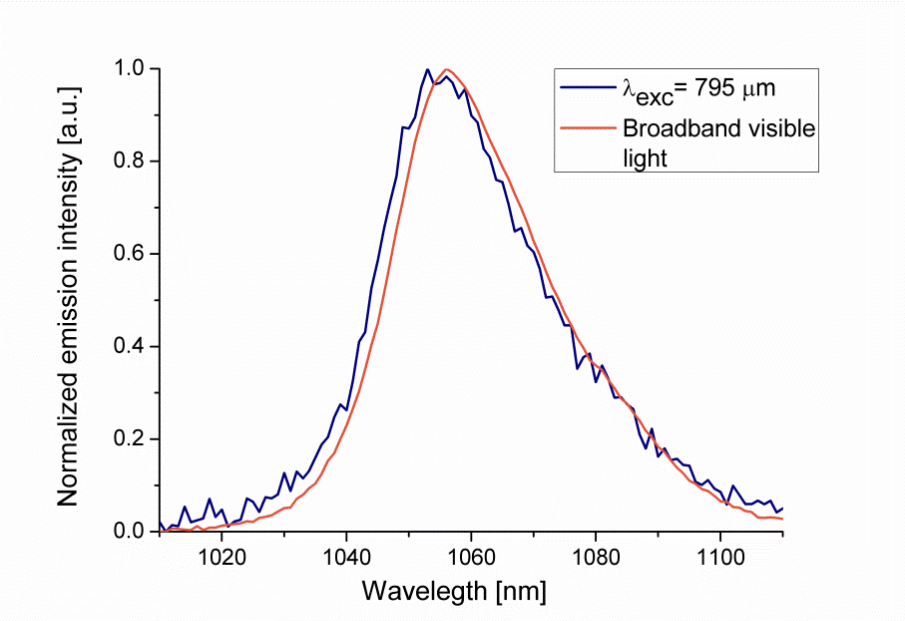

Figure 6.7. Emission spectra of the $^4F_{3/2} \rightarrow {}^4I^{11/2}$ transition of Nd^{3+} upon 795 nm excitation and broadband visible light for the sample Nd05 (6 mol% Nd^{3+} concentration).

The broad 1.06 μm emission is assigned to the $^4F_{3/2} \rightarrow {}^4I_{11/2}$ transition. Similar spectra were recorded for the other manufactured glass samples.

It is important to underline that the spectra obtained with the two different excitation sources were the same, in spite of the distinct excitation paths. This observation demonstrates the validity of using the single frequency source as excitation light for characterizing our samples and then extrapolate those results to the case of a polychromatic pump source, like the sun.

Therefore, concerning the lifetime measurements and concentration quenching effect, all the results reported in section 4.3.5, obtained under excitation by a monochromatic light, could be extended to the case of solar pumping of the active glasses.

6.5.3 Test in a real solar concentrator system

Assessment of Nd^{3+}-doped phosphate glass performance, in form of a rod, was also carried out in a real solar concentrator system located in Portugal.

Figure 6.8 reports a picture of the solar concentrator facility and a detailed diagram of the laser head, based in this case on a Nd:YAG rod active material [17].

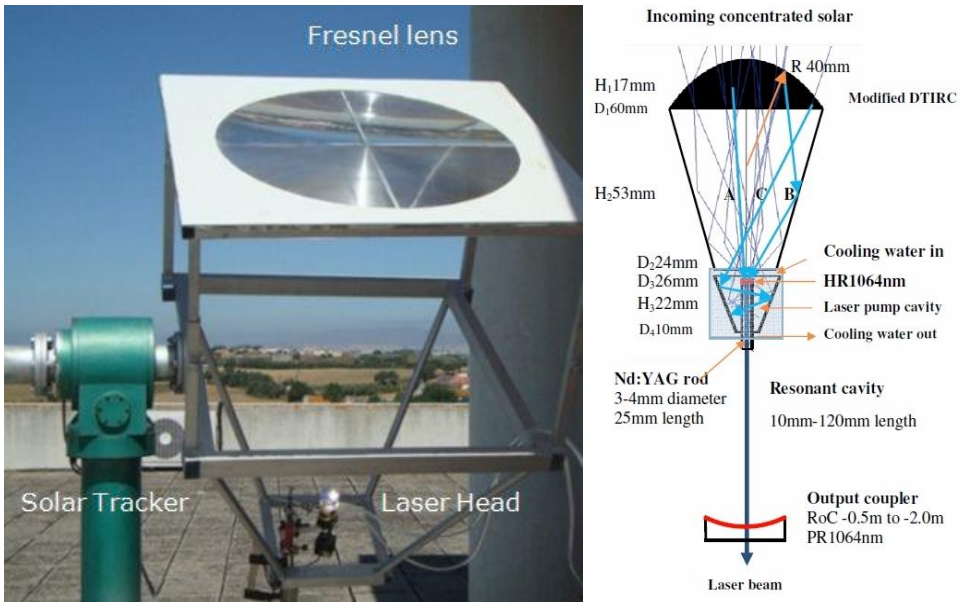

Figure 6.8. On the left: The solar-pumped laser system with a 0.9 m diameter Fresnel lens and a laser head positioned in its focal zone. On the right: a detailed view of the laser head, in this case based on a Nd:YAG rod active material. See for details [16].

The system is composed of a 0.9 m diameter Fresnel lens, made of Polymethyl Methacrylate (PMMA) material, mounted on a two-axis solar tracker that follows automatically the sun's movement. In order to couple efficiently the light distributed in the lens focal zone to a thin rod, a further concentration stage is required. This is obtained by using a dielectric totally internally reflecting concentrator (DTIRC), with a large curved input face and a small planar output face, coupled to the conical pumping cavity where the 3-4 mm diameter active material is mounted. The system is water cooled and this water also plays a crucial role in guaranteeing efficient light coupling between the output end of the DTIRC and the rod. Efficient absorption of pump radiation is achieved through both direct end-pumping and multi-pass side-pumping within the cavity.

In order to test our active material in the described solar concentrator system, rods of Nd^{3+}-doped phosphate glasses were fabricated with two different diameters, 3 and 4 mm. The glasses were doped with a concentration of 0.5% Nd_2O_3 corresponding to $1.32 \cdot 10^{20}$ ions/cm^3.

Glass was fabricated using the method described in chapter 4.1. The melt was cast in a pre-heated cylindrical brass mould and then a stage of stretching in the drawing tower

was performed in order to obtain the requested diameters of 3 and 4 mm. The cylindrical doped glass was then cut using the cutter Hitech Europe C100 equipped with a diamond blade in order to obtain rods 25 mm long. The rod ends were then lapped and polished to optical smoothness.

In order to form the laser cavity in the solar system facility, the rods were required to have one end coated by an high reflectivity (HR) layer at laser wavelength and an high transmission (T) of visible light. The deposition was performed by an external laboratory using an RF sputtering. The coating had the following characteristic: HR-Coating Reflectivity R > 99.8% @ 1064nm and T >95% @ 808nm.

Figure 6.9 shows some of the Nd^{3+}-doped phosphate glass rods manufactured for the test.

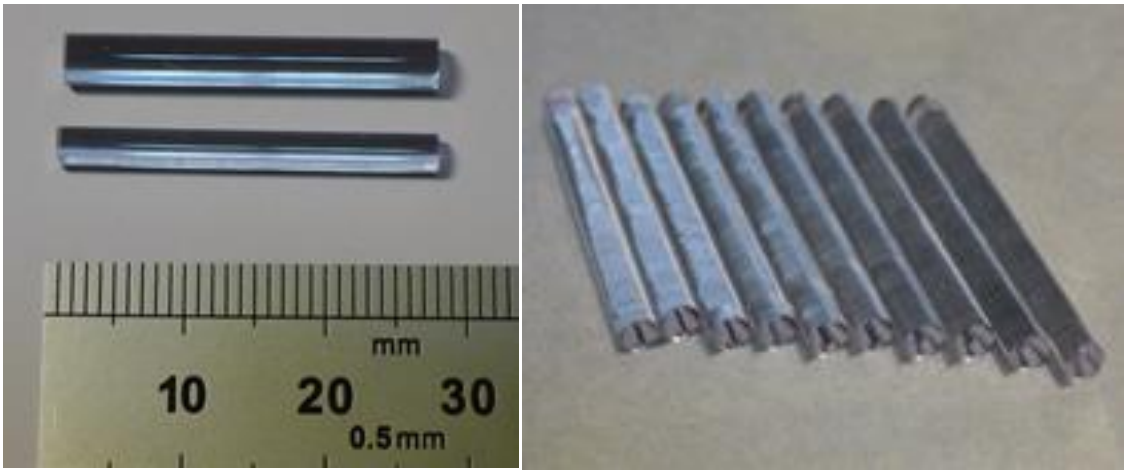

Figura 6.9. Nd^{3+}-doped phosphate glass rods manufactured for testing the active material in a real solar concentrator system.

First of all the test was run on 4mm diameter rod. Since phosphate glass is quite hygroscopic, the sample was kept dry during the experiment preparation and cooling water was only applied when the glass was pumped within the laser cavity. Unfortunately, no laser emission was observed and the rod was quickly damaged under about 400 W solar power incident onto input face of the laser head, as it can be seen in figure 6.10.

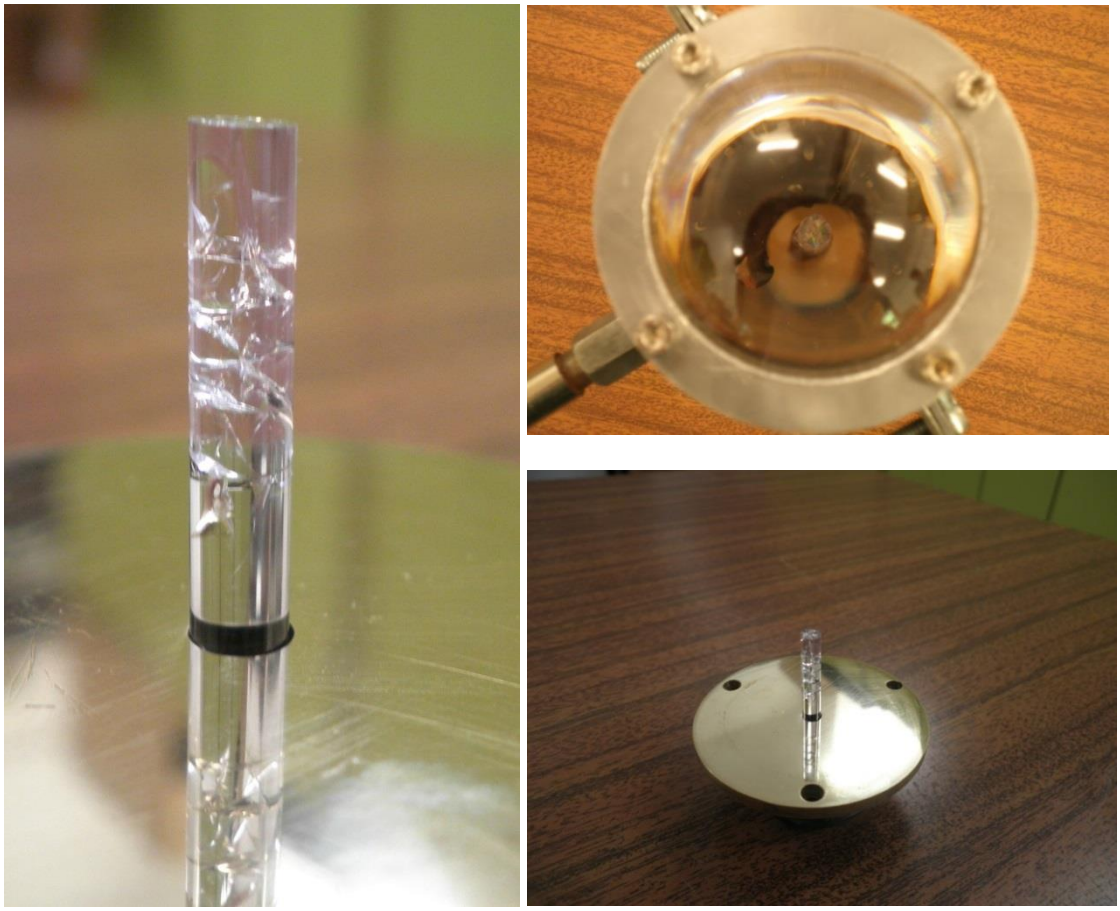

Figure 6.10. Fractured phosphate glass rod of 4 mm diameter after test with 400 Watt of incident solar power.

A second test was performed on a 3 mm diameter glass rod. In this second case the rod did not break within the cavity even with 400W solar laser power at the focal area. Nonetheless no laser emission was measured.

From the picture in figure 6.10 we could observe that the glass broke, but did not crystallize or melt. This means that probably the damage that occurred to the 4 mm rod it was due to thermal shock considering that glass has much lower thermal conductivity than YAG crystal, that was used in the same solar facility. Phosphate glass has a thermal conductivity of about 0.5 W/mK [25] while YAG crystal of about 13 W/mK [26].

The fact that 3mm rod did not break confirmed this hypothesis: smaller diameter sample could better dissipate heat into the cooling water and thus avoid thermal shock.

Concerning the problem that no laser emission was detected we thought it could be due to a bad HR coating on the sample end or a not perfectly planar end surfaces of the sample itself. Another reason could be a problem in the glass synthesis considering that the rods were prepared when the fabrication method was still under optimization.

We plan to repeat the experiment with a better quality glass, using different level of Nd^{3+} doping in the samples.

6.6 Eu^{3+} co-doping of the active material

In order to increase the SPL efficiency, Eu^{3+} co-doping of Nd^{3+}-doped phosphate glasses was evaluated, because it potentially enables an increase in the overall pump power conversion efficiency because of the transfer of the unused solar energy in the UV region by radiative sensitization to wavelengths absorbable by the laser material. Previous works [27, 29] on Eu^{3+} / Nd^{3+} co-doping led to different conclusion concerning the increase of the Nd^{3+} fluorescence due to the energy transfer between Eu^{3+} and Nd^{3+}.

For this study several Eu^{3+}/ Nd^{3+} co-doped phosphate glass samples were manufactured. Their physical, thermal and optical properties were measured along with their spectroscopic behaviour. The energy transfer phenomenon and mechanism between Eu^{3+} and Nd^{3+} ions in co-doped phosphate glass was also investigated.

6.6.1 Glass synthesis and properties measurement

Glass samples (30g batch) used in this research were prepared by conventional melt-quenching technique using chemicals of 99+% purity. Five different glasses, named for short Eu7, EuNd8 ÷ EuNd11, were manufactured in order to evaluate the effect of Eu^{3+} co-doping. They were obtained by doping the host glass ($65P_2O_5$:$17Li_2O$:$3Al_2O_3$:$4B_2O_3$:$5BaO$:$6La_2O_3$ mol%) with different amounts of Eu_2O_3 (2 and 4 mol%) and Nd_2O_3 (ranging from 0 to 2 mol%), both added in substitution of La_2O_3. The full list of glass samples manufactured for this research and their doping concentration are reported in Table 6.2.

Table 6.2. Molar and ionic concentration of dopants in the manufactured phosphate glass samples. The dopant ion concentrations were calculated from measured sample densities (measured by Archimedes method) and their initial compositions.

Glass label	Dopant concentration			
	[mol%]		[x 10^{20} ions/cm^3]	
	Nd^{3+}	Eu^{3+}	Nd^{3+}	Eu^{3+}
Eu7		4		5.3
EuNd8	2	4	2.65	5.29
EuNd9	4	4	5.29	5.29
EuNd10	6	4	7.93	5.29
EuNd11	2	8	2.64	10.5

After weighting and mixing, the batched chemicals were melted in an alumina crucible in a vertical furnace at a temperature of 1350ºC for 1 hours; a mix of O_2/N_2 gases was purged into the furnace during melting in order to minimize the hydroxyl ions (OH^-) content. The melt was then cast into a brass mould preheated at 480 °C and annealed at the same temperature for 10 h to relieve glass internal stresses.

Compared to fabrication method of chapter 4.1, the melting temperature and time were reduced in order to reduce the incorporation of alumina in the glass and to avoid crucible fracture during glass preparation.

Characteristic temperatures of glasses, T_g (glass transition temperature) and T_x (onset crystallization temperature) were measured with a Netzsch DTA 404 PC Eos differential thermal analyser up to 1400 ºC under Ar flow with a heat rate of 10º C/min in sealed Pt pans using typically 30 mg samples.

Measured glass transition temperatures were about 495 °C, around 15 °C lower than values previously measured in similar glasses (see section 4.3.1), thus confirming the lower amount of alumina from the crucible incorporated in these glass samples. The onset crystallization temperatures were found in the order of 700 °C, in line with results previously obtained in similar glasses. This means that a slight change of alumina contents in the glass does not influence the crystallisation temperature of the samples.

The refractive index of the glasses was measured at 5 different wavelengths using the instrument Metricon, model 2010 (see table 6.3). Five scans were performed for each wavelength, the average value of these five measurements representing the refractive index. Estimated error on the measurement was 0.001. The refractive index of each glass was found, as expected, to decrease monotonously with increasing wavelength. On the contrary, the refractive index did not change significantly with changing the doping level of the glasses, due to the fact that the doping oxides, Nd_2O_3 and Eu_2O_3, were both added in substitution of La_2O_3 in the host matrix. Exceptions were samples EuNd8 and EuNd11 that showed values slightly different compared to the other samples, thus probably indicating a small difference in molar composition or fabrication method. Nonetheless it was decided that this difference was negligible for our study focused on the evaluation of Eu^{3+} co-doping of Nd^{3+}-doped phosphate glasses.

Table 6.3. Refractive index of the manufactured glasses at 5 different wavelengths. Estimated error on the measurement is 0.001.

Glass sample	Wavelength [nm]				
	633	825	1061	1312	1533
Eu7	1.5516	1.5469	1.5422	1.5389	1.5363
EuNd8	1.553	1.5476	1.5448	1.5419	1.5384
EuNd9	1.5511	1.5466	1.5420	1.5388	1.5362
EuNd10	1.5511	1.5463	1.5422	1.5390	1.5364
EuNd11	1.5528	1.5477	1.5445	1.5413	1.382

6.6.2 Absorption spectroscopy

The absorption spectra of the manufactured glasses were measured at room temperature for wavelength ranging from 350 to 3000 nm using the double beam scanning spectrophotometer Varian Cary 500 (see section 4.2.5 for details).

Figure 6.11 shows the normalized absorption spectra obtained for the co-doped glass sample EuNd9. Most of the inhomogeneously broadened bands are due to the Nd^{3+} ion and they are assigned to the transitions from the ground state $^4I_{9/2}$ to the excited states of Nd^{3+} ion (see for reference Fig. 6.12). The exceptions are the bands circled in red, that

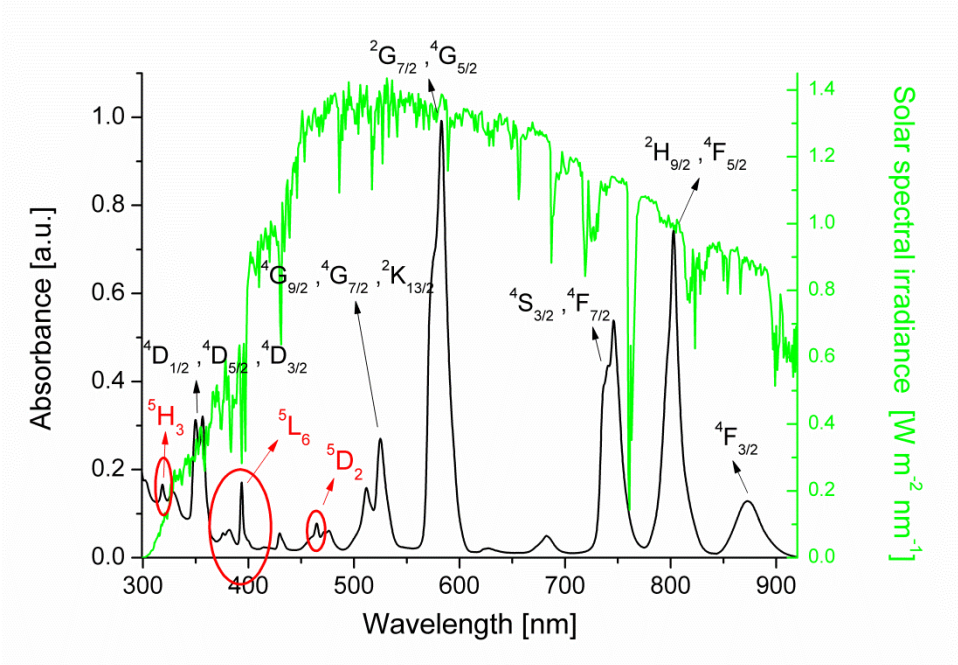

Figure 6.11. Absorption cross-section spectrum for sample EuNd9. The inhomogeneously broadened bands due to the Nd^{3+} ion are assigned (in black) to the transitions from the ground state $^4I_{9/2}$ to the excited states of Nd^{3+} ion. The inhomogeneously broadened bands due to the Eu^{3+} ion are circled in red and are assigned (in red) to the transitions from the ground state $^7F_0$ to the excited states of Eu^{3+} ions. In green, for reference, the direct solar spectral irradiance at sea level is reported (ASTM G173-03).

are due to Eu^{3+} ion; they are assigned to the transitions from the ground state $^7F_0$ to the excited states of Eu^{3+} ions (see for reference Fig. 6.12). Other Eu^{3+} absorption bands usually observed in glasses [29] are not visible because of the strong absorption bands of Nd^{3+} ions at the same wavelengths.

In figure 6.11, for reference, the direct solar spectral irradiance at sea level is also reported (ASTM G173-03). As mentioned above, Nd^{3+} presents several strong absorption bands in the visible, where the sun has its maximum emission, making it a suitable doping ion for the development of a SPL. The Eu^{3+} ion absorption bands are, as expected, mostly located in the UV spectral range, but they are small if compared to the ones measured for Nd^{3+}, so their contributions to the total absorption of the glass is not so relevant.

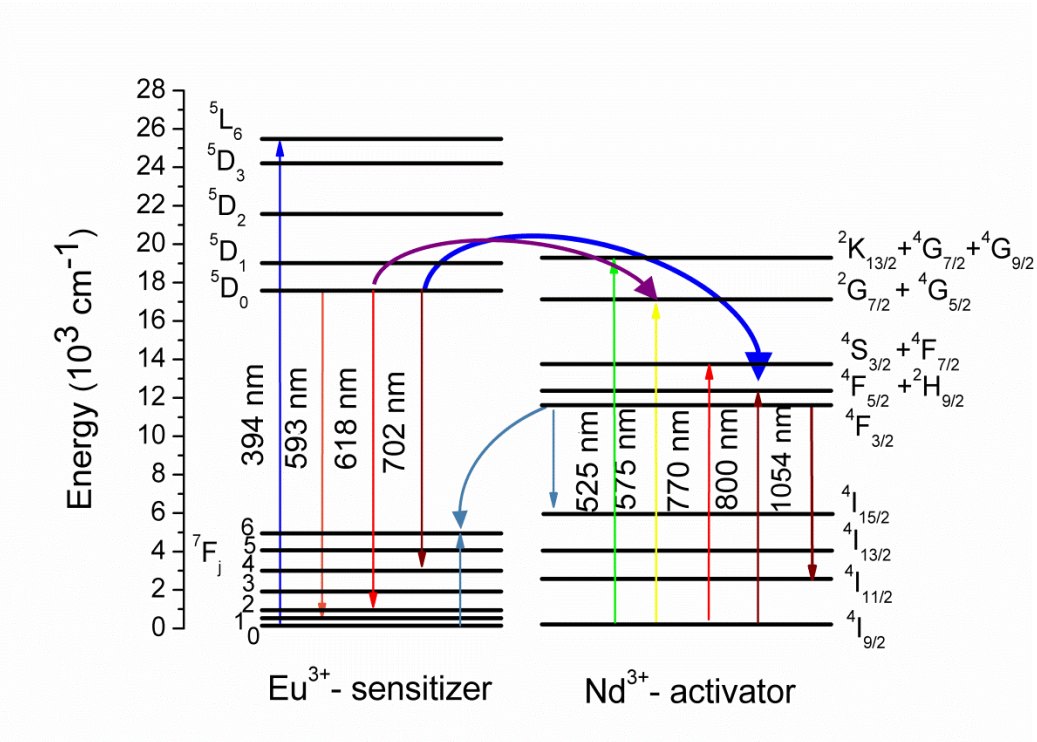

Figure 6.12. Schematic energy level diagram of Eu^{3+} and Nd^{3+} ions.

6.6.3 Emission spectroscopy

Emission spectra of samples Eu7 and EuNd8 ÷ EuNd11 were obtained using a Perkin Elmer LS 55 fluorescence spectrometer equipped with a Xenon lamp as excitation source. The signal was detected with a red-sensitive R928 photomultiplier. For measurements, excitation and emission wavelength were set at 390 nm and between 550 and 750 nm respectively and excitation and emission slit widths were 10 nm. All measurements were performed at room temperature.

Eu^{3+} ion fluorescence was measured upon excitation at 390 nm both in a single doped sample (Eu7) and in presence of Nd^{3+} (EuNd8 ÷ EuNd11). Figure 6.13 reports the emission spectra of samples doped with a 2 mol% fixed amount of Eu^{3+} and an increasing concentration of Nd^{3+}, ranging from 0 (black curve) to 6 mol% (green curve). Eu^{3+} fluorescence decreased with increasing of Nd^{3+} content due to the energy transfer between those ions. The decrease is higher for the peak at 593 nm compared to the one at 618 nm, due to the overlapping with the strong Nd^{3+} absorption band centred

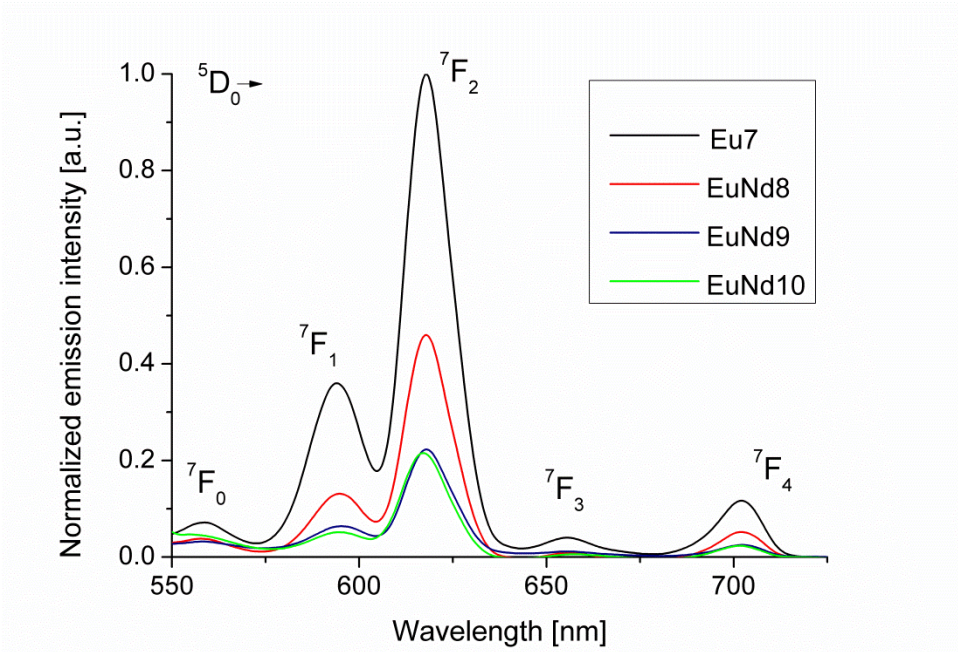

Figure 1.13. Fluorescence spectra of samples doped with a fixed amount of Eu^{3+} (2 mol% concentration) and an increasing concentration of Nd^{3+}, ranging from 0 (black curve) to 6 mol% (green curve).

at this wavelength. Possible energy transfer between ions could occur between the level Eu^{3+}: $^5D_0$ and Nd3+: $^2G_{7/2}$, $^4G_{5/2}$ or between Eu^{3+}: $^5D_0$ and Nd^{3+}: $^4F_{5/2}$, $^2H_{9/2}$ (see Fig. 6.12).

6.6.4 Fluorescence lifetime

As already discussed in paragraph 4.2.7, the fluorescence lifetime determines the decay rate for radiation from a particular transition. It is an essential parameter for the characterization of the emission properties of RE ions in a host medium, and therefore its suitability for active optical devices. Moreover, the fluorescence lifetime is one of the requested parameter for laser design.

The fluorescence lifetime of Nd^{3+}: $^4F_{3/2}$ level was obtained by exciting the samples with light pulses of 785 nm fibre pigtailed laser diode (Axcel B1-785-1400-15A), recording the signal by a digital oscilloscope (Tektronix TDS350) and fitting the decay traces by single exponential (see for details paragraph 4.2.7).

For a Nd^{3+}-doped laser operated at 1.06 μm, the important parameter is the $^4F_{3/2}$ lifetime. A longer lifetime of level $^4F_{3/2}$ benefits the population inversion between this level (the upper laser level) and the $^4I_{11/2}$ one (the lower laser level).

The decay curves of the Nd^{3+}: $^4F_{3/2}$ was measured under 785 nm excitation for all co-doped samples and the results are listed in Table 6.4. In the table, for reference, the lifetime of single doped samples, Nd1 ÷ Nd6, are also reported.

Table 6.4. Fluorescence decay time of the $^4F_{3/2}$ state of Nd^{3+} ion in single doped and co-doped samples under laser excitation at 785 nm.

Glass label	Dopant concentration [mol%]		Nd^{3+}:$^4F_{3/2}$ lifetime [μs] ±15μs
	Nd^{3+}	Eu^{3+}	
Nd1	0.1		365
Nd2	1		358
Nd3	2		327
Nd4	4		212
Nd5	6		177
Nd6	10		92
EuNd8	2	4	103
EuNd11	2	8	50

Considering samples Nd3, EuNd8 and EuNd11, they have a fixed Nd^{3+} concentration of 2 mol% and an increasing Eu^{3+} concentration, ranging from 0 to 8 mol%. In these samples, the lifetime of level Nd^{3+}: $^4F_{3/2}$ has a sharp decrease with increasing Eu^{3+} concentration, reducing from 327 μs in absence of Eu^{3+} to 50 μs in the co-doped sample EuNd11 (8 mol% of Eu^{3+}). This result indicates that there is an Eu^{3+} concentration dependent quenching of Nd^{3+} fluorescence due to unwanted interactions between the two ions species, as already observed in [28].

Lower lifetime means higher decay rate from the Nd^{3+}:$^4F_{3/2}$ emitting level due to non-radiative decay process towards the Eu^{3+} energy level. We can estimate the efficiency of this energy transfer using the following formula [31]:

$$P = 1 - \left(\frac{\tau}{\tau_0}\right) \tag{6.1}$$

where τ_0 and τ are the lifetime Nd^{3+}:$^4F_{3/2}$ in absence and presence of Eu^{3+} co-doping. The calculated efficiency of the transfer for the co-doped sample with higher amount of Eu^{3+} ions (EuNd11) is 85%.

These non-radiative decay processes will reduce the radiative quantum efficiency of the Nd^{3+}:$^4F_{3/2}$ emitting level and hence will limit the usefulness of Eu^{3+} sensitization for Nd^{3+} laser action.

6.7 Conclusion and future development

In this chapter the possibility to develop a Nd^{3+}-doped solar pumped fiber laser based on the developed phosphate glass host presented in chapter 4 is discussed and preliminary results of active material evaluation are presented.

All prepared glass samples were homogeneous and presented a good thermal stability and thus are suitable for fibre drawing. The glasses present several strong absorption bands in the visible where the sun has its maximum emission, making them suitable for the development of a SPL. A strong emission at 1.06 µm was measured for each sample by using two different excitation sources: a laser at 795 nm and a polychromatic light, confirming the possibility to pump these glasses by concentrated sunlight.

In order to increase the efficiency of the active material for SPL, Eu^{3+} co-doping of Nd^{3+}-doped phosphate glass was evaluated. The co-doping gave a limited increase to the glass pump power absorption limited to the UV range. Although energy transfer from Eu^{3+} to Nd^{3+} occurred, a large Eu^{3+} concentration dependent quenching of Nd^{3+} fluorescence was observed. This latter process decreases the radiative quantum efficiency of Nd^{3+}:$^4F_{3/2}$ emitting level and hence limits the attractiveness of Eu^{3+} sensitization for Nd^{3+} laser action.

The next step in this research will be the design, based on these preliminary results, of the optical fibre to be pumped with concentrated solar light. The choice of the most suitable Nd^{3+} doping level will be driven not only by the concentration quenching effect, but also by the maximum energy available for the pumping. Thus, it will depend on the dimension and efficiency of the solar element collection system and the optical pumping scheme.

REFERENCES

[1] E. Snitzer, "Optical Maser Action of Nd^{3+} in a Barium Crown Glass," Phys. Rev. Lett., pp. 444-446, 1961.

[2] J. A. Duffie and W. A. Beckman, "Solar Engineering of Thermal Process", Chapter 7, edited by John Wiley & Sons, Inc. 1991.

[3] http://www.astm.org/Standards/G173.htm.

[4] T. Yabe et al., "100 W-class solar pumped laser for sustainable magnesium-hydrogen," J. Appl. Phys. 104, pp. 083104-083104.8, 2008.

[5] D. Graham-Rowe, "Solar-powered lasers," Nat. Photonics 4(2), pp. 64–65, 2010.

[6] M. Lando, J. Kagan, B. Linyekin, and V. Dobrusin, "A solar-pumped Nd:YAG laser in the high collection efficiency regime," Opt. Commun. 222, pp. 371-381, 2003.

[7] L. Summerer et al., "Concepts for wireless energy transmission via laser," ESA, ACT-RPR-NRG-2009-SPS-ICSOS, 2009.

[8] A. Biswas et al., "Deep-Space Optical Communications Downlink Budget from Mars: System Parameters," IPN-NASA Progress Report, 42-154, 2003.

[9] D. P. Resendes et al., "Laser Propulsion for ESA Missions: Ground to Orbit Launch Project Overview — Part 1," BEAMED ENERGY PROPULSION: Fourth International Symposium on Beamed Energy Propulsion. AIP Conference Proceedings, Volume 830, pp. 576-587, 2006.

[10] C. A. Maddock et al., "Designs of multi-spacecraft swarms for the deflection of Apophis by solar sublimation," ESA, ACT-RPR-MAD-2009, 2009.

[11] www.esa.int

[12] T. Yabe et al. "Demonstrated Fossil-Fuel-Free Energy Cycle Using Magnesium and Laser," Appl. Phys. Lett. 89, 261107-261107.3, 2006.

[13] Z. I. Kiss, H.R. Lewis and R.C. Duncan "Sun pumped continuous optical maser," Appl. Phys. Lett. 2, pp. 93-94, 1963.

[14] C. G. Young, "A sun-pumped cw one-watt laser," Appl. Opt. 5, pp. 993-997, 1966.

[15] V. Krupkin, Y. Kagan, and A. Yogev, "Nonimaging optics and solar pumping at the Weizmann Institute," Proc. SPIE 2016, pp. 50-60, 1993.

[16] T. Yabe et al., "Noncatalytic dissociation of MgO by laser pulses towards sustainable energy cycle," J. Appl. Phys. 101, 123106–123106.7, 2007.

[17] D. Liang andG. Almeida, "Highly efficient solar-pumped Nd:YAG laser," Opt. Express 19, pp. 26399-26405, 2011.

[18] K. Ueda, A. Liu, K. Kametani, and M. Kamamura, "Possibility of solar-pumped fiber lasers," IEEJ OQD-97-19, pp. 13–19, 1997.

[19] S. Mizuno, H. Ito, K. Hasegawa, T. Suzuki, and Y. Ohishi, "Laser emission from a solar-pumped fiber," Opt. Express 20, pp. 5891-5895, 2012.

[20] J. Nilsson and D. Payne, "High-power fiber lasers," Science 332 (6032), pp. 921-922, 2011.

[21] Y. Shimony Z. Burshtein, A. B.-A. Baranga, Y. Kalisky, and M. Strauss, "Repetitive Q-switching of a cw Nd:YAG laser using Cr^{4+}:YAG saturable absorbers," IEEE J. Quantum Electron. 32, pp. 305–310, 1996.

[22] M. Lando, Y. Shimony, Y. Noter, R. M. J. Benmair, and A. Yogev, "Passive Q switching of a solar-pumped Nd:YAG laser," Appl. Optics 39, pp. 1962-1965, 2000.

[23] Y. W. Lee et al., "High-Power Yb^{3+}-Doped Phosphate Fiber Amplifier," J. Sel. Top. Quant. 15, pp. 93-102, 2009.

[24] M. Weksler and J. Shwartz, "Solar-pumped solid-state lasers," IEEE J. Quantum Electron. 24, pp. 1222-1228, 1988.

[25] M. Yamane and Y. Asahara, "Glasses for Photonics," Cambridge University Press, 2004.

[26] http://www.rp-photonics.com/yag_lasers.html

[27] A. Y. Cabezas and L. G. DeShazer, "Radiative transfer of energy between rare earth ions in glass," Appl. Phys. Lett. 4, pp. 37-39, 1964.

[28] E. J. Sharp, M. J. Weber, and G. Cleek, "Energy Transfer and Fluorescence Quenching in Eu and Nd Doped Silicate Glasses," J. Appl. Phys. 41, pp. 364-369, 1970.

[29] J. C. Joshi, N. C. Pandey, B. C. Joshi, R. Belwal, and Janardan Joshi, "Quantum efficiency of diffusion-limited energy transfer from Eu^{3+}-> Nd^{3+} in borate glass," J. Solid State Chem. 23, pp. 135-139, 1978.

[30] G. Pucker, K. Gatterer, H.P. Fritzer, M. Bettinelli, and M. Ferrari, "Optical investigation of Eu^{3+} in a sodium borosilicate glass: Evidence for two different site distributions," Physical Review B 53, pp. 6225-6234, 1996.

[31] H.-Y.D. Kel, and E.R. Birnbaum, "Many-Body Nonradiative Energy Transfer in a Crystalline Europium(III) EDTA Complex," J. Lumin. 63, pp 9-17, 1995.

Conclusions

Nd^{3+}-doped fibre lasers have a lot of potential applications in many different fields, in which they could replace other lasers systems, such as solid state lasers based on crystals, bringing all the advantages of reliability, compactness and efficiency of fibre laser solutions. Many applications, especially those that require high output power, would benefit from a fibre laser developed in a phosphate glass host that possess several interesting features, such as a higher RE solubility (compared to silica glass), higher photo-darkening threshold and lower nonlinear refractive index.

In this thesis I have presented a research toward the development of a novel phosphate glass suitable for the realization of Nd^{3+}-doped optical fibre lasers.

The first part of the work was focused on the design, engineering and manufacturing of a host glass able to incorporate high amount of RE ions and suitable for fibre drawing. Several doped phosphate glass samples were fabricated by doping the developed host glass with concentrations of Nd^{3+} up to 10 mol%. All prepared glass samples were homogeneous, transparent and presented good thermal stability and thus were found suitable for fibre drawing.

In order to perform spectroscopic characterization of the manufactured samples, a dedicated set-up for active glass spectroscopy (frequency and time resolved) measurements in clean room environment was developed, as part of the work of this PhD activity.

A strong emission at 1.06 μm was measured for each glass sample by using a laser emitting at the wavelength of 785 nm as excitation source. The effect of Nd^{3+} doping concentration on optical properties was investigated in order to study the concentration quenching effect on luminescence performance. No changes in the shape of the fluorescence spectrum were found with increasing the Nd^{3+} ion doping level. Lifetimes of the Nd^{3+}:$^4F_{3/2}$ were found to decrease with increasing Nd^{3+} concentration. The following characteristic values parameters were obtained: radiative lifetime τ_0 = 367 μs and quenching concentration N_0 = 8.47 E+20 ions/cm^3.

A second step in the research was to realize, using the previously developed phosphate glass, a DC optical fibre. This goal required the fabrication of three different phosphate glasses with similar thermo-mechanical properties, but with a suitable refractive indexes contrast in order to obtain an adequate numerical aperture between core and inner cladding, and between inner and outer cladding.

The three manufactured glasses showed great stability toward crystallization due to the presence of network intermediate (R_2O_3) and limited glass transition temperature.

The Nd^{3+}-doped core glass exhibited a strong emission at 1.06 μm when excited by a laser diode emitting at 785 nm. The lifetimes of the Nd^{3+}:$^4F_{3/2}$ was measured; the value obtained (305 ± 15 μs) was in line with previous measurements performed on the same glass system.

Numerical analysis of the Nd^{3+}-doped fibre lasers was performed in order to optimize laser design. With the concentration level used for manufacturing the core glass ($2.4 \cdot 10^{20}$ Nd^{3+} ions/cm^3) and the numerical aperture obtained from our glasses, an output power around 0.6 W could be obtained using 10 cm of active fibre (10/50/125 μm), thus obtaining a 30% optical conversion efficiency with respect to the launched pump power (via cladding pump).

A Nd^{3+}-doped DC optical fibre based on the developed glass host composition was successfully drawn and characterized with the dimension of 8/35/105 μm. The fabricated fibre was free from air bubbles but presented some defects at the interface between inner and outer cladding. It was assessed that the defects were not crystals, but the reason of their formation is still under investigation.

Guiding properties inside the core was verified by near field measurement, thus confirming that the defects are located mainly at less critical interface between inner and outer cladding. The measured attenuation coefficient was 5.7 dB/m.

A CW cladding pumped fibre laser based on 9 cm of fabricated Nd^{3+}-doped optical fibre emitting at 1054.5 μm was demonstrated, with a slope efficiency of 18% with respect to the launched pump power. A maximum output power of 85 mW was obtained for a launched pump power of 930 mW.

The obtained optical conversion efficiency (~9%) is relatively low compared to the one (30%) foreseen from the laser design. This result could be explained by several factors. First of all the fibre dimensions used for laser design where slightly bigger than the real ones: 10/50/125 μm against 8/35/105 μm. Moreover the fabricated fibre showed some defects at the interface between the two claddings, which certainly affected the confinement of the pump light into the inner cladding. At last mechanical tolerances in the positioning of the flexure stages could have caused imperfect alignment between the optical elements forming the laser cavity.

It must be said that at this stage of the research, the aim was not the realization and optimization of a fibre laser, but a preliminary evaluation of the laser emission from the manufactured fibre. Further work on spliceability of phosphate fibres to commercial silica based fibre and fibre components, will allow the realization of the whole laser resonator in fibre (all fibre setup) avoiding the use of free-space optics, with their stringent requirements for precise alignment.

In order to optimize laser output emission from the Nd^{3+} doped fibre, additional work will be also carried out in order to address the problem of defects formation at the interface between the two cladding during fibre drawing.

Part of the PhD research activity was also dedicated to the possibility to develop a Nd^{3+}-doped solar pumped fibre laser based on the in-house developed phosphate glass active material.

Nd^{3+}-doped glasses present several strong absorption bands in the visible where the sun has its maximum emission, making them suitable for the development of a SPL. A strong emission at 1.06 μm was measured for each sample by using two different excitation sources: a laser at 795 nm and a polychromatic light, confirming the possibility to pump these glasses by concentrated sunlight.

In order to increase the efficiency of the active material for SPL, Eu^{3+} co-doping of Nd^{3+}-doped phosphate glass was also evaluated. The co-doping gave a limited increase to the glass pump power absorption limited to the UV range. Although energy transfer from Eu^{3+} to Nd^{3+} occurred, a large Eu^{3+} concentration dependent quenching of Nd^{3+} fluorescence was observed. This latter process decreases the radiative quantum efficiency of Nd^{3+}:$^4F_{3/2}$ emitting level and hence limits the attractiveness of Eu^{3+} sensitization for Nd^{3+} laser action.

The next step in this research will be the design, based on these preliminary results, of the optical fibre to be pumped with concentrated solar light, using a Fresnel lens as collecting element. The choice of the most suitable Nd^{3+} doping level will be driven not only by the concentration quenching effect, but also by the maximum energy available for the pumping. Thus, it will depend on the dimension and efficiency of the solar element collection system and the optical pumping scheme.

Appendix A

Phosphate fibre splicing

Fibre fusion splicing is a technique where two laterally aligned bare fibre ends are joined together permanently by heating them above melting temperature while pushing together in axial direction. The heating is often accomplished with a high-voltage electric discharge, but there are other methods such as a tungsten or graphite filament, a CO_2 laser, or a gas flame. An inert gas is often used in combination with the filament technique to prevent the filament from oxidation.

Standard procedure of splicing consists in:

- fibres coating removal;
- cleaning of the fibres glass with alcohol;
- cleaving of the two fibre ends;
- aligning and fusion splicing using custom parameters for the fusion splicer, optimized for the given fibre type (material and geometry);
- reinforcing the optical fibre splice with a protection sleeve.

Splicing of standard silica based fibres can exhibit very low optical losses if the two fibres have the same geometry and, in ideal conditions, losses are of the order of 0.02 dB. Nearly no light will be reflected at the splice. The splice location can then hardly be seen under a microscope. Nevertheless, the mechanical strength of the splice and its surroundings may be well below that of the normal bare fibre, if the fibre surface receives some damage during handling. After splicing, it is common to apply a new

coating or add a protection sleeve in order to obtain a sufficiently high mechanical robustness.

When dealing with high-power fibre lasers and amplifiers the power of light lost in splices can be sufficient for burning materials, in particular fibre coatings. This means that high-quality splices are essential not only for the power efficiency, but also for reliable operation.

If the fibres to splice are not based on the same glass system, for example phosphate and silica, the operation poses a particular challenge, due to the fundamentally different thermal and mechanical properties of different glass families. Nevertheless this is a key point for the integration of phosphate glass fibres in commercial system based on silica glass fibre and components.

Table A.1 lists thermo-mechanical parameters of phosphate and silica glass that are most critical for this process. The quite different glass transition temperatures T_g would require non-symmetrical heating of the splice zone and the largely different coefficient of thermal expansion may cause stress in the splice region.

Table A.1. Thermo-mechanical parameters of phosphate and silica glass critical for fibres splicing.

Parameter	Phosphate	Silica
Glass transition temperature T_g [°C]	490	1000
Coefficient of thermal expansion [$°C^{-1}$]	10 E-6	0.5 E-6

A passive phosphate fibre manufactured in our laboratory (40-125 µm) was used for preliminary test of cleaving and fusion splice with commercial silica MM fibre (50-125 µm), using standard splicer equipment, Fujikura FSM-30S. The system does not allow a non-symmetrical heating of the splice zone, but allows the user to adjust several independent variables.

After several trials, a custom splicing recipe was developed, starting with a conventional recipe for silica-to-silica splicing and successively changing the parameters, until a splice with sufficient mechanical robustness was obtained. The obtained parameters are shown in Table A.2.

Table A.2. Splice parameters used for phosphate-to-silica fibre splicing.

Parameter	Unit	Value
Mode		MM
Arc power	[bit]	2
Arc time	[ms]	100
Prefuse time	[ms]	0
Fibre forwarding time	[ms]	85
Gap value	[line]	6

In figure A.1 an image of one of the splice realized is reported.

Future work will include the evaluation of optical attenuation and mechanical strength of the obtained splice.

Figure A.1. Pictures of a fusion splice between a phosphate fibre (right) and a silica fibre (left).

Appendix B

List of publications during PhD

Journal Papers

Bourhis K., Petit L., Koponen J., **Boetti N. G.**, Milanese D., "Influence of the P_2O_5/Al_2O_3 co-doping on the local environment of erbium ions and on the 1.5 um quantum efficiency of Er^{3+}-borosilicate glasses," Optical Materials 36, pp. 926-931, 2014.
DOI 10.1016/j.optmat.2013.12.035

Scarpignato G.C., Milanese D., Lousteau J., **Boetti N. G.**, Mura E., "Fabrication and Characterization of a High-Gain Yb-Er Codoped Phosphate Glass Optical Amplifier;" Journal Of Engineering, vol. 2013, pp. 1-4, 2013.
DOI: 10.1155/2013/858341

Boetti N. G., Negro D., Lousteau J., Freyria F. S., Bonelli B., Abrate S., Milanese D., "Spectroscopic investigation of Nd^{3+} single doped and Eu^{3+} / Nd^{3+} co-doped phosphate glass for solar pumped lasers," Journal of Non-Crystalline Solids, vol. 377, pp. 100-104, 2013.
DOI: 10.1016/j.jnoncrysol.2013.01.004

Lousteau J., Scarpignato G., Athanasiou G. S., Mura E., **Boetti N.**, Olivero M., Benson T., Sewell P., Abrate S., and Milanese D., "Photonic bandgap confinement in an all-

solid tellurite-glass photonic crystal fiber," Optics Letters, Vol. 37, Issue 23, pp. 4922-4924, 2012.
DOI: 10.1364/OL.37.004922

Shiyu Y., Lousteau J., Olivero M., Merlo M., **Boetti N. G.**, Abrate S., Chen Qiuling, Chen Qiuping, Milanese D., "Analysis of Faraday effect in multimode tellurite glass optical fiber for magneto-optical sensing and monitoring applications," Applied Optics, vol. 51 n. 19, pp. 4542-4546, 2012.
DOI: 10.1364/AO.51.004542

Lousteau J., **Boetti N. G.**, Chiasera A., Ferrari M., Abrate S., Scarciglia G., Venturello A., Milanese D., "Er^{3+} and Ce^{3+} co-doped tellurite optical fiber for lasers and amplifiers in the near infrared wavelength region: fabrication, optical characterization and prospects," IEEE Photonics Journal, vol. 4 n. 1, pp. 194-204, 2012.
DOI: 10.1109/JPHOT.2011.2181974

Olivero M., Braglia A., Perrone G., **Boetti N. G.**, Lousteau J., Milanese D., "Improved setup and procedure for benchmarking of photodarkening in Ytterbium doped silica fibers," Journal Of Optics, vol. 14 n. 12, pp. 125702-125707, 2012.
DOI:10.1088/2040-8978/14/12/125702

Boetti N. G., Lousteau J., Negro D., Mura E., Scarpignato G., Abrate S., Milanese D., "Multiple visible emissions by means of up-conversion process in a microstructured tellurite glass optical fiber," Optics Express, vol. 20 n. 5, pp. 5409-5418, 2012.
DOI: 10.1364/OE.20.005409

Boetti, N. G., Lousteau, J., Chiasera, A., Ferrari, M., Mura, E., Scarpignato, G.C., Abrate, S., Milanese, D., "Thermal stability and spectroscopic properties of erbium-doped niobic-tungsten tellurite glasses for laser and amplifier devices," Journal of Luminescence, Vol. 132, Issue 5, pp. 1265-1269, 2012.
DOI: 10.1016/j.jlumin.2011.12.057

Gomes, L., Milanese, D., Lousteau, J., **Boetti, N.**, Jackson, S.D., "Energy level decay processes in Ho^{3+}-doped tellurite glass relevant to the 3 μm transition," Journal of Applied Physics, Vol. 109, Issue 10, pp. 103110-103110-6, 2011.

DOI: 10.1063/1.3587476

Proceedings

Mura E., Scarpignato G.C., Lousteau J., Rondinelli M., **Boetti N.G**., Milanese D., "Rare-Earth Doped Phosphate Glass Fibers," Advanced Solid state Laser Congress, Paris, 27 October - 1 November 2013.

Lousteau J., Mura E., Rondinelli M., **Boetti N. G.**, Heidt A., Richardson D.J., Honkanen S., Milanese D., "New Developments in Tellurite Glass Fibers," Workshop on Specialty Optical Fibers, Sigtuna, Sweden, 28-30 August 2013.

Boetti N.G., Lousteau J., Mura E., Scarpignato G.C., Milanese D., "Nd^{3+} Doped Phosphate Glass Optical Fibre Lasers," 15th International Conference on Transparent Optical Networks, Cartagena (Spain), 23-27 June 2013.
DOI: 10.1109/ICTON.2013.6602841

Mura E., Annoscia A., Lousteau J., **Boetti N.G.**, Milanese D., "Dehydration study on phosphate glasses for optical fibers," in: The 23rd International Congress on Glass, Prague, Czech Republic, 1-5 July 2013.

Scarpignato G. C., Lousteau J., Mura E., **Boetti N. G.**, Abrate S., Milanese D., Bastard L., Broquin J. E., "Design curves based optimization and fabrication of a high gain Yb-Er co-doped optical amplifier based on phosphate glasses," in: CLEO®/Europe-IQEC 2013, Munich, 12-16 May 2013.

Mura E., Scarpignato G. C., Lousteau J., **Boetti N. G.**, Abrate S., Milanese D., "Yb-doped phosphate double-cladding optical fiber laser for high-power applications," Photonics West, San Francisco (USA), 2-7 February 2013.

Boetti N. G., Lousteau J., Negro D., Mura E., Scarpignato G. C., Perrone G., Abrate S., Milanese D., "Solar pumping of solid state lasers for space mission: a novel approach," International Conference on Space Optics, Ajaccio (France), October 9th-12th 2012.

Lousteau J., **Boetti N. G.**, Mura E., Negro D., Scarpignato G. C., Perrone G., Abrate S., Milanese D., "Photonic glasses for IR and mid-IR spectral range,". International Conference on Space Optics (ICSO), Ajaccio (France), 9th-12th October 2012.

Milanese D., Lousteau J., **Boetti N. G.**, Mura E., Scarpignato G. C., Negro D., Ferraris M., Perrone G., Olivero M., Abrate S., "Fibra ottica micro-strutturata a base di vetri telluriti drogati con ioni di terre rare per applicazioni fotoniche," XI Convegno Nazionale AIMAT, Gaeta (LT), 16–19 settembre 2012.

Mura E., Lousteau J., **Boetti N. G.**, Scarpignato G. C., Negro D., Milanese D., "Double-cladding optical fibre from phosphate glasses for high-power laser applications," 18th International Symposium on Non-Oxide and New Optical Glasses ISNOG, St. Malo (France), 1st July - 5th July 2012.

Shiyu Y., Lousteau J., Olivero M., Merlo M., **Boetti N. G**., Abrate S., Milanese D., Chen Q., Pirri F., Ferraris M., "Investigation of the Faraday effect in tellurite glass optical fiber," 14th International Conference on Transparent Optical Networks, Warwick (UK), 1-5 July 2012.
DOI: 10.1109/ICTON.2012.6253717

Boetti N. G., Lousteau J., Negro D., Mura E., Scarpignato G. C., Abrate S., Milanese D., "Spectroscopic investigation of Eu^{3+} / Nd^{3+} codoped phosphate glass for solar-pumped lasers," 18th International Symposium on Non-Oxide and New Optical Glasses ISNOG, St. Malo, 1st July - 5th July 2012.

Mura E., Lousteau J., **Boetti N.**, Scarpignato G. , Negro D., Abrate S., Milanese D., "Phosphate double-cladding optical fibre for high-power laser applications," Specialty Optical Fibers & Applications (SOF), Colorado Springs (USA), 17 June - 20 June 2012.

Lousteau J., Scarpignato G.C., Athanasiou G., Mura E., **Boetti N. G.**, Olivero M., Benson T., Milanese D., "Photonic bandgap confinement in an all-solid tellurite glass photonic crystal fiber," Specialty Optical Fibers & Applications (SOF), Colorado Springs, 17 June -20 June 2012.

Bourhis K., Ferraris M., Milanese D., Chen Q., Perero S., Lousteau J., Mura E., Negro D., **Boetti N. G.**, Scarpignato G. C., "Development of innovative optical glasses for photonics at Politecnico di Torino: novel silica and tellurite glasses," Fotonica 2012, 14° Convegno Nazionale delle Tecnologie Fotoniche, Firenze, 15-17 maggio 2012.

Milanese, D., Lousteau, J., Gomes, L., **Boetti, N.**, Abrate, S., Jackson, S., "Ho-doped tellurite glasses for emission in the mid infrared wavelength region," 2011 Conference on Lasers and Electro-Optics Europe and 12th European Quantum Electronics Conference, CLEO EUROPE/EQEC 2011.
DOI: 10.1109/CLEOE.2011.5942833

Scarpignato G. C., Lousteau J., Athanasiou G., Mura E., **Boetti N. G.**, Olivero M., Benson T., Milanese D., "Photonic bandgap confinement in an all-solid tellurite glass photonic crystal fibre," Micro- and nano-photonic materials and devices, Trento, January 16-18, 2012.

Milanese D., Lousteau J., **Boetti N. G.**, Mura E., Scarpignato G. C., Negro D., Perrone G., Olivero M., Grassini S., Rollino S., Ferraris M, "Tellurite glass optical fibres for lasers and amplifiers in the near infrared wavelength region," VIII INSTM CONFERENCE, Catania, 26-29th June 2011.

Lousteau J., **Boetti N.**, Negro D., Mura E., Scarpignato G., Raimondo M., Abrate S. and Milanese D., "Rare-earth doped tellurite glass optical fibre for visible light sources," Transparent Optical Networks (ICTON), 2011 13th International Conference Stockholm (Sweden) June 2011.
DOI: 10.1109/ICTON.2011.5971059

Olivero M., **Boetti N.**, Braglia A., Neri A., Lousteau J., Milanese D., "Measurements techniques for the evaluation of photodarkening in fibers for high power lasers," Proceedings of SPIE - The International Society for Optical Engineering, Photonic West, (San Francisco) 22-27 January 2011, vol. 7914, article 79142U.
DOI: 10.1117/12.876276